NAVAL POSTGRADUATE SCHOOL

MONTEREY, CALIFORNIA

THESIS

SYSTEMATIC REVIEW OF UIT PARAMETERS ON RESIDUAL STRESSES OF SENSITIZED AA5456 AND FIELD BASED RESIDUAL STRESS MEASUREMENTS FOR PREDICTING AND MITIGATING STRESS CORROSION CRACKING

by

Michelle E. Haggett

March 2014

Thesis Advisors:	Luke N. Brewer Kim Ngoc Tran

Approved for public release; distribution is unlimited

REPORT DOCUMENTATION PAGE	*Form Approved OMB No. 0704-0188*

1. AGENCY USE ONLY *(Leave blank)*	**2. REPORT DATE** March 2014	**3. REPORT TYPE AND DATES COVERED** Master's Thesis

4. TITLE AND SUBTITLE
SYSTEMATIC REVIEW OF UIT PARAMETERS ON RESIDUAL STRESSES OF SENSITIZED AA5456 AND FIELD BASED RESIDUAL STRESS MEASUREMENTS FOR PREDICTING AND MITIGATING STRESS CORROSION CRACKING

5. FUNDING NUMBERS

6. AUTHOR(S) Michelle E. Haggett

7. PERFORMING ORGANIZATION NAME(S) AND ADDRESS(ES)
Naval Postgraduate School
Monterey, CA 93943-5000

8. PERFORMING ORGANIZATION REPORT NUMBER

9. SPONSORING /MONITORING AGENCY NAME(S) AND ADDRESS(ES)
Mr. R. Hays
OSD-Corrosion Policy and Oversight
OSD(AT&L) CPO
3000 Defense Pentagon
Washington DC 20301
Dr. K. Tran
Naval Surface Warfare Center, Carderock Division
9500 MacArthur Blvd.
West Bethesda, MD 20817

10. SPONSORING/MONITORING AGENCY REPORT NUMBER

11. SUPPLEMENTARY NOTES The views expressed in this thesis are those of the author and do not reflect the official policy or position of the Department of Defense or the U.S. Government. IRB protocol number ____N/A____.

12a. DISTRIBUTION / AVAILABILITY STATEMENT Approved for public release; distribution is unlimited	**12b. DISTRIBUTION CODE** A

13. ABSTRACT (maximum 200 words)

This thesis focuses on the use of x-ray diffraction to measure residual stresses around welds in aluminum ship structures both in the laboratory and in the field. Tensile residual stresses are often generated during welding and, in sensitized aluminum structures, can cause extensive stress corrosion cracking. Peening techniques, such as ultrasonic impact treatment (UIT), can mitigate and even reverse these tensile residual stresses. This research uses x-ray diffraction to measure residual stresses around welds in AA5456 before and after UIT. In particular, we examined the importance of UIT parameters such as peening amplitude and pin size. We found that all combinations of UIT parameters removed the tensile residual stresses and resulted in compressive stress several hundred microns below the weld surface. The exact level of compressive residual stress was sensitive to the pin size used with a smaller, but measurable, dependence upon the displacement amplitude. In an effort to extend these measurement techniques to the field, we successfully performed the first x-ray residual stress measurements on a U.S. naval combatant.

14. SUBJECT TERMS SCC, stress corrosion cracking,AA5456, ultrasonic impact treatment, UIT, XRD, residual stress	**15. NUMBER OF PAGES** 133
	16. PRICE CODE

17. SECURITY CLASSIFICATION OF REPORT Unclassified	**18. SECURITY CLASSIFICATION OF THIS PAGE** Unclassified	**19. SECURITY CLASSIFICATION OF ABSTRACT** Unclassified	**20. LIMITATION OF ABSTRACT** UU

NSN 7540-01-280-5500
Standard Form 298 (Rev. 2-89)
Prescribed by ANSI Std. 239-18

THIS PAGE INTENTIONALLY LEFT BLANK

SYSTEMATIC REVIEW OF UIT PARAMETERS ON RESIDUAL STRESSES OF SENSITIZED AA5456 AND FIELD BASED RESIDUAL STRESS MEASUREMENTS FOR PREDICTING AND MITIGATING STRESS CORROSION CRACKING

Michelle E. Haggett
Lieutenant, United States Navy
B.S., Old Dominion University, 2009

Submitted in partial fulfillment of the
requirements for the degree of

MASTER OF SCIENCE IN MECHANICAL ENGINEERING

from the

NAVAL POSTGRADUATE SCHOOL
March 2014

Author: Michelle E. Haggett

Approved by: Luke N. Brewer
Thesis Co-Advisor

Kim Ngoc Tran
Thesis Co-Advisor

Knox T. Millsaps
Chair, Department of Mechanical and Aerospace Engineering

THIS PAGE INTENTIONALLY LEFT BLANK

ABSTRACT

This thesis focuses on the use of x-ray diffraction to measure residual stresses around welds in aluminum ship structures both in the laboratory and in the field. Tensile residual stresses are often generated during welding and, in sensitized aluminum structures, can cause extensive stress corrosion cracking. Peening techniques, such as ultrasonic impact treatment (UIT), can mitigate and even reverse these tensile residual stresses. This research uses x-ray diffraction to measure residual stresses around welds in AA5456 before and after UIT. In particular, we examined the importance of UIT parameters such as peening amplitude and pin size. We found that all combinations of UIT parameters removed the tensile residual stresses and resulted in compressive stress several hundred microns below the weld surface. The exact level of compressive residual stress was sensitive to the pin size used with a smaller, but measurable, dependence upon the displacement amplitude. In an effort to extend these measurement techniques to the field, we successfully performed the first x-ray residual stress measurements on a U.S. naval combatant.

THIS PAGE INTENTIONALLY LEFT BLANK

TABLE OF CONTENTS

THIS PAGE INTENTIONALLY LEFT BLANK

LIST OF FIGURES

LIST OF TABLES

THIS PAGE INTENTIONALLY LEFT BLANK

LIST OF ACRONYMS AND ABBREVIATIONS

AA	aluminum alloy
ARB	accumulative roll bonding
ASTM	American Society for Testing and Materials
AU	Applied Ultrasonics
BSE	backscatter electron
CCD	charge coupled device
DOS	degree of sensitization
EBSD	electron backscatter diffraction
ECAE	equal channel angular extrusion
FIB-SEM	focused ion beam, scanning electron microscope
GMAW	gas metal arc welding
GOS	grain orientation spread
GPa	gigapascal
GTAW	gas tungsten arc welding
IGSCC	intergranular stress corrosion cracking
M	molar
MET	multiple exposure technique
MPa	megapascal
NAMLT	nitric acid mass loss test
NSWCCD	Naval Surface Warfare Center Carderock Division
SET	single exposure technique
SCC	stress corrosion cracking
SEOP	standard and emergency operating procedures
SiC	silica carbide
SPD	severe plastic deformation
UIT	ultrasonic impact treatment
USSP	ultrasonic shot peening
wt%	weight percent

THIS PAGE INTENTIONALLY LEFT BLANK

ACKNOWLEDGMENTS

I owe endless gratitude to several organizations and individuals for their support of this research. Expressing that gratitude here is hardly sufficient, but it is my hope that the research speaks for itself and all parties feel their time, efforts, and funding were well spent. For anybody I forget, I offer my apologies. This work is far reaching and the number of people involved is far reaching.

Professor Luke Brewer continually dedicates an unprecedented amount of time and effort to his students and research. He ensured that this work was set up for success every step of the way by coordinating permission, coordinating funding, imparting knowledge, providing guidance, and so much more. I am grateful for this opportunity to impact the future of the U.S. Navy.

Dr. Kim Tran at Naval Surface Warfare Center Carderock Division was involved throughout my research with the provision of samples, funding, and advice. I feel honored that she was willing to share her vast amount of knowledge in this field of study. Between her and Professor Brewer, I could not have asked for a better set of advisors.

I am very grateful for funding for this research provided by the Office of the Secretary of Defense-Corrosion Policy and Oversight Office. Specifically, Mr. R. Hays, Deputy Director, generously provided financial support and enthusiasm for the approach, the instrument, and the labor needed begin this x-ray residual stress approach.

Site visits were conducted at The Navy Yard in Philadelphia and onboard *USS Bunker Hill* (CG52). The support of the personnel at each location was astounding. A special thanks to Bobby Sparks, Alan Karpovitch, and David Sparkuhl for making the visits educational and successful. Additionally, the crew of the *USS Bunker Hill* was overwhelmingly supportive of our work and went out of their way to aid our research. Dr. Bill Golumbfskie made a special site visit to the location of our field work to offer the use of his *in situ* metallography equipment, which will prove useful in future work. Thanks to all who made the site visits a success.

Lastly, the process of obtaining permission to conduct open beam x-ray diffraction was a giant hurdle we overcame in the process of conducting this research. The guidance and support of the Naval Postgraduate School radiation safety officer, Mr. R. J. Greve, is greatly appreciated.

I. INTRODUCTION

A. MOTIVATION

The United States Navy funds ship design and shipbuilding under the expectation that a ship will remain active for the entire specified service life or longer, typically several decades. This approach allows for proper budget planning and a fully operational fleet. Life cycle maintenance plans are developed in the design phase of a ship class. They act as a means of prolonging ship life by providing a schedule for conducting major tasks onboard including those that require dry docking. Under the current budget constraints, ship maintenance is critical since the rate of shipbuilding is reduced. Despite rigorous maintenance cycles, it is difficult to mitigate complications that each ship design will encounter.

The Ticonderoga class cruisers represent one such challenge currently facing the U.S. Navy maintenance community. Stress corrosion cracking (SCC) plagues the superstructure of these cruisers (Figure 1) [1]. There were 27 total cruisers built in this class with a designated service life of 35 years each [2]. The class's namesake, *USS Ticonderoga* (CG47), was commissioned in 1983 and decommissioned a short 21 years later. The subsequent four ships in the class (CG48-CG51) experienced similar periods of commission, causing the U.S. Navy to lose roughly 15 years of service per vessel and decreasing the U.S. Navy's operational capability. These five ships were decommissioned early due to the inferior defense capabilities as compared to the remaining cruisers in the class. Twenty-two Ticonderoga class cruisers remain in service. The oldest remaining, *USS Bunker Hill* (CG52), has been in service for 28 years; while the youngest, *USS Port Royal* (CG73), has been in service for 20 years. It is imperative for fiscal stability and operational capability that the remaining cruisers achieve the 35 year service life. The U.S. Navy has an interest in SCC solutions due to the life cycle maintenance currently being conducted to sustain the remaining Ticonderoga class cruisers to prolong their service life [1]. The U.S. Navy also has concerns that relate to other ship classes including the littoral combat ship that have since been constructed of similar material and may present SCC problems in the future.

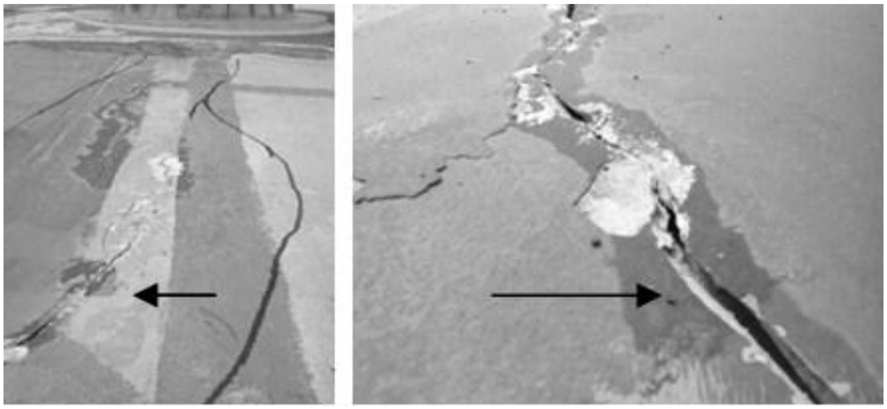

Figure 1. Stress corrosion cracking in AA 5456-H116 (from [1]).

The challenges of SCC are a present concern for the U.S. Navy due to materials and strenuous operational environment [1, 3, 4]. SCC may lead to problems with watertight integrity among other issues in U.S. naval vessels [1]. Both aluminum alloy (AA) 5456 and AA5083 are common alloys used in shipbuilding and exceed the 3 weight percent (wt%) magnesium threshold over which sensitization is a concern (compositions in Table 1 and phase diagram in Figure 2).

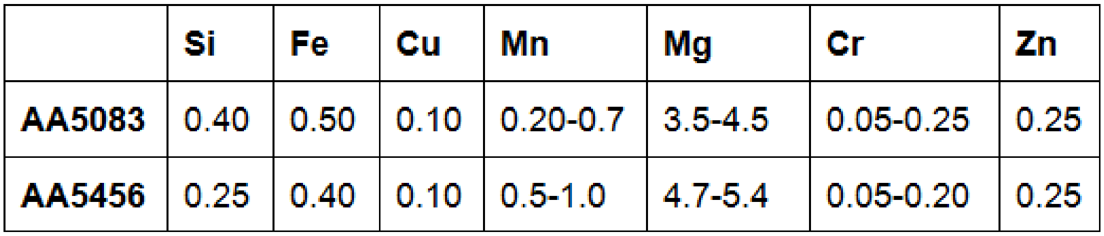

	Si	**Fe**	**Cu**	**Mn**	**Mg**	**Cr**	**Zn**
AA5083	0.40	0.50	0.10	0.20-0.7	3.5-4.5	0.05-0.25	0.25
AA5456	0.25	0.40	0.10	0.5-1.0	4.7-5.4	0.05-0.20	0.25

Table 1. Weight percent of alloying elements in common aluminum alloys used for shipbuilding (from [5]).

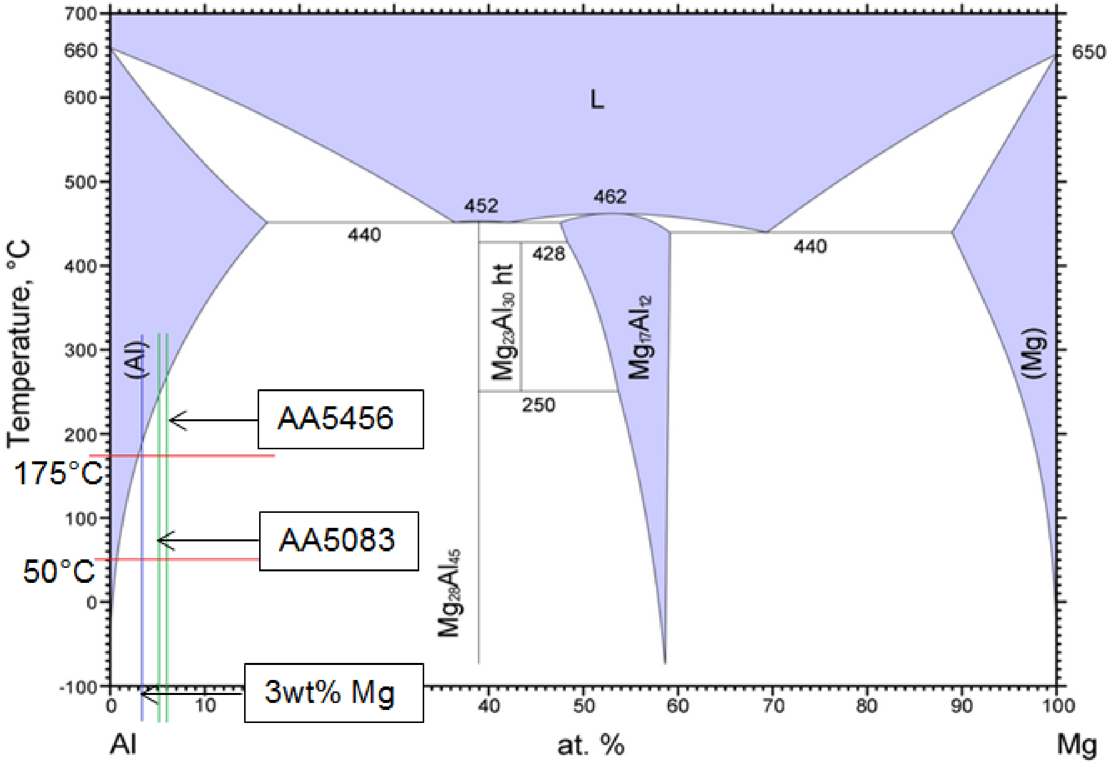

Figure 2. Aluminum magnesium phase diagram with 3 wt% Mg, AA5083, and AA5456 highlighted (after [6]).

Common areas of operation expose U.S. naval vessels to elevated air temperatures up to 40°C that can result in extended periods of time with surface temperatures in excess of 60°C, triggering the sensitization. Due to the constant marine and coastal environments, the ships are exposed to chloride-containing solutions nearly all of the time. The final element for SCC, tensile stress, is present as a result of applied load on the structure and exacerbated by residual stresses induced by welding used for shipbuilding and ship repairs. The superstructure in Ticonderoga class cruisers is the primary focus of this work. The superstructure is attacked due to the air-seawater environment promoting constant repassivation (oxygen in air) and breakdown of the passive oxide layer (chlorides in seawater).

B. LITERATURE REVIEW

SCC is a type of environmentally assisted cracking. It results from a combination of microstructural susceptibility, tensile stresses (residual and/or applied), and a corrosive environment (commonly represented by the Venn diagram in Figure 3). The environmental aspects that cause SCC depend on the vulnerabilities of a specific material [7, 8]. SCC can initiate due to surface discontinuities or corrosion pits and by intergranular corrosion or slip dissolution. It should be noted that these conditions do not guarantee that SCC will occur. To reiterate, SCC is a “synergistic stress-corrosion interaction” [8] and requires all three conditions in Figure 3. Because the chemistry at the crack tip is significantly different than that in the bulk conditions, crack propagation in SCC may occur due to conditions that are different than those under which the crack initiated. Two categories encompass all proposed crack propagation mechanisms for SCC: chemical dissolution models and mechanical fracture models. For a single instance of SCC, several mechanisms might drive SCC. The influence of sensitization and the chemistry of corrosion environment will both affect the exact mechanisms of SCC that are operative; however, the primary focus of this research is the tensile stress aspect required for SCC.

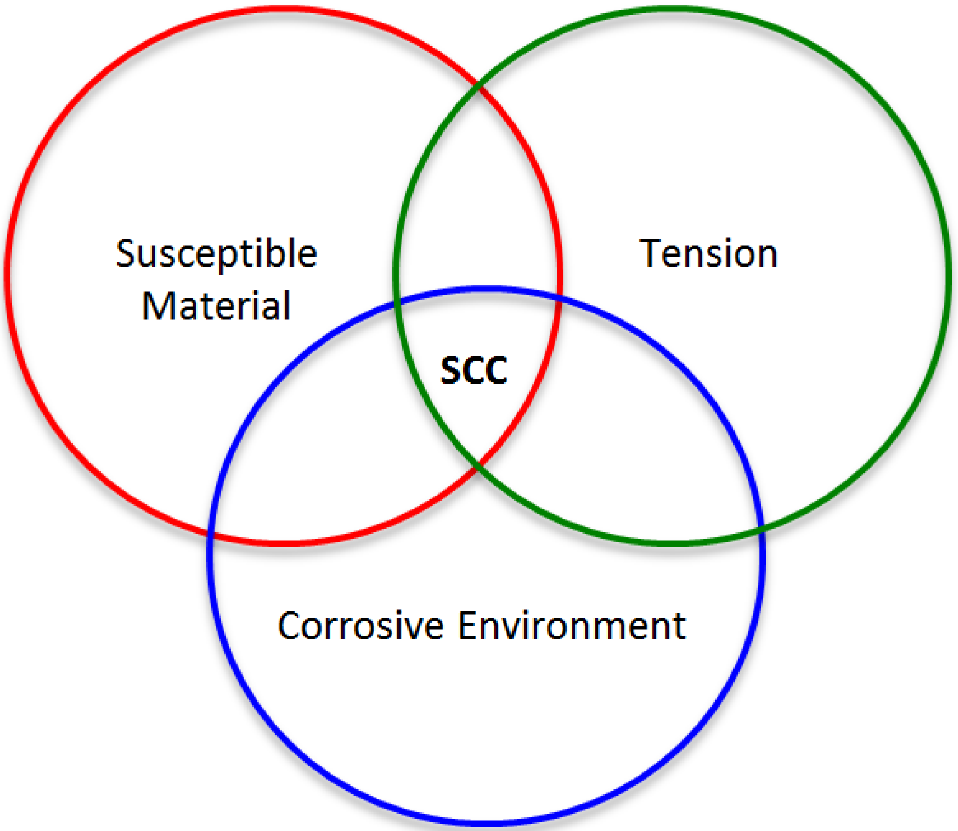

Figure 3. Venn diagram displaying the three factors required for stress corrosion cracking.

1. SCC in 5xxx Series Aluminum Alloys

The 5xxx series aluminum alloys are ideal candidates for maritime use because of their resistance to general corrosion (SCC is a result of localized corrosion), relatively high strength, and weldability (vital for shipbuilding and repairs) [9]–[11]. The primary alloying element, magnesium, provides the needed strength without negatively impacting the general corrosion resistance, ductility, and weldability [10, 11]. Additionally, in comparison to other shipbuilding materials such as steel, aluminum is lightweight and workable [3, 10]. Finally, 5xxx series aluminum alloys form a particularly durable protective oxide layer in high oxygen environments (i.e., the superstructure in air) [3, 12]. Nonetheless, SCC remains a source of failure for 5xxx series aluminum alloys due to the combination of operating temperatures, the marine environment, and both loading stresses and stresses induced by welding.

a. Susceptibility

A material's susceptibility to SCC is often described as sensitization. Sensitization is a change in metallurgical or microstructural state that causes the material to react with its environment in a transgranular or intergranular cracking manner; appropriately termed transgranular stress corrosion cracking (TGSCC) and intergranular stress corrosion cracking (IGSCC) [8]. The type of sensitization (and subsequent cracking path) will depend on the material but may include changes in one or more of the following ways due to environmental factors such as pH, temperature, and solute concentration as discussed by Jones [8]:

- Stability of the passive film and phase distribution
- Alloying elements affecting local stability of passive film
- Segregation of elements to the grain boundary, altering the chemistry compared to the local matrix
- Additions to the matrix may affect the chemistry as the crack intersects and the environment reacts with them
- Dealloying

Sensitization in 5xxx aluminum alloys is directly related to the magnesium content used to strengthen the alloy and temperature (due operational requirements and welding) [11, 13]. At temperatures above 50°C (122°F), Al-Mg alloys containing greater than 3 wt% magnesium can become sensitized over time as a result of the formation of a continuous secondary (or beta-Al_3Mg_2) phase at the grain boundaries [10], [13]–[18]. Grain boundary sensitization results from this change in grain boundary chemistry making the boundaries anodic with respect to the grain interior [7]. This microstructural variance causes the SCC to propagate preferentially along the grain boundaries, a phenomena termed Intergranular stress corrosion cracking (IGSCC), because the boundaries corrode more rapidly with the surroundings than the grain interior matrix. Holtz et al. observed this phenomenon in AA5083-H131 at temperatures as low as 70°C

[19]. After roughly 1,000 hours, the β phase begins to precipitate on the grain boundaries (Figure 4). When the distribution of β phase on the grain boundaries becomes nearly continuous, the material is considered to be fully sensitized and will be susceptible to both SCC and corrosion fatigue. This transformation has been qualitatively observed using such methods as transmission electron microscopy and quantitatively observed using the ASTM G67 nitric acid mass loss test (NAMLT) [16, 19, 20].

The degree of sensitization, DOS, is most often measured using NAMLT [21]. A sample of the sensitized aluminum material with known mass is placed in nitric acid [22]. The nitric acid dissolves β phase precipitates and the mass of the remaining sample is measured to determine the mass loss. The mass loss normalized by the surface area exposed is an indicator of the degree of sensitization. A safe and acceptable NAMLT value is less than or equal to 15 mg/cm^2 [21]. This means that the level of sensitization is within a safe operational limit. In the experiments conducted by Holtz et al, after only 1,000 hours at 70°C they recorded NAMLT values of 30 mg/cm^2 for AA5083-H131, which is considered the critical degree of sensitization. At 3,000 hours, only 125 days, a continuous β phase is present along the grain boundary resulting in a NAMLT above 40 mg/cm^2, which is considered severely degraded [19]. The process occurs faster at higher temperatures. Additionally, for extended periods of elevated temperatures, the continuous film will widen [20]. When conducting fatigue testing, they found that the stress threshold is dependent on NAMLT values, regardless of the temperature of sensitization. This suggests that sensitization at lower temperatures may take longer, but the effects are equally as detrimental.

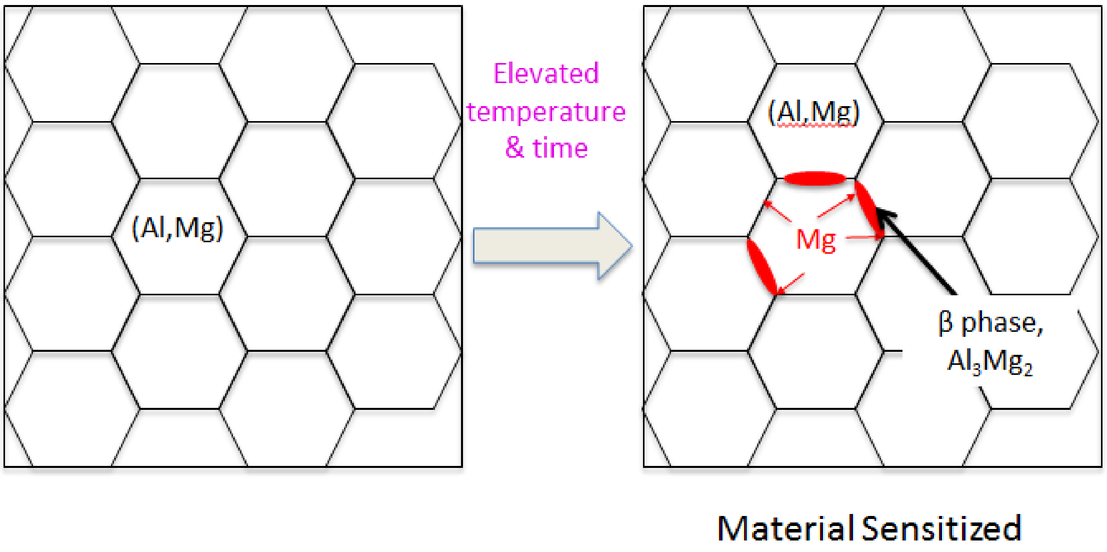

Figure 4. Depiction of sensitized 5000 series aluminum alloy (from [23]).

b. Corrosive Environment

A corrosive environment is one in which a particular material oxidizes resulting in deterioration. The environment that causes corrosion will vary based on the material [8]. Not all detrimental combinations are known and at times the 'known' information can be misleading because of vast differences that may occur between experimental and service conditions. The rate of deterioration and the byproducts of the reaction are dependent upon the interaction between the environment and specified material. Temperature, solution velocity, pH, and solute species/concentration are examples of environmental factors that play a role in the rate of material deterioration [7, 8]. In some cases, it is possible to control these variables or to at least minimize their effect on the material. Proper material selection and processing methods are required in instances when controlling the environment is not an option.

An appropriate material for a given environment will have a stable, passive oxide layer on its surface. The passive oxide layer acts as a nonreactive, protective barrier between the base metal and environment. The layer is good for the prevention of general and uniform corrosion [8]. It forms due to a reaction between the base metal and the environment under a set of conditions predicted using Pourbaix diagrams (example of aluminum in water shown in Figure 5), which are potential voltage versus pH graphs specific to each element and environment (solution, temperature, etc.) [7, 8, 12].

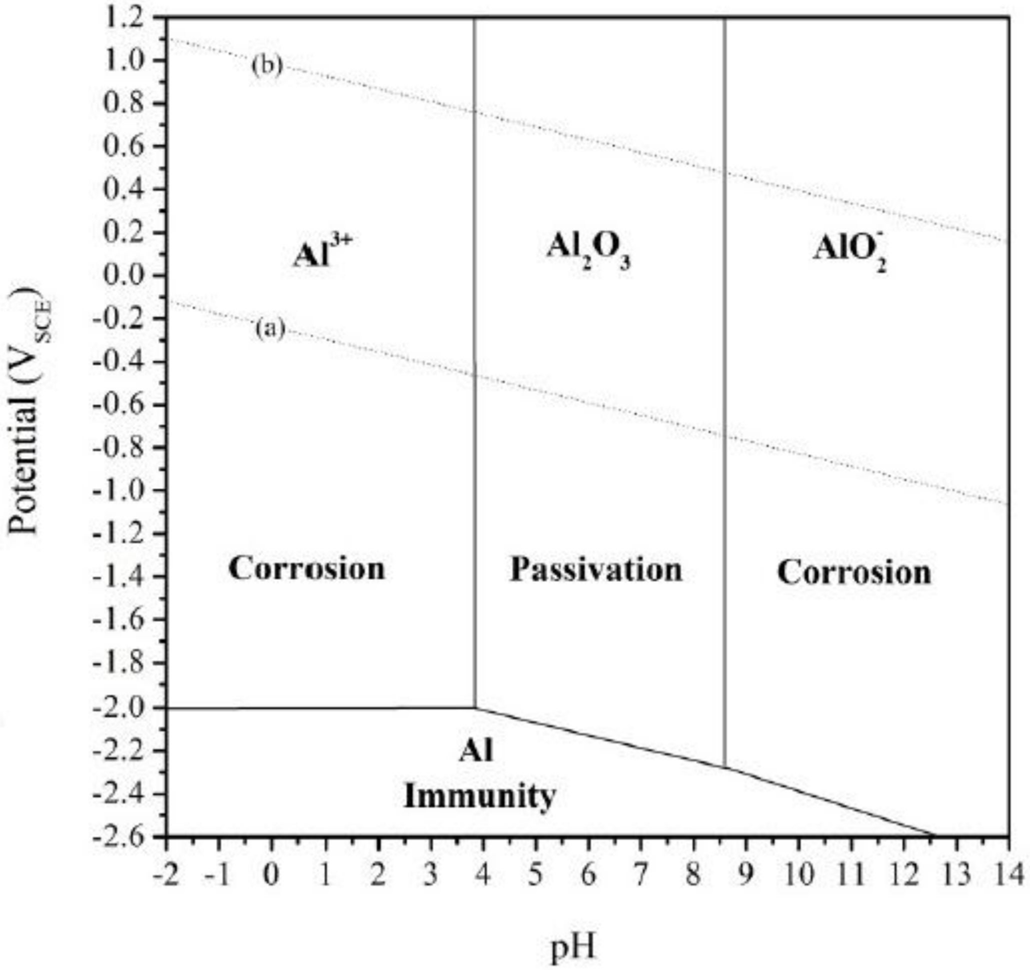

Figure 5. Example of Pourbaix diagram for aluminum at 25°C in aqueous solution (adapted from [24] by [12]).

Overlaying Pourbaix diagrams for the dominant three or four elements in an alloy is a common method of estimating the passive conditions for an alloy when a single diagram has not been determined. Ideally, the predominant elements of an alloy will overlap such that regions of corrosion will be strengthened by regions of immunity or passivity of other elements allowing for a broader region of passivity in the alloy as a whole (resulting in a smaller region of reactivity). The applicability is limited due the experimental parameters as compared to service conditions. The potential versus pH diagram for AA5083 was developed based on experimental data of the alloy in a 0.5 molar (M) sodium chloride solution [12]. In the sodium chloride solution, the AA5083 oxide layer becomes corrosive in regions where pure aluminum is passive in a solution of water. This diagram offers a more comprehensive look at how 5xxx series aluminum alloys will react in the presence of chloride (Figure 6), which more closely represents that found in marine environments.

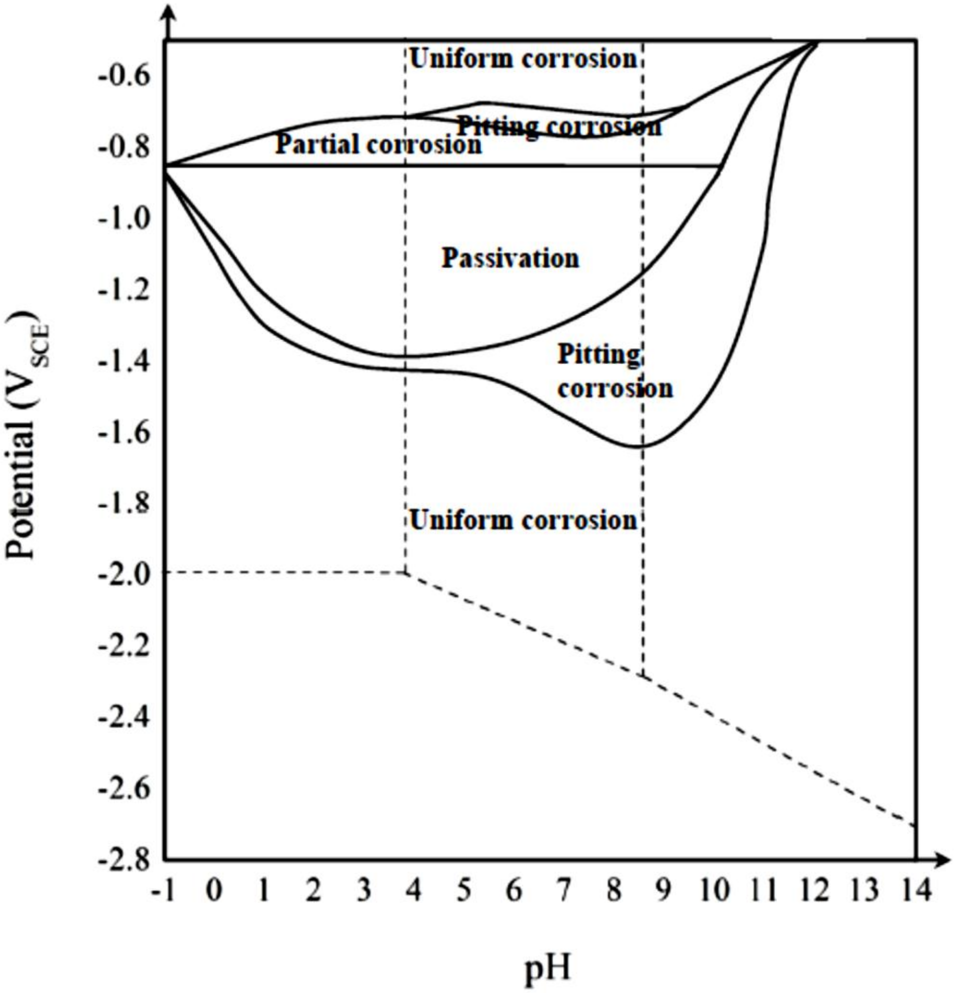

Figure 6. Pure aluminum Pourbaix diagram with an overlay of the corrosion modes for aluminum alloy 5083 determined experimentally in 0.5 M sodium chloride. Areas of corrosion and passivity are labeled (from [12]).

The rate of corrosion is controlled by ionic transport across the passive oxide layer. This layer is often quite thin, and in aluminum is only about 30 nanometers thick [25]. A slight scratch during service or a defect from manufacturing (any surface discontinuity) exposes the base metal to the surrounding corrosive environment [8]. In the ideal environment, damage to the passive oxide layer will be healed by repassivation. The oxide layer will re-form such that the base material is once again protected; even in a mildly reactive solution (low concentration and activity), the concentration of the reactive species (i.e., chloride ions) increases exponentially at the crack tip, causing an increased breakdown of the passive oxide layer and continual removal of material. Thusly, the presence of a passive oxide layer in an alloy cannot be the sole determination of the alloy's resistance to corrosion and can, in fact contribute to SCC [7, 12].

Two predominant theories were found when researching the SCC mechanisms in 5xxx series aluminum. Both theories are supported by Arnott, Baxter, and Rouze who were able to discern that for AA7075-T6 higher rates of repassivation result in more rapid cracking and lower rates of repassivation results in slower crack propagation in SCC [25]. Several older studies suggest that the film rupture of the passive oxide layer is a means by which SCC propagates in aluminum alloys [7, 25, 26]. Under constant stress, the oxide layer has an opportunity to repassivate in an oxygen rich environment (such as the air) [3, 26]. The passive oxide layer offers protection, but tensile stresses disrupt the layer at the crack tip, exposing base metal to the corrosive environment [25]. The base metal will continue to repassivate, but the stress concentration at the crack tip will cause the crack to continually propagate. Another SCC mechanism theory suggests that a combination of the following steps causes SCC in aluminum instead of film rupture [8, 18, 27]:

- local anodic dissolution of the β phase
- hydrogen uptake due to the production of hydrogen during dissolution
- hydrogen embrittlement of local metallic material
- crack extension along the grain boundary
- further exposure of the beta phase to local anodic dissolution.

In this mechanism, surface defects and the presence of chlorides also cause crack initiation and propagation. However, the chemical change and resultant embrittlement makes the material less resistant to the tensile stresses present. This process is not solely dependent upon the brittle nature of the passivating oxide film as previously postulated [28].

c. Tensile Stresses

Tensile residual or applied stresses are the final requirement for SCC. Applied stresses are due to loading induced as a result of the various weapons systems, radars, etc. supported by the superstructure. Residual stresses are those that exist when the material is not supporting a load. They are the result of manufacturing, construction, and repairs. Applied stresses are those that exist when a load is being supported by the material. Tensile yield stress is the total tensile stress a material can withstand. Combined tensile stresses less than this amount will be acceptable unless a flaw, such as a microcrack, exists in the material. SCC is of particular interest because failure occurs under constant loading conditions within the design capabilities of a material due to the combination of residual stresses, corrosive environment, and susceptible material [8].

Under the assumption that a flaw exists, it is necessary to consider the stress intensity value, K. The equation below provides the simplest form of the relationship between stress intensity, acting stress, and existing crack length, where “Y” accounts for the crack geometry [7].

$$K = \mathrm{Y}\sigma\sqrt{\alpha} \qquad \text{Equation 1.}$$

The stress intensity determined using Equation 1 must be compared to the material’s fracture toughness, K_{IC}. Under inert conditions (i.e., no corrosion), K must exceeds K_{1C}, for crack propagation to occur. This can be due to the length of the crack reaching the critical crack length, α_c, under the given stresses or due to the stress, σ_c, reaching a critical value for the given crack length. In a corrosive environment, a modified, and usually significantly lower, stress intensity factor, K_{ISCC} must be considered [7, 8, 14]. Theoretically, K_{ISCC} correlates with the stress below which crack propagation will not occur [8]. K_{ISCC} is determined not only based on material properties, but also based on the environment. This value is used under the assumption that the size of the plastic zone at the crack tip is small [8, 29].

While considered weldable, 5xxx aluminum-magnesium alloys can possess substantial tensile residual stresses after welding. Welding is used in both construction of and repairs to maritime vessels. Heat input and cooling rate from welding affect the temperature gradient induced, which leads to the residual stresses that contribute to SCC as discussed above [3, 30]. James et al. measured the residual stresses as a result of gas metal arc welded (GMAW) butt welds in AA5083 using synchrotron x-ray diffraction (Figure 7) [31]. Their findings show GMAW welding induces tensile residual stresses up to 100 megapascals (MPa) to a depth 7 mm below the surface in the heat affected zone (HAZ). Sanders and McDowell demonstrated that the parameters of the weld affect the magnitude of the tensile stresses (e.g., geometry, orientation, and roughness of weld) [3]. They concluded orienting the weld in the direction of the applied load and lower angle at the toe of the weld increase fatigue life in AA5456 and AA5083. It has been shown that excessive preheating prior to welding can cause sensitization of AA5083 [13]. Previous reports about sensitization suggest that there are concerns that heat input from repair welding on sensitized material may cause the material to further sensitize [13, 14, 17]. Once 5xxx series aluminum sensitizes, tensile stresses in conjunction with the corrosive atmosphere leads to IGSCC (Figure 8).

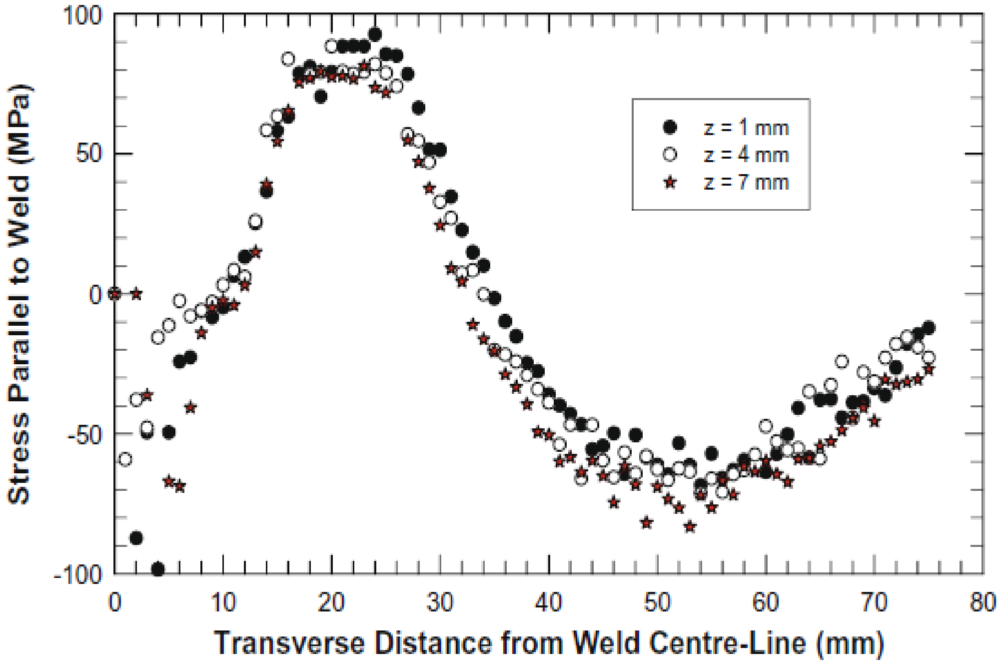

Figure 7. Residual stresses at multiple depths as a result of GMAW butt welds in AA5083 (from [31]).Measurements were conducted using synchrotron x-ray diffraction.

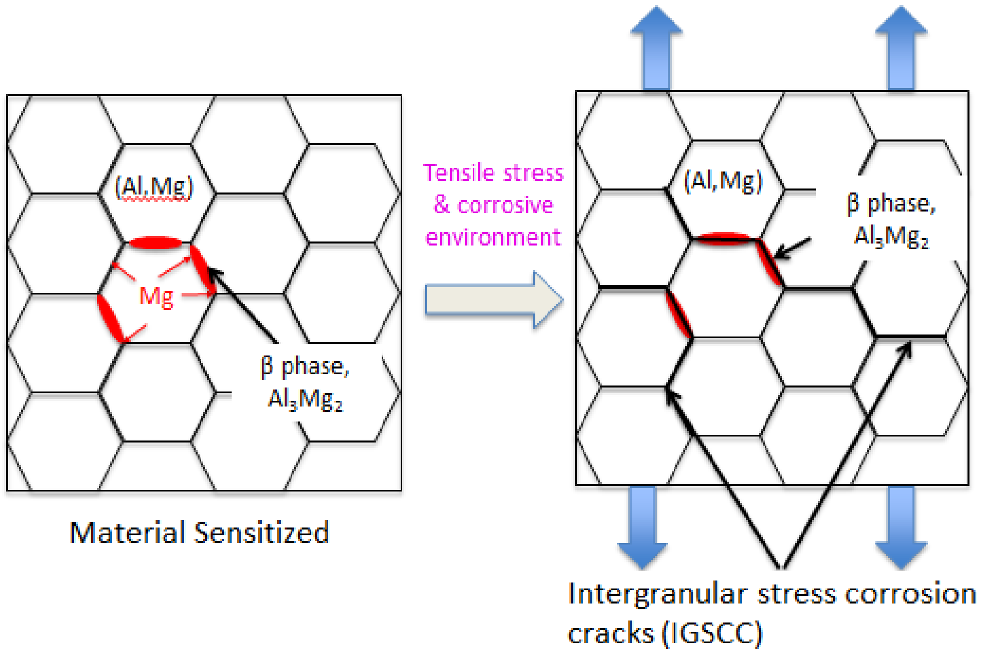

Figure 8. Intergranular stress corrosion cracking due to a sensitized material subject to tensile stresses and a corrosive environment (from [23]).

2. Mitigating Stress Corrosion Cracking

In order to mitigate SCC, it is necessary to remove one of the three elements: sensitization, corrosive environment, or tensile stresses. Local heat treatment has been shown to locally reverse sensitization without further inducing sensitization in the surrounding material [32]. The method was successfully used in a portable configuration and appears to be a promising solution for returning the sensitized AA5456-H116 to a non-sensitized condition. Doping was shown to reduce SCC susceptibility in 7xxx series aluminum alloys by altering the composition of the grain boundaries even in peak aged condition, suggesting the sodium chloride environment no longer poses a severe corrosive threat because there is no longer a susceptible microstructure [33]. Friction stir welded (FSW) AA5083 showed improved stress corrosion resistance compared to GMAW AA5083 because the precipitates are more uniformly distributed throughout the grain instead of along the grain boundaries as required for IGSCC [34]. However, FSW still produces a significant amount of heat input and resultant residual stresses that will contribute to SCC if the material is exposed to a corrosive environment and becomes sensitized due to other contributing factors (Figure 9) [35]. The remaining discussion will focus on mitigating tensile stresses associated with welding.

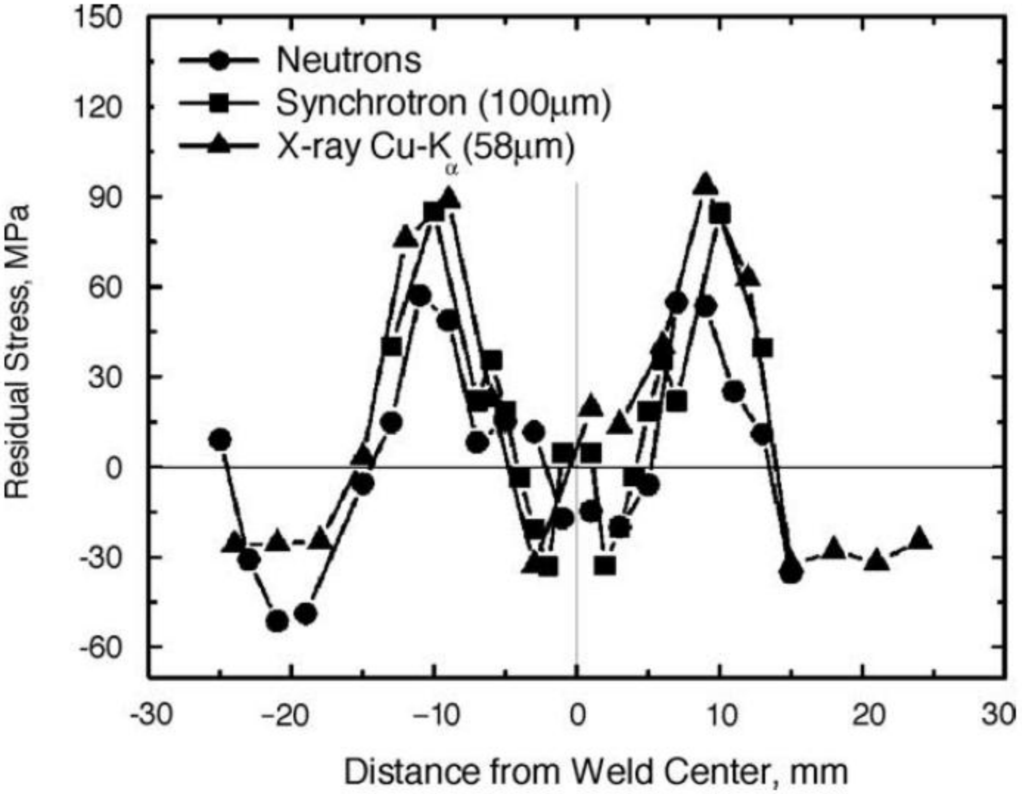

Figure 9. Diffraction measurements of residual stresses induced by friction stir welding of 6013Al-T4 as presented by Mishra and Ma (from [35]).

Reducing, or even reversing, the tensile residual stress on the surface of aluminum alloys through peening approaches shows potential for mitigating SCC. Peening has long been a method used in industry as a method to create the compressive surface stresses needed to combat fatigue and SCC [36]–[47]. Over the years, the method has been refined, but the concept remains the same. Each method seeks to bombard a surface with a specified component (e.g., hammer, small metallic spheres, lasers) that plastically deforms the surface and, in turn, creates the compressive stresses needed to increase the life of the material [29]. However, these processes can be quite complicated and imprecise in anything less than ideal environment (i.e., laboratory). Laser peening, shot peening, low plasticity burnishing, and ultrasonic impact treatment are just a few peening methods shown to induce compressive stresses on the surface of a material.

Each peening method presents its own set of advantages and disadvantages. Laser peening tends to be the most costly due to the elaborate technology and required operator skillset. A laser beam is aimed at the desired location and generates a shockwave on the surface of the material, plastically deforming it, and thus generating a compressive, elastic stress. Laser peening offers superior control over parameters and minimal surface deformation [37]. Portable laser peening methods are available and used in primary water SCC repairs in power plants [48]. Shot peening is a more basic process involving projecting small spheres at high speed towards the surface of the material. Shot peening reliably induces compressive stresses, but results in surface deformations, a wider range of induced stresses, and compressive to depths of only about 0.2 mm [49]. Portable shot peening is in use, but the equipment is bulky and difficult to use in confined spaces. Low plasticity burnishing is a process where a single ball with a force behind it is rolled across the surface of a material [50]. It is a highly controlled process that produces compressive stresses and leaves behind a “mirror finish” on the surface of the material. The system configuration is not portable and appears to be a time consuming process due to the use of a single rolling ball. The attributes of each of these will be briefly compared to ultrasonic impact treatment, which was used in this research.

3. Ultrasonic Impact Treatment

Ultrasonic impact treatment is a portable, hand held, severe plastic deformation (SPD) process that uses pins vibrating at an ultrasonic frequency to induce compressive stresses [40, 43]. Other SPD methods include equal channel angular extrusion (ECAE), accumulative roll bonding (ARB), and ultrasonic shot peening (USSP). SPD methods are known for inducing high plastic strains at the microstructural level, but preserving the overall dimensions of the material [45]. In general, it is difficult or impractical to implement SPD in a field environment due to the complexity of the requirement equipment. UIT is a notable exception. Not only is it more cost effective than other SPD methods, but UIT mitigates the portability complications presented by both SPD and other peening methods because it is readily useable for field applications [45].

UIT has been successfully and commercially applied in the field by Applied Ultrasonics-Esonix (AU) and by Empowering Technologies-Sonats to increase fatigue resistance and reduce SCC in various metal structures [41]–[47], [51]–[53]. The AU process involves the use of a pin tool that behaves like an ultrasonic transducer that outputs continuous ultrasonic impulse or vibrations to treat the material's surface. The technology is based on converting the ultrasonic oscillations of the transducer into impulses of ultrasonic impacts [47]. The output end employs needle indenters, strengthened with hard materials such as carbide containing alloys or artificial diamonds that are directed at the surface and are in continuous contact with the surface of the material.

The SONATS process is based on a technology that is known as STRESSONIC™. The STRESSONIC™ generator (Figure 10) creates a digital sine wave with an ultrasonic frequency (generally 15, 20, or 40 kHz) that is converted to a mechanical signal by a piezo-electric emitter. The mechanical signal is amplified by a series of boosters and a sonotrode [54]. The mechanical energy of the sonotrode is then transmitted to the indenters or shot peening media. No ultrasonic waves are transmitted to the component to be treated but rather just mechanical energy. The vibration amplitude of the sonotrode ranges from 10 µm to 250 µm.

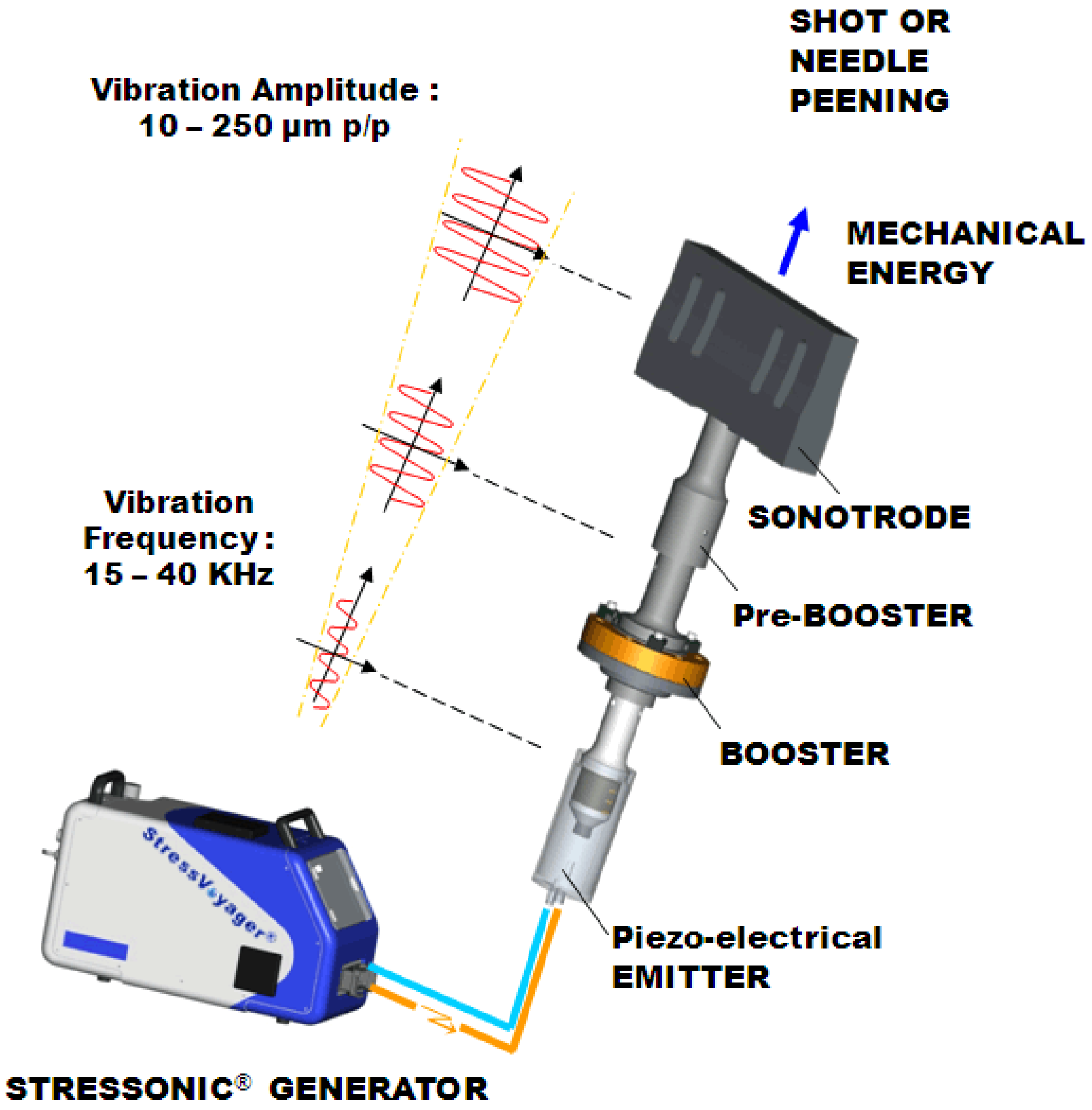

Figure 10. The schematic of the STRESSONIC principle shows the location of the various portions of the SONATS UIT device (from [54]).

Both machines include a generator box and a handheld tool that allows the operator to apply UIT to the work piece (similar to Figure 11). Single or multiples pins can be selected based on the size and location of the UIT area. There are multiple pin sizes available for each tool. The amplitude, generator frequency, impact frequency, load amplitude, feed rate, and pressure have all been varied in laboratory experiments. A summary of these parameters is provided in Table 2.

Figure 11. Sonats portable ultrasonic impact treatment machine (from [52]).

Table 2. UIT parameters used in various studies.

Year, Author, Reference	**Parameters**							
	Material	Single/ Multi Pin Tool	Pin Dia. (mm)	Carrier Freq. (kHz)	Impact Freq. (Hz)	Load Amp. (µm)	Feed Rate (mm/min)	Other
1985/Mikheev et al. [43]	Steel	a. Single b. Multi	16	27.5			≤500	
2002/Statnikov et al. [47]	Steel	Multi	a. 5 b. 5 then treated w/ 3					
2003/Cheng et al. [57]	Steel		3	27	100			
2006/An et al. [45]	AA2024		5	36	a. 260 b. 220	a. 18 b. 15	a. 400 b. 1000	Normalized impact: 64 impulses
2007/Rodopoulos et al. [56]	AA2024		5	36	260			
2008/Liao et al. [58]	AA7075	Multi	5	36		20	400	Normalized impact: 64 impulses Average power: 300W
2010/Castillo-Morales et al. [44]	AA2024		a. 6.35 b,c,d. 5	a. 27 b,c,d. 36	a. 236 b. 260 c,d. 220	a. 22 b. 18 c. 15 d. 10	a,b. 400 c,d. 1000	Normalized impact: 64 impulses

Year, Author, Reference	Parameters							
	Material	Single/ Multi Pin Tool	Pin Dia. (mm)	Carrier Freq. (kHz)	Impact Freq. (Hz)	Load Amp. (μm)	Feed Rate (mm/min)	Other
2011/Scheck et al. [40]	AA5456			27		22	100	Power Consumption: 80V, 11.2A
2011/Goudar et al. [58]	Stainless Steel		6.3	20-30			150	
2012/Okawa et al. [42]	Steel		3	27				
2013/Mordyuk et al. [46]	Al-6Mg Alloy	Single		21.7		22		Power Output: 0.3kW
2013/Tran et al. [41]	AA5456	Multi	3	27			100	Power Consumption: 80V, 11.2A

UIT has been shown to be a viable solution improving the material properties of aluminum alloys and steels. UIT induces compressive stresses on the order of -175 MPa in aluminum alloys and -500 MPa in steels, eliminating tensile stresses from welding [42, 44, 46], [55]–[58]. On average the compressive stresses reach depths ranging from 1.5 to 2 mm (Figure 12) [44], [56]–[58], but have been shown to reach up to 4 mm in thick specimen [55]. These compressive stresses have been shown to improve the fatigue life of materials [42]–[44], [46, 47, 56, 57]. The number of cycles to fatigue is dependent upon the material and the conditions under which the fatigue testing was conducted. However, across the board, research suggests that UIT increases fatigue life as shown in Table 3. The microhardness has been shown to be highest at the treated surface and decrease to the match that of the base material at a depth 1–2 mm in aluminum alloys [40, 44, 46, 56]. The severe impact caused by UIT led to research about the effect on the surface and subsurface microstructure. UIT impacts the material causing deformation at the surface. Crater depths have been observed over a range of values from 0.5 to 2.5 μm in various aluminum alloys [44, 46]. SEM images show that grain size decreases at the surface of the material due to recrystallization but these smaller grains are not present below the surface [45, 53]. Studies in surface and subsurface microstructural evolution also revealed that UIT results in twinning, microbands, and micro-tearing in various aluminum alloys [41, 45].

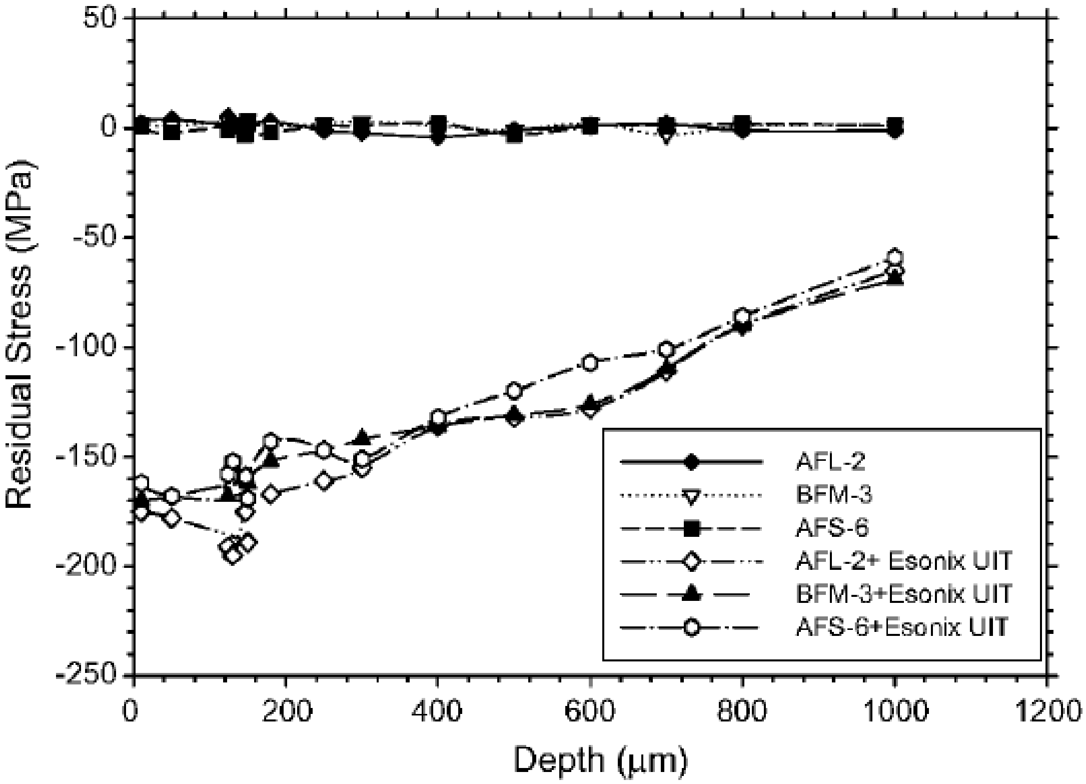

Figure 12. XRD residual stress depth resolved measurements of varying levels of exfoliated AA7075-T6511 following surface UIT. Lightly, moderately, and severely (AFL, BFM, and AFS, respectively) exfoliated specimen were tested for residual stresses before and after UIT (from [58]).

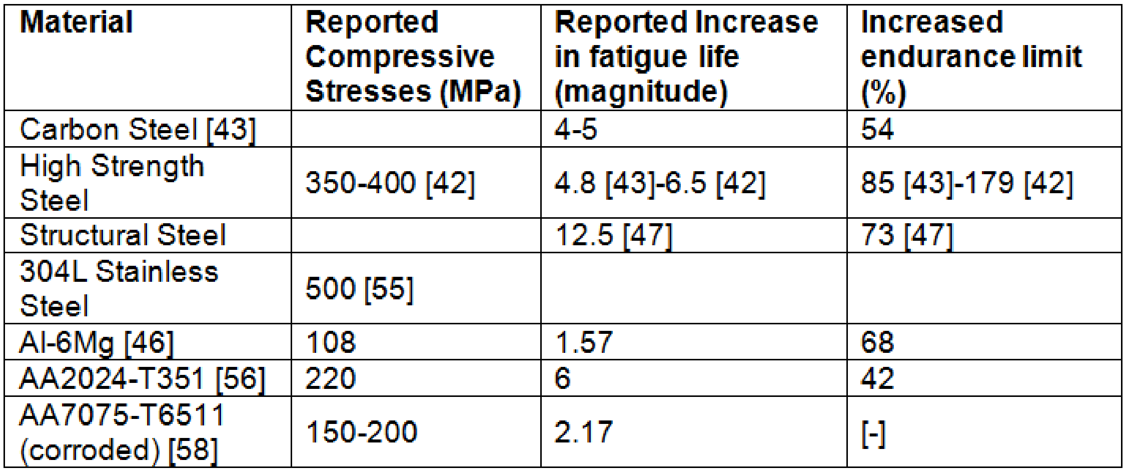

Material	Reported Compressive Stresses (MPa)	Reported Increase in fatigue life (magnitude)	Increased endurance limit (%)
Carbon Steel [43]		4-5	54
High Strength Steel	350-400 [42]	4.8 [43]-6.5 [42]	85 [43]-179 [42]
Structural Steel		12.5 [47]	73 [47]
304L Stainless Steel	500 [55]		
Al-6Mg [46]	108	1.57	68
AA2024-T351 [56]	220	6	42
AA7075-T6511 (corroded) [58]	150-200	2.17	[-]

Table 3. Aluminum alloys and steels with reported values for compressive stresses and fatigue improvments as a result of UIT.

Several UIT parameters have been researched with respect to their effect on fatigue life or microstructure. In research and practice, UIT is conducted at the toe of the weld or over the entire surface of the region of concern for the material. Mikheev et al. determined that using a single pin tool along the toe of the weld (resulting in a single line of width equal to the diameter of the pin) and using a multi pin tool on the surface of the butt joint was (resulting in a treated area between 20-60 mm) both increased the fatigue life of the specimen, but the data was inconclusive as to which method was ideal for fatigue life [43]. Various pin sizes are available for the UIT handheld tool. Results obtained by Statnikov et al. suggest that using a 3 mm pin results in a roughly 10 percent increase in fatigue life compared to a 5 mm pin for structural steel [47]. An et al. compared other parameters such as impact frequency, load amplitude, and feed rate for microstructural variations in AA2024-T351 [45]. These combinations suggest that slower feed rate/larger amplitude under load result in larger grain sizes at the surface and smaller grain sizes at the subsurface. Castillo-Morales presents the most comprehensive research found on UIT parameters [44]. Pin size, carrier frequency, impact frequency, load amplitude, feed rate and pressure were varied for UIT conducted on AA2024-T3. Based on their findings, the fatigue life was reduced significantly where the treatment per area was highest. Of the research conducted there has been little systematic testing of the various UIT parameters and their relationship with the residual stresses inducted as a result of UIT.

In the decades since UIT was developed, only a few systematic investigations into the advantages and disadvantages of UIT in 5xxx series aluminum alloys have been conducted [40, 41, 53]. In order to be effective for ship repairs, UIT must be shown to successfully mitigate SCC in sensitized 5xxx aluminum without creating additional material concerns. Standardized, optimized UIT parameters are needed for use during construction and repairs of 5xxx aluminum alloys. Understanding the impact of individual parameters on residual stresses and microstructure will fill a void where information is lacking. UIT has been shown to mitigate the tensile stresses induced by welding, but the direct connections between UIT process parameters and the resultant surface residual stresses have not been determined for the 5xxx series alloys.

4. X-ray Diffraction Measurements

Since UIT and other peening methods depend upon compressive residual stresses for mitigation of fatigue and SCC, the capability to measure surface residual stresses is vital. Residual stresses can be measured by both destructive (e.g., hole-drilling, slit-compliance) and non-destructive methods (e.g., x-ray, synchrotron x-ray, neutron diffraction) [59]. X-ray and neutron diffraction have both been used to measure residual stress distributions in aluminum welds. In particular, James et al. have used synchrotron x-ray diffraction to measure the residual stress distribution in GMAW welds of AA5083 (Figure 7), Tensile Stresses section above). They observed tensile stresses as high as 100 MPa parallel to the weld. While synchrotron x-ray and neutron diffraction are able to measure three-dimensional distributions of residual stress through thick (10–30 mm thick) aluminum structures, they require large, special purpose facilities that cannot be used to perform field measurements.

The comparison of residual stress measurements using x-ray diffraction, synchrotron, and neutron diffraction has demonstrated good agreement between these techniques (Figure 9) [35]. These results suggest that x-ray diffraction is a practical method of measuring residual stresses in the laboratory. X-ray diffraction has also been used to measure the residual stresses on the surface of aluminum welds before and after UIT (Figure 12, above). This type of x-ray diffraction has also been developed into a commercial diffraction instrument with portable capabilities as proven by the successful use in a warehouse laboratory as well as onboard a Canadian naval vessel [60, 61].

When using x-ray diffraction, the elastic strain level in the surface of the sample is measured, and the stress is calculated based upon linear elasticity theory (represented in Figure 13). The spacing between planes of atoms in the crystalline lattice provides the fundamental length scale for these "atomic strain gauge" measurements. This "d-spacing", d_{hkl}, can be related to the x-ray diffraction angle through Bragg's law (Equation 2).

$$d_{\varphi\psi} = \frac{\lambda}{2\sin\theta} \qquad \text{Equation 2.}$$

Lambda (λ) is the wavelength of the incident x-ray (cobalt for this research) and theta (θ) is the Bragg diffraction angle. The lattice spacing, $d_{\phi\psi}$, is the measurement of the lattice spacing for a given {hkl} reflection at a given sample orientation (ϕ) and a given x-ray source orientation (ψ). The strain component perpendicular to the scattering vector, Q, is given by Equation 3.

$$(\varepsilon'_{33})_{\varphi\psi} = \frac{d_{\varphi\psi} - d_o}{d_o} \qquad \text{Equation 3.}$$

Where the unstrained lattice spacing (d_o) is determined from measurements taken normal to the material's surface. By measuring ε'_{33} for a series of ψ angles, the strain components ε_{ij} can be determined for a given sample orientation, ϕ, by solving the following system of equations:

$$\left(\varepsilon'_{33}\right)_{\phi\psi} = \frac{d_{\phi\psi} - d_0}{d_0} = \varepsilon_{11}\cos^2\phi\sin^2\psi + \varepsilon_{12}\sin 2\phi\sin^2\psi + \varepsilon_{22}\sin^2\phi\sin^2\psi$$
$$+ \varepsilon_{33}\cos^2\psi + \varepsilon_{13}\cos\phi\sin 2\psi + \varepsilon_{23}\sin\phi\sin 2\psi$$

Equation 4.

Typically, ε_{13} and ε_{23} are assumed to be close to zero, thus Equation 4 becomes:

$$\left(\varepsilon_{33}^{'}\right)_{\phi\psi} = \varepsilon_{11}\cos^2\phi\sin^2\psi + \varepsilon_{12}\sin 2\phi\sin^2\psi + \varepsilon_{22}\sin^2\phi\sin^2\psi + \varepsilon_{33}\cos^2\psi$$

Equation 5.

which is linear in $\sin^2\psi$. If one assumes isotropic elastic properties and that the stress normal to the sample surface, σ_{33}, is zero (assumed in XRD because x-rays do not penetrate more than a few microns [62]), then the measured strain can be related to the stress as:

$$\left(\varepsilon_{33}^{'}\right)_{\phi\psi} = \frac{1+\nu}{E}\left\{\sigma_{11}\cos^2\phi + \sigma_{12}\sin 2\phi + \sigma_{22}\sin^2\phi\right\}\sin^2\psi - \frac{\nu}{E}\left(\sigma_{11} + \sigma_{22}\right)$$

Equation 6.

At $\phi=0$, the level of stress is simply the linear slope of ε'_{33} plotted against $\sin^2\psi$. This behavior is termed "regular" $\sin^2$ behavior and is the basis for traditional laboratory x-ray residual stress measurements (Figure 14) [62]. The components of σ_{11}, σ_{22}, and σ_{12} can be measured independently by repeating this measurement for different values of the sample orientation, ϕ.

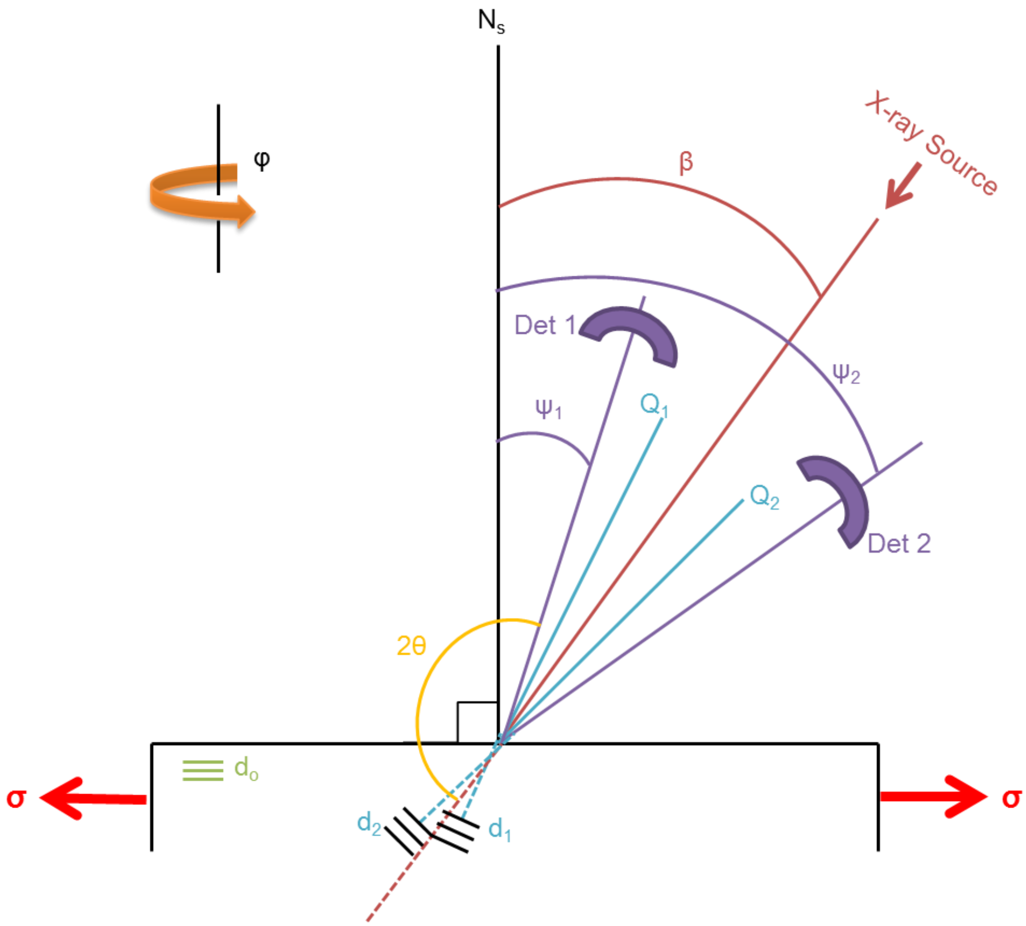

Figure 13. Visual depiction of measuring lattice planes of a specimen using x-ray diffraction. This method is used to determine residual stresses in a material.

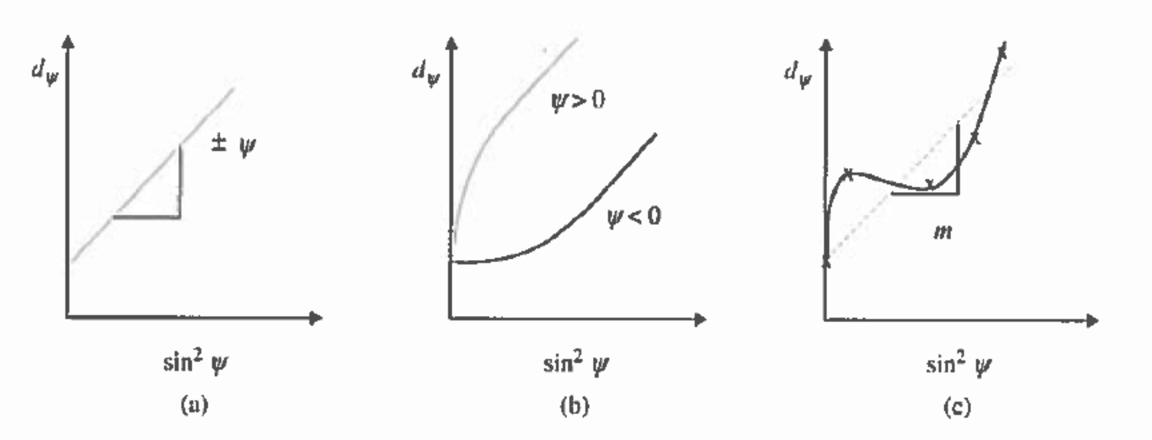

Figure 14. Regular (a,b) and irregular (c) d-spacing versus $\sin^2\psi$ results (from [62]). The branching in (b) is indicative of out of plain strains ε_{i3}.

C. THESIS OBJECTIVES

The purpose of this thesis is to investigate the residual stresses generated by ultrasonic impact treatment on welded AA5456 plate material, both in the laboratory and in the field. This information will lead to more effective means for resolving SCC issues plaguing USN cruisers (Figure 15). The laboratory experiments will provide a more comprehensive understanding of the processing-microstructure-property relationships. These field measurements are the first attempt to take this approach to analyzing aluminum structures on USN ships.

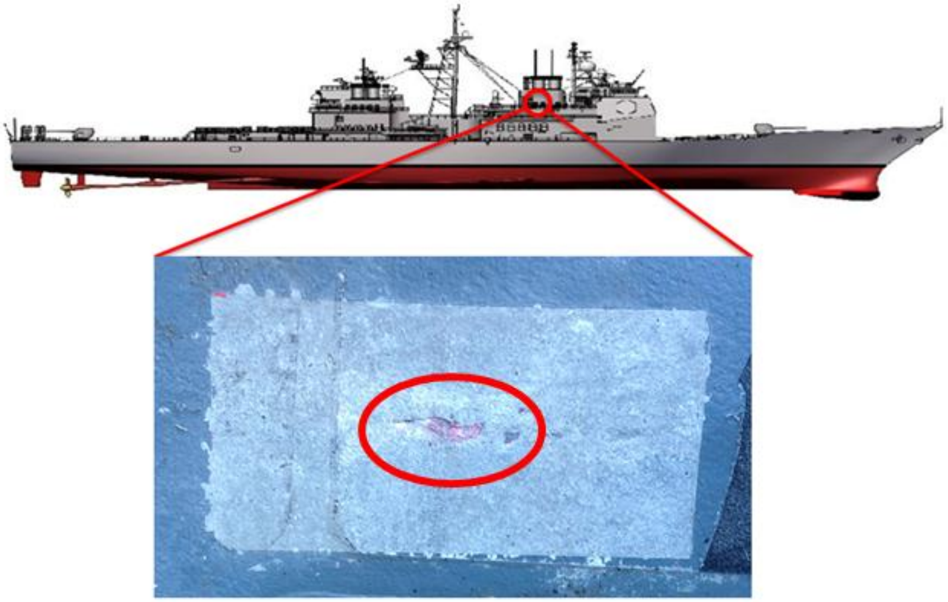

Figure 15. Existing stress corrosion crack on the O4 Level of a United States Navy cruiser.

The following objectives were established for research in this thesis:

- Successfully use x-ray diffraction to measure residual stresses on welded and ultrasonically treated aluminum plates.
- Explore the effects of UIT control parameters on the surface residual stresses generated in sensitized AA 5456 plate.
- Perform x-ray residual stress measurements on a U.S. Navy cruiser.
- Examine the effects of UIT on the weld microstructure.

THIS PAGE INTENTIONALLY LEFT BLANK

II. EXPERIMENTAL METHODS

Five sets of x-ray residual stress measurements were made on welded aluminum alloy 5456 plates, representing a variety of plate and welding conditions. One sample was a 32.43 mm (1.277 in) thick plate that was welded using gas tungsten arc welding (GTAW). Two sample sets were comprised of sensitized, shipboard material that was joined by gas metal arc welding (GMAW) and then subsequently subjected to ultrasonic impact treatment (UIT). The final sample was the aluminum deck of a U.S. Navy cruiser. Surface and depth-resolved residual stress measurements were taken using x-ray diffraction (XRD). Electrolytic polishing was conducted on various samples to determine the best solution and, ultimately, conduct the depth-resolved measurements.

A. LABORATORY EXPERIMENTS

1. Residual Stress Measurements

The Proto iXRD Residual Stress Analyzer was used to measure the residual stresses at various locations on each sample. This instrument is a dedicated x-ray diffractometer, specifically designed for residual stress measurements. The diffractometer remained in the manufacturer's radiation safety enclosure for the duration of all laboratory measurements. Startup was conducted in accordance with the standard and emergency operating procedures (SEOP) at the beginning of each day (or following any shut down period) [63]. Prior to collecting any data, the alignment of the equipment was verified using stress free and high stress aluminum standards.

Stress free powder standards and high stress standards were used to confirm alignment of the system. The 99.5 percent pure aluminum powder standard was secured in position on the test stand using putty and leveled using a simple bubble level. The iXRD collimator was adjusted in the ‘x’ and ‘y’ directions using the system motors (Figure 16). The manual focus or autofocus option was used to determine the required “z” position of the collimator and stored in the XRDWIN software. In order to conduct measurements, the pointer was removed and the 2 mm aperture was placed in the collimator.

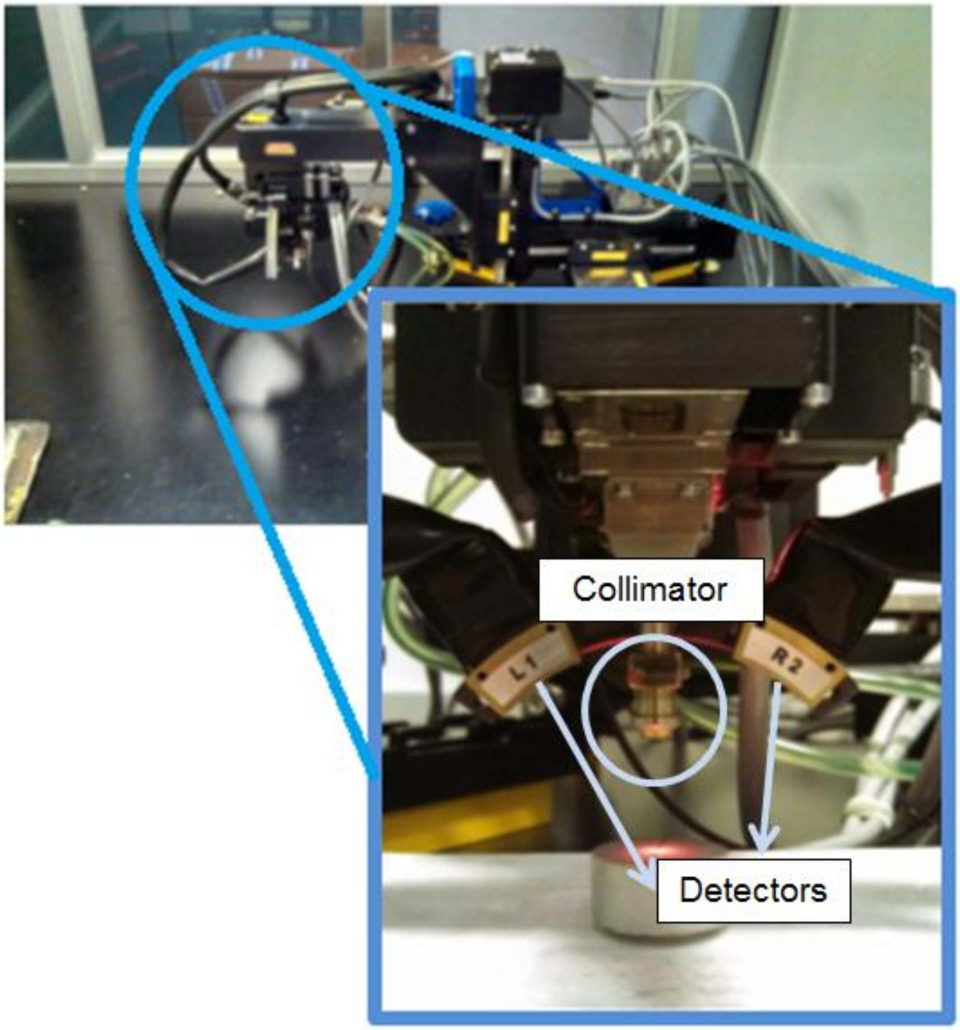

Figure 16. The Proto Manufacturing iXRD with close up of collimator used to collect residual stress values for AA5456 samples (after [64]). The high stress sample is pictured.

A single XRD profile of the aluminum powder standard was collected using the single exposure technique (SET). The beta and phi angles were set to zero (Figure 17). To ensure that the full range of the peak was visible and that there was room for peak broadening, the location of the diffraction peak on the detectors was reviewed on the representative graphs in the profile window. If the peaks were not centered, the detectors were moved to compensate for the shift in peaks and additional SET measurements were collected. The background fit and the region of interest (ROI) were adjusted to include only the region of the peak desired (Figure 18).

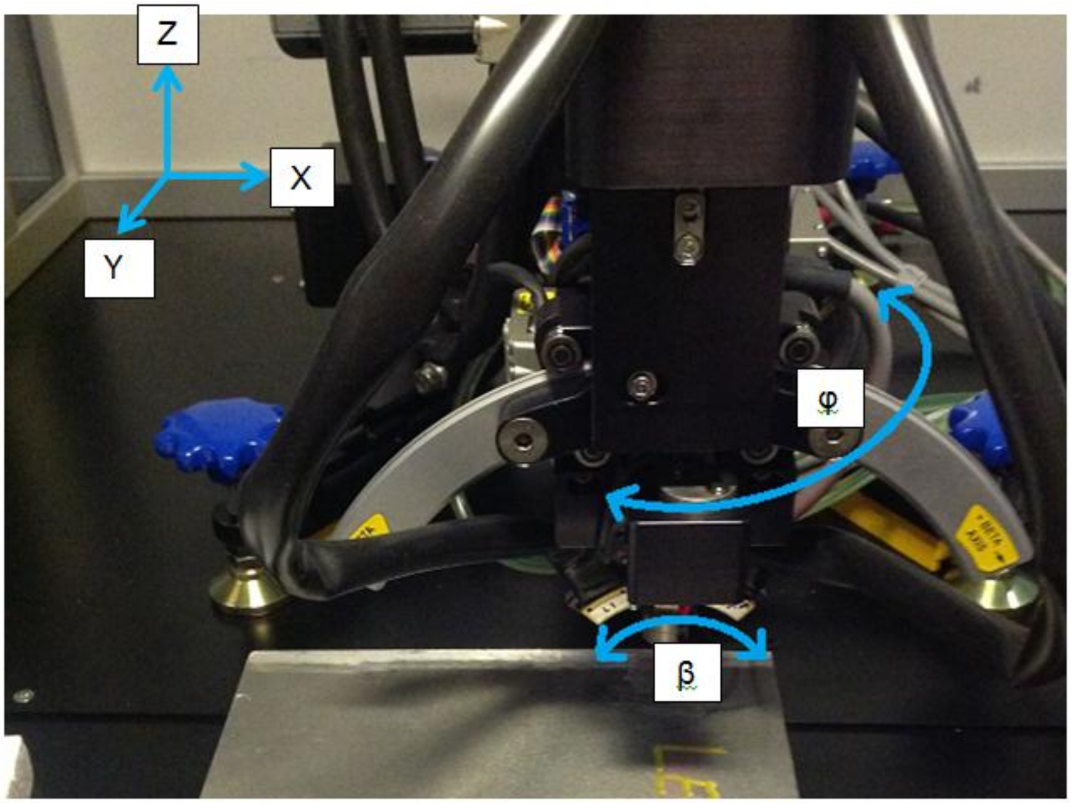

Figure 17. The Proto Manufacturing iXRD with each axis labeled. The X and Y axes had a range of ±50 mm from the zero position. The Z axis had a range of ±50 mm. The β axis had an arc from ±45°. The φ axis had a range of 0° to 180°.

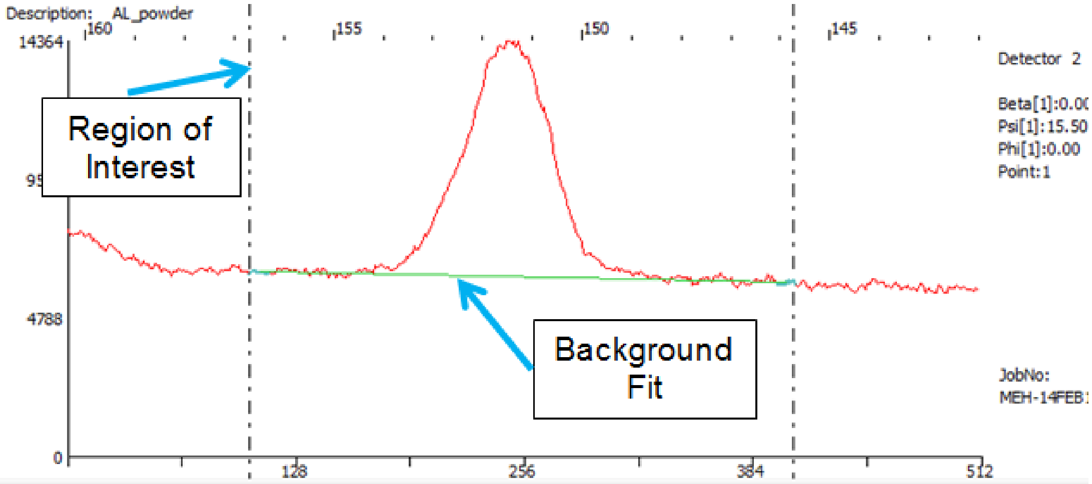

Figure 18. Results from a single exposure technique measurement of the aluminum powder standard. The region of interest is labeled and enclosed by the vertical dashed lines. The background fit is also labeled and depicted by the green horizontal line.

Gain measurements were made to provide a background signal level on the charge coupled device (CCD) detectors for the x-ray diffractometer. The gain established a baseline that was used for background subtraction during the diffraction peak analysis. A β-titanium gain shim was placed atop the aluminum powder standard to collect the gain. If the data returned was not well matched with the profile (Figure 19), the accelerating voltage on the x-ray was varied to achieve better agreement. The gain voltage value remained at 10 kilovolts for the majority of the measurements. The gain shim was removed to expose the powder standard and take additional measurements.

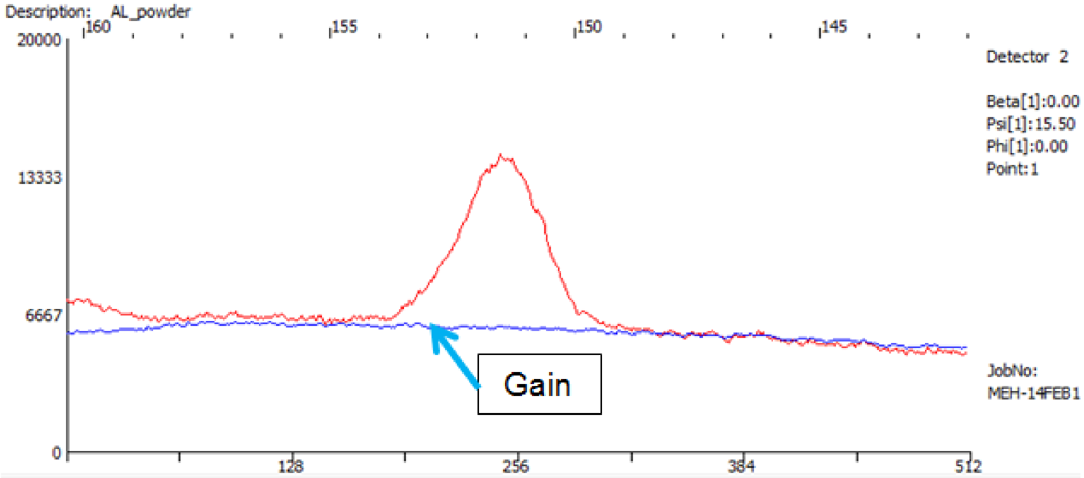

Figure 19. Profile of a single exposure technique measurement taken on the stress free aluminum powder standard. The blue horizontal line represents a well-matched gain. The red curve shows the diffraction signal from the aluminum, stress-free powder.

Three to five multiple exposure techniques (MET) were conducted to determine the stress in the powder standard. The phi angle was set to zero and eleven beta angles were examined, evenly spaced from 25 to -25 degrees. The results were analyzed by reviewing the bitmaps of the diffraction peaks at each beta angle for any inconsistencies (Figure 20). Measurement irregularities included no return on the data (e.g., all noise in the graph and no peak), jagged peaks, and lopsided peaks. These irregularities were a result of shadowing and were encountered more often during sample data collection vice standards measurements. The Background Fit and ROI were once again adjusted, but the settings had to be generic enough to include the diffraction peaks from each beta angle (visible when reviewing bitmaps). The d-spacing versus $\sin^2\psi$ plot was reviewed to verify low out-of-plane shear stress values were returned for the aluminum standards (Figure 21). A wide ellipse (ψ-splitting) indicated high out-of-plane shear strain values and, thus, a misalignment in the system when measuring the standards [62]. Out-of-plane shear stress values were compared to the baseline values returned during installation; a value that exceeded ±10 MPa was cause for concern.

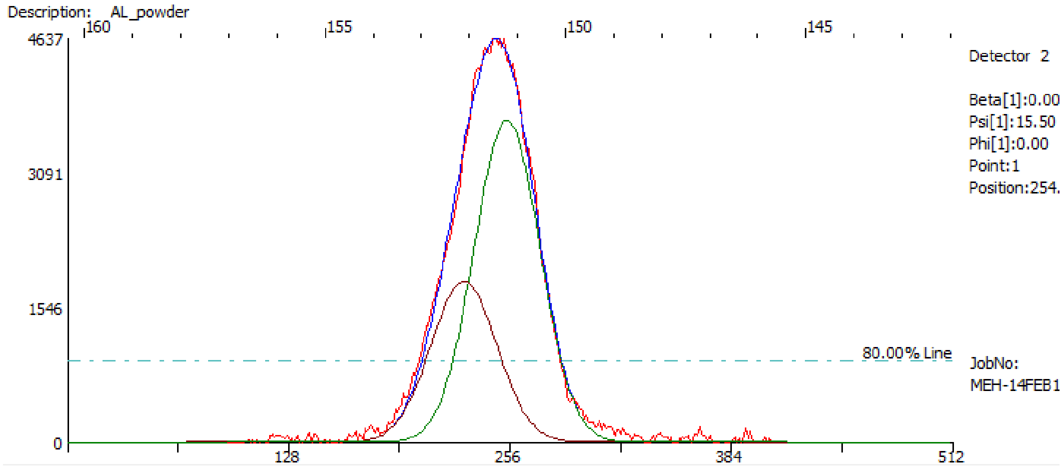

Figure 20. Measured diffraction peak from single exposure technique measurement of the stress free aluminum powder standard. This bitmap exhibits a smooth peak with very little noise (the red curve) and is an ideal representation of expected data return. A two-peak Gaussian method in conjunction with the linear psi fit correction was used to fit the peaks and determine peak location.

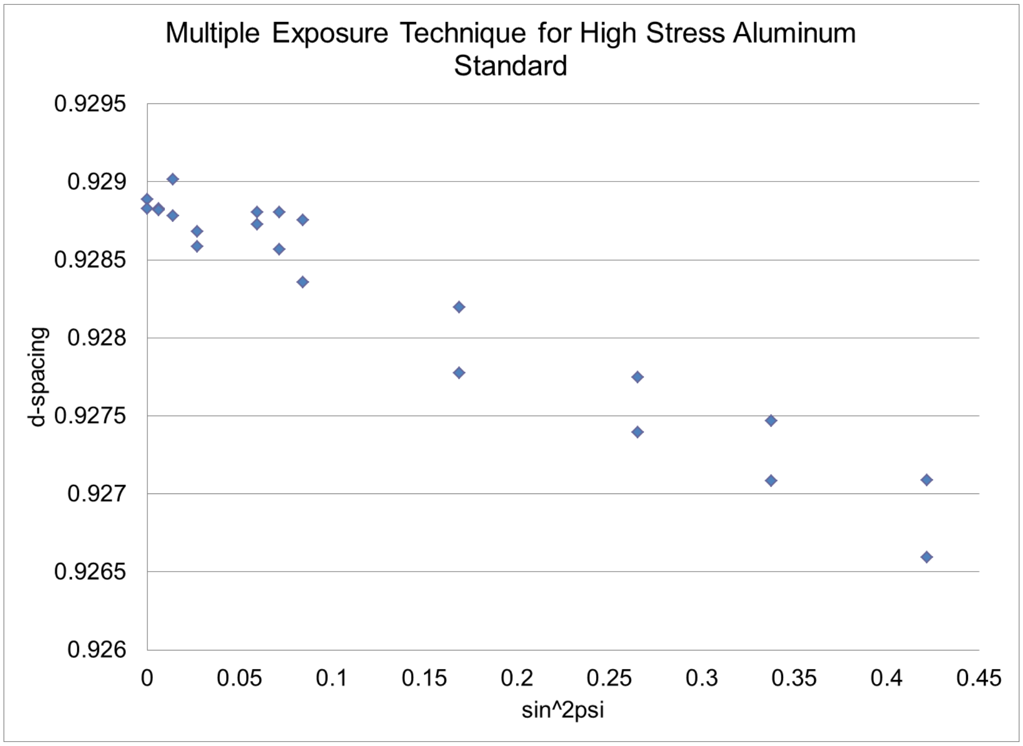

Figure 21. D-spacing versus $\sin^2\psi$ results from a multiple exposure technique measurement on the high stress aluminum standard. The slim ellipse was indicative of an acceptable out-of-plane shear and good system alignment.

If acceptable data was returned for the aluminum powder standards, one to three MET scans were conducted on the high stress aluminum standard. The collimator was defocused, the powder standard was replaced by the high stress standard, and the collimator was focused again. Measurements were taken and analyzed in the same manner discussed above. However, in some cases the stress and/or out-of-plane shear values initially achieved were outside the acceptable range for one or both standards (standards and acceptable values given in Table 4), and troubleshooting was required to realign the system. Alignments were verified in the following order: beta arc, manual and autofocus pointers, and tube placement. Realignments were conducted as necessary.

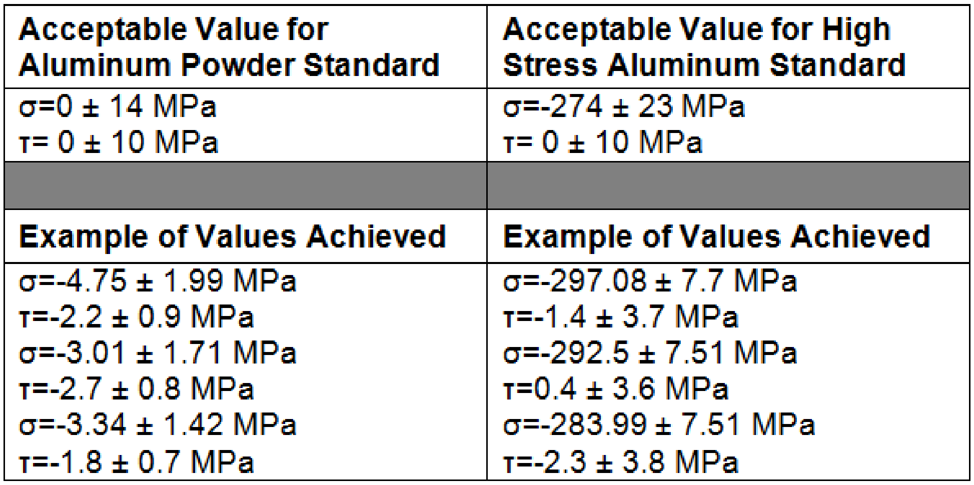

Acceptable Value for Aluminum Powder Standard	**Acceptable Value for High Stress Aluminum Standard**
σ=0 ± 14 MPa τ= 0 ± 10 MPa	σ=-274 ± 23 MPa τ= 0 ± 10 MPa
Example of Values Achieved	**Example of Values Achieved**
σ=-4.75 ± 1.99 MPa τ=-2.2 ± 0.9 MPa σ=-3.01 ± 1.71 MPa τ=-2.7 ± 0.8 MPa σ=-3.34 ± 1.42 MPa τ=-1.8 ± 0.7 MPa	σ=-297.08 ± 7.7 MPa τ=-1.4 ± 3.7 MPa σ=-292.5 ± 7.51 MPa τ=0.4 ± 3.6 MPa σ=-283.99 ± 7.51 MPa τ=-2.3 ± 3.8 MPa

Table 4. Acceptable values of stress measurements and stress measurements collected for aluminum powder and high stress standards.

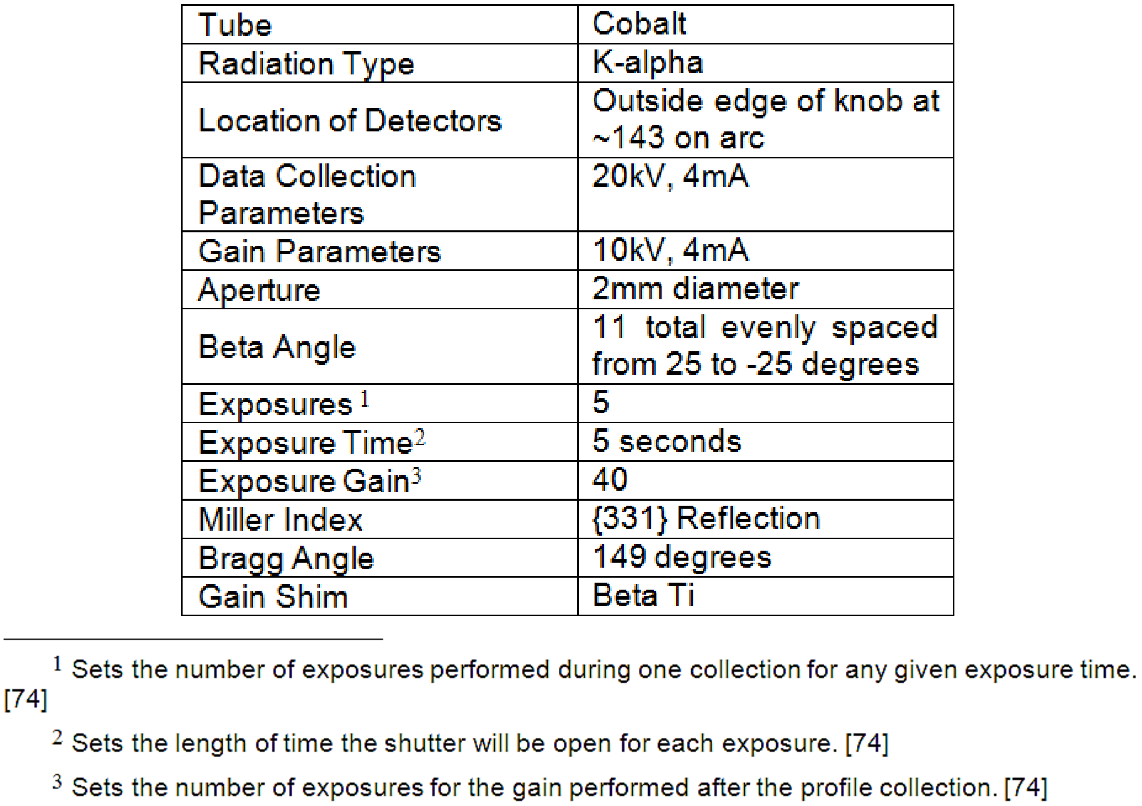

Tube	Cobalt
Radiation Type	K-alpha
Location of Detectors	Outside edge of knob at ~143 on arc
Data Collection Parameters	20kV, 4mA
Gain Parameters	10kV, 4mA
Aperture	2mm diameter
Beta Angle	11 total evenly spaced from 25 to -25 degrees
Exposures [1]	5
Exposure Time[2]	5 seconds
Exposure Gain[3]	40
Miller Index	{331} Reflection
Bragg Angle	149 degrees
Gain Shim	Beta Ti

---

[1] Sets the number of exposures performed during one collection for any given exposure time. [74]

[2] Sets the length of time the shutter will be open for each exposure. [74]

[3] Sets the number of exposures for the gain performed after the profile collection. [74]

Table 5. Proto iXRD parameters for laboratory based residual stress measurements on AA5456-H116.

For each of the measurements taken using the Proto iXRD, the surface of the material was located using the manual or automatic pointer. Biaxial MET and biaxial teach maps were the two primary types of measurements conducted (using parameters in Table 5). Single point MET measurements were mostly used for depth-resolved testing. The scans (conducted as discussed above for the standards) were completed after each set of electrolytic polishing (as outlined in the Electrolytic Polishing section). After each polish, the autofocus pointer was used to locate the newly exposed surface of the material. Teach maps were formed in the XRDWIN software for measurements taken across the various welds and UIT areas of AA5456. The user selected the line where the measurement was taken for each teach map. The number of points and the spacing of points were entered into the software. The spacing was larger in the base metal, but as the data points approached the estimated HAZ, the spacing was shortened to 2 mm (the aperture used was 2 mm, thus shorter distances would have been ineffective). The autofocus feature collected and stored the ‘Z’ value at each of the selected points. The pointer was removed and the scan was initiated. The iXRD automatically moved from point to point collecting biaxial measurements at each point.

2. Non-sensitized, Systematically Gas Tungsten Arc Welded

Sample set one was analyzed to confirm that the iXRD reliably measured the residual stresses across welds in AA5456 plate. Sample set one consisted of two 23.9 cm (9.41 in) wide, 21.7 cm (8.54 in) long, and 32.43 mm (1.277 in) thick plates of AA5456-H116 welded perpendicular to the rolling direction using four systematically different conditions of GTAW (Figure 22/Table 6). The plates were procured from Sunshine Metals. The chemical composition of AA5456 is: magnesium 5.07, manganese 0.64, iron 0.181, silicon 0.114, chromium 0.085, titanium 0.0231, zinc 0.017, copper 0.012 and the remainder aluminum. The compositions are given in weight percent and were certified by the American Bureau of Shipping. Members of the NPS machine shop fabricated the “bead-on-plate” welds with the gas tungsten arc welding (GTAW) process using the Miller Syncrowave 300 power supply. The plates were autogeneously welded and 100 percent argon gas was used for shielding.

The residual stresses on these plates were analyzed using the teach map feature discussed in the Residual Stress Measurements section. A teach map was developed across each of the welds at 5 mm increments in the base metal and 2 mm increments as the points approached the HAZ. The x-ray diffraction measurements were performed using the conditions listed in Table 5. The measurements were taken on the machined surfaces of the plates without any surface preparation.

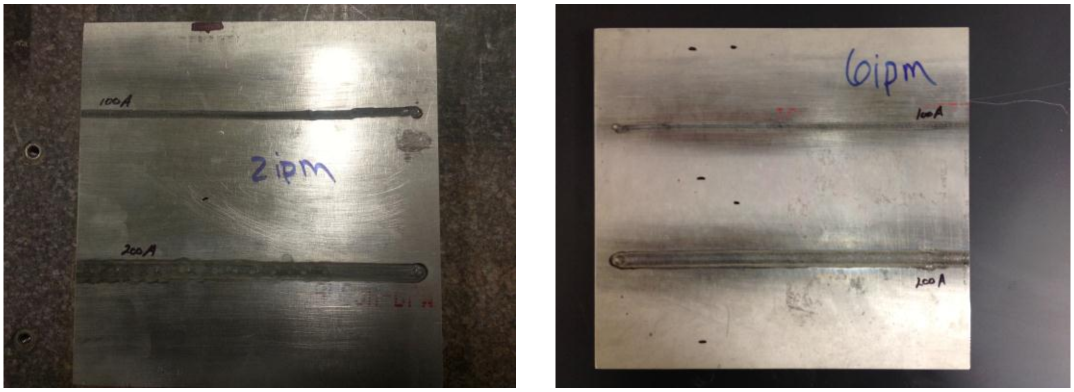

Figure 22. Optical macrographs of GTAW AA5456-H116 plate. The plate on the left was welded at a speed of 50.8 mm/min and the plate on the right was welded at 152 mm/min.

	Weld Speed, V (mm/min)	**Current, I (Amps)**	**Voltage, E (Volts)**	**Power, Q (Watts)**	**Heat Input, H (kJ/mm)**
Weld 1	50.8	100	15.4	1540	1.819
Weld 2	50.8	200	16.8	3360	3.969
Weld 3	152.4	100	15.4	1540	0.606
Weld 4	152.4	200	16.8	3360	1.323
Base Metal	AA5456				
Filler Wire	N/A (autogenous weld)				
Shielding Gas	Argon				

Table 6. GTAW parameters for non-sensitized AA5456-H116 plate

Where power, Q, was determined using Equation 7 and heat input, H, was determined using Equation 8 (scaling values used for conversion factor), respectively:

$$Q = I \cdot E \qquad \text{Equation 7.}$$

$$H = \frac{60 * Q}{1000 * V} \qquad \text{Equation 8.}$$

3. Sensitized, Systematically Ultrasonic Impact Treated, Gas Metal Arc Welded

Sample set two consisted of two 37 cm (14.6 in) wide, 36 cm (14.2 in) long, and 6.35 mm (0.25 in) plates composed of sensitized AA5456 plate material cut from a U.S. Navy cruiser (Figure 23). The material was obtained from the O4 level. Random ASTM G67 testing for degree of sensitization (DOS) of material from the O4 level of a U.S. Navy cruiser indicate DOS levels that range from 40 to >60 mg/cm^2. The plates were butted together to form a 60 degree single-v groove joint. The welds were fabricated with 5556 filler metal by the GMAW pulse process at the Naval Surface Warfare Center Carderock Division (NSWCCD). Welding parameters are provided in Table 7.

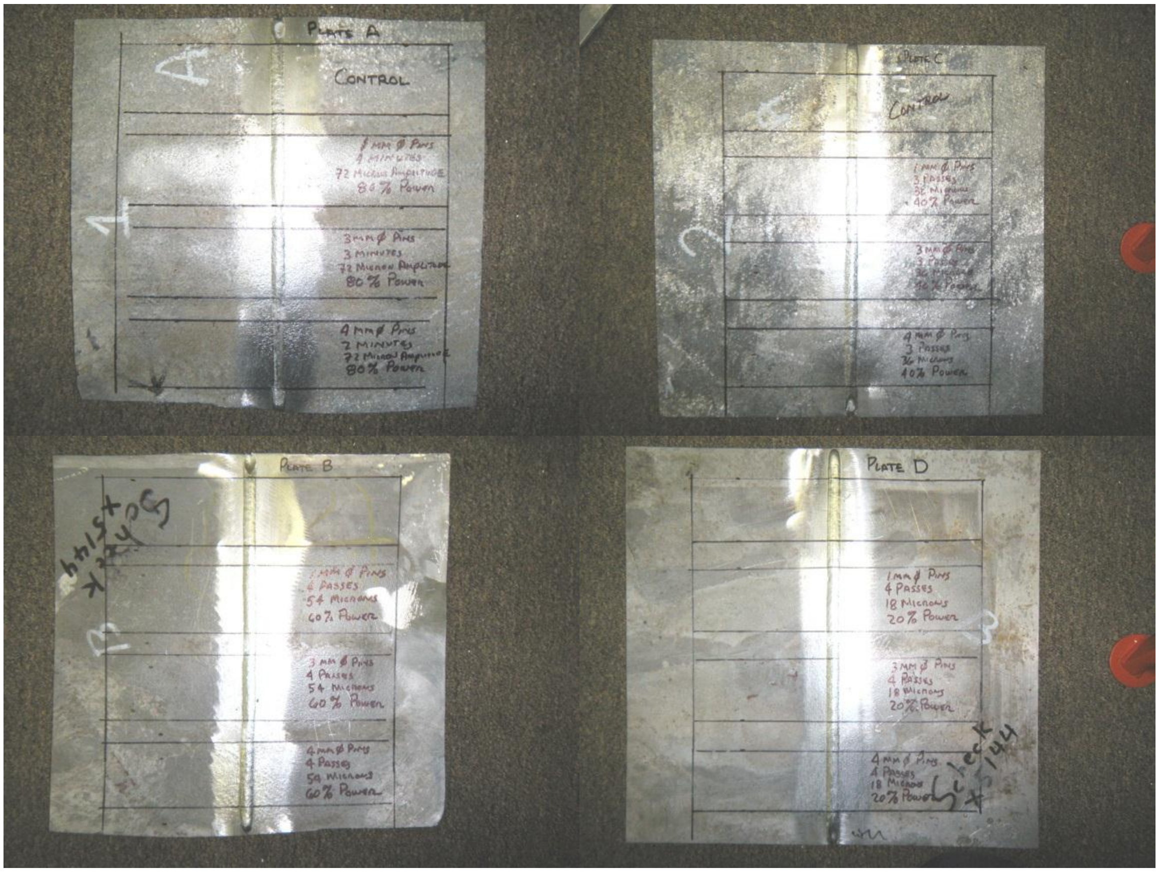

Figure 23. Two plates of sensitized, GMAW butt welded AA5456-H116 at various UIT conditions. Clockwise from top left: Surface A, Surface C, Surface D, and Surface B. Parameters given in Table 8.

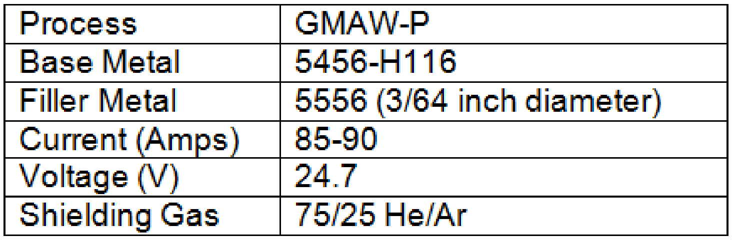

Process	GMAW-P
Base Metal	5456-H116
Filler Metal	5556 (3/64 inch diameter)
Current (Amps)	85-90
Voltage (V)	24.7
Shielding Gas	75/25 He/Ar

Table 7. GMAW parameters for sensitized AA5456-H116 plates.

UIT was performed commercially by Empowering Technologies a subsidiary of SONATS. UIT was conducted at different power inputs on each surface and each surface had four experimental “zones” as noted below (Table 8). At 100 percent power, the operating frequency was 20 kHz resulting in 64 µm amplitude. Three zones were treated with hardened tool steel pins with different diameters.

- Control Zone (no UIT conducted)
- UIT conducted with 1 mm pins
- UIT conducted with 3 mm pins
- UIT conducted with 4 mm pins.

The zones were 27.5 cm (10.8 in) wide, 6.5 cm (2.6 in) long and separated by a 2 cm (0.79 in) gap. Both of the plates exhibited some warping, which is a common characteristic of deck material obtained from USN cruisers.

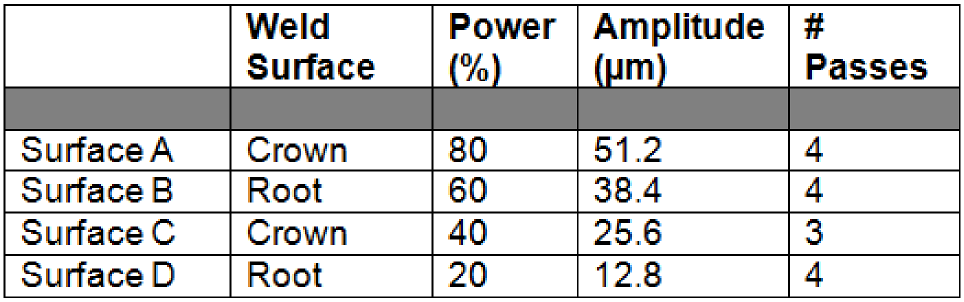

	Weld Surface	Power (%)	Amplitude (µm)	# Passes
Surface A	Crown	80	51.2	4
Surface B	Root	60	38.4	4
Surface C	Crown	40	25.6	3
Surface D	Root	20	12.8	4

Table 8. Ultrasonic impact treatment parameters conducted on sensitized AA5456-H116 plates performed by SONATS.

Sample two provided a systematic set of residual stresses on sensitized, GMAW butt welded AA5456-H116 plates. Teach maps were recorded across each zone on all four surfaces as discussed in the Residual Stress Measurements section. No further surface preparation was conducted prior to measurement. On Surface A (80 percent power) in the 3 mm pin zone, repeatability experiments were conducted by taking multiple teach maps across the same area. Depth-resolved measurements were taken on Surface A (control, 1 mm, and 4 mm pin sizes) and Surface C (40 percent power, 4 mm pin size) at a position in or near the HAZ and a position in the base metal. The areas were electropolished using the "L1" solution as discussed in the Electrolytic Polishing section below. Following each layer removal with electropolishing, depth was determined and an MET measurement was taken (as discussed in the Residual Stress Measurements section above) at each location.

4. Non-sensitized, Various Ultrasonic Impact Treated Areas, Gas Metal Arc Welded

Sample three consisted of two specimen of 9.525 mm (0.375 in) thick, as-manufactured AA5456-H116 butt welded together parallel to the rolling direction of the material (Figure 24). Dr. Tran provided sample three, which was welded at NSWCCD using GMAW (welding parameters provided in Table 9). UIT was conducted at the toe of the weld on both sides. A patch of UIT was also conducted in the upper left corner of the plate. The UIT was conducted using a 3 mm diameter pin at a frequency of 20 kHz.

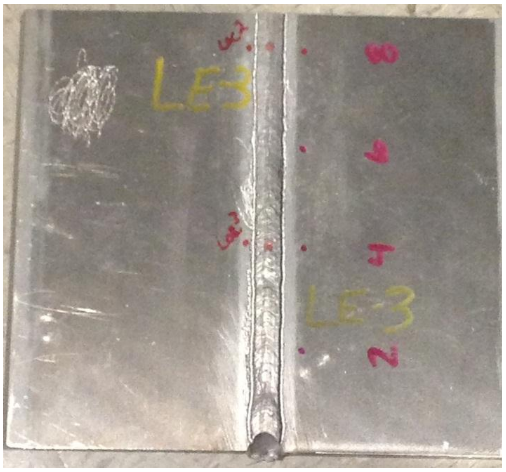

Figure 24. Two plates of non-sensitized, GMAW butt welded AA5456-H116. UIT is present at the toe of the weld and in a patch near the top left corner.

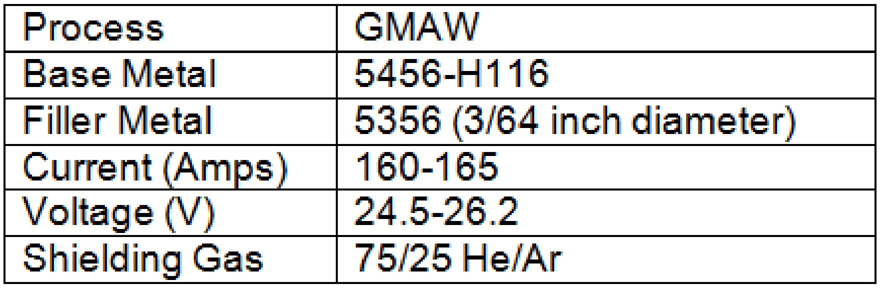

Process	GMAW
Base Metal	5456-H116
Filler Metal	5356 (3/64 inch diameter)
Current (Amps)	160-165
Voltage (V)	24.5-26.2
Shielding Gas	75/25 He/Ar

Table 9. GMAW parameters for non-sensitized AA5456-H116.

Due to the non-systematic nature of sample three, it was used largely for comparison of residual stresses on non-sensitized AA5456-H116 with and without UIT. Residual stress measurements were taken via a teach map across the weld as well as three METs at individual locations including: base metal, the UIT patch, and the UIT line along the toe of the weld. No surface preparation was conducted and data was collected using methods in the Residual Stress Measurements section. Electropolish tests were conducted using various parameters as discussed in the Electrolytic Polishing section (below) to determine the best solution, time, and frequency parameters. A depth resolve measurement was attempted on the UIT patch using a solution of equal parts perchloric acid and Electrolyte ‘A’.

5. Sensitized, Ultrasonic Impact Treated, Gas Metal Arc Welded

Sample four was a single specimen of 19.5 cm (7.68 in) wide, 41 cm (16.1 in) long, and 6.35 mm (0.25 in) thick plate cut directly from the superstructure of a U.S. Navy cruiser (Figure 25). This sample provided by Dr. Tran had a GMAW butt weld parallel to the rolling direction and along the edge of the plate. The weld was fabricated during original ship construction; therefore, the welding parameters are unknown. UIT was conducted on the base metal and at the root of the weld subsequent to removal from a U.S. Navy cruiser. Empowering Technologies completed both treatments. The base metal UIT was performed with a multi-pin (3 mm diameter each) tool at a frequency of 20 kHz. The UIT at the root of the weld was conducted using a single 3 mm diameter pin tool at a frequency of 20 kHz. The degree of sensitization for these samples ranged from 40 to >60 mg/cm^2.

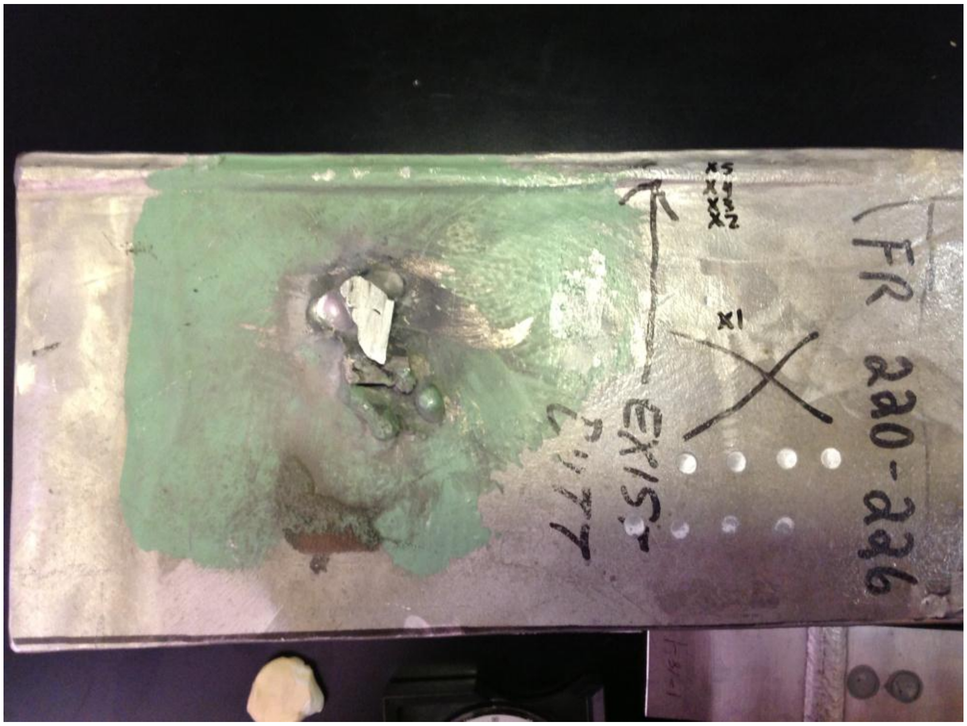

Figure 25. Sensitized AA5456-H116 removed from superstructure of USN cruiser.

Because sample four did not offer a systematic set of data, residual stresses were measured to determine variances that occur due to UIT as well as the condition of material following time in service. Two teach maps were collected on the surface of the material: one across the root of the weld and one from the crown of the weld into the base metal. No surface preparation was conducted and data was collected using the methods described above in the Residual Stress Measurements section. Electropolishing tests were conducted on sample four using only ‘Electrolyte A’ to determine the best time and frequency parameters, as discussed in the Electrolytic Polishing section. Depth was determined and quality of polish was assessed for each instance of electropolishing.

6. Electrolytic Polishing

The Proto Electrolytic Polisher Model 8818-V3 (Figure 26) was used to systematically remove material from the surface of the samples in order to produce depth-resolved residual stress measurements. Solution, polish time, and voltage were determined based on a series of experiments conducted on sample three and sample four. Solutions were mixed before being placed in the center chamber of the stainless steel electrolytic tank. The ‘L1’ solution was placed in the freezer prior to use and in between every couple uses to decrease the temperature and maintain viscosity. Other solutions were used at room temperature.

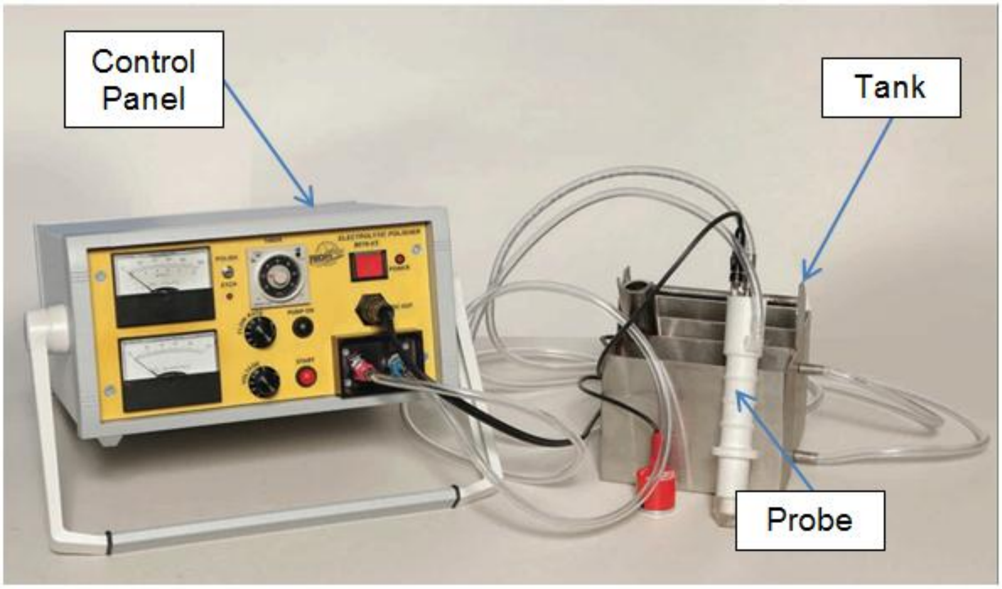

Figure 26. Proto Electrolytic Polisher Model 8818-V3 used to remove surface material for depth resolve measurements. (image adapted from [65])

A circuit and chemical reaction were required to conduct electrolytic polishing. The 15 mm rubber tip was selected for the probe and pressed against the surface of the material, supplying the electrolyte. The black banana plug was placed into the probe (cathode) and the red banana plug was placed into a large alligator clip, which was clamped to the edge of the selected sample (anode). When the power supply was turned on, current was passed through the electrolyte from the anode to the cathode. The electrolyte reacted with the sample to remove material. The voltage and time were selected on the electrolytic polisher main control panel.

Throughout the duration of tests conducted, the spots were closely scrutinized for pitting, quality of polish, and depth attained. Residual stress measurements were taken to compare the polishes from a solution of only ‘Electrolyte A’ and a solution of equal parts ‘Electrolyte A’ and perchloric acid. Depths were measured as needed using the iXRD autofocus pointer. Polishing times varied greatly for the tests for the sake of achieving desired depth. Table 10 organizes the parameters tested.

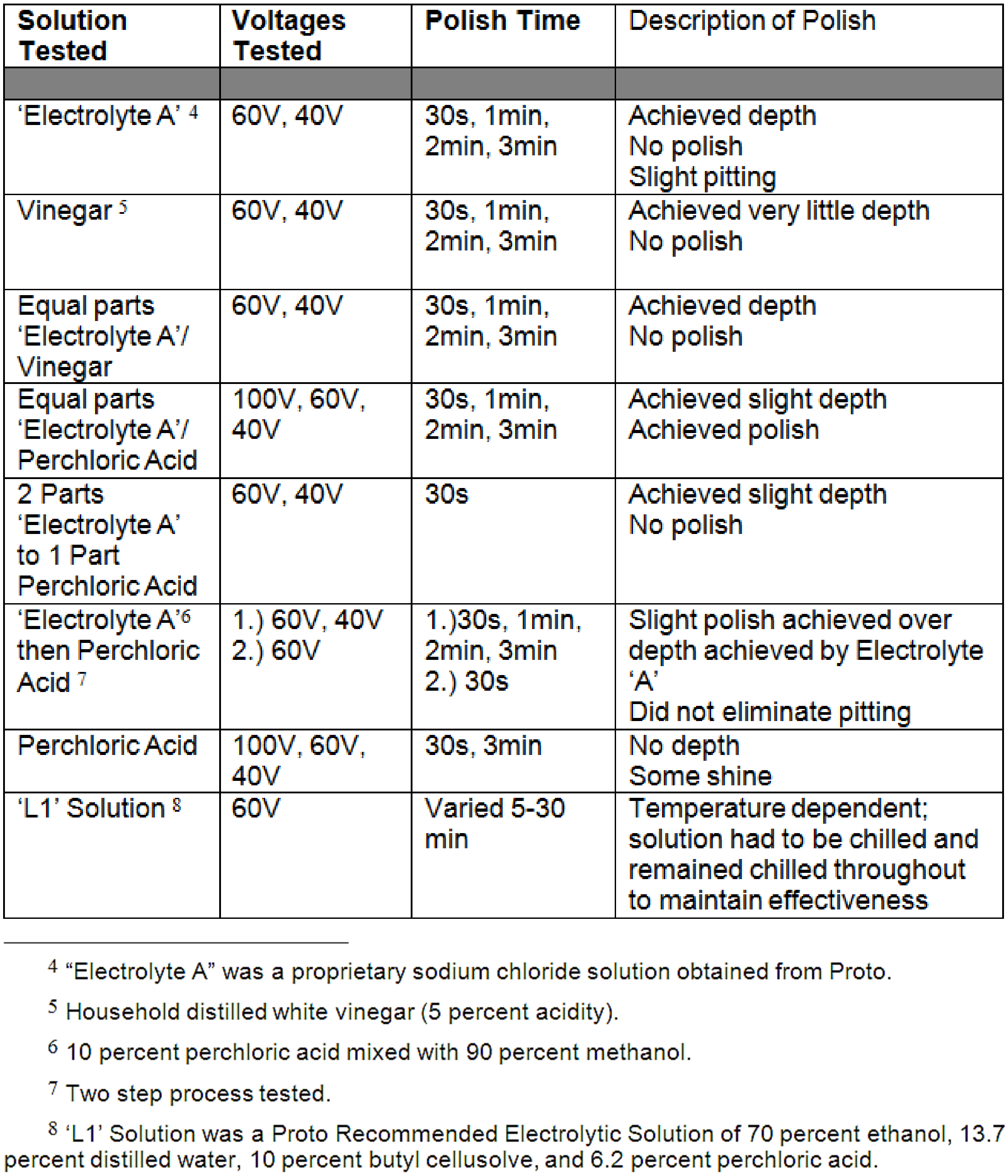

Solution Tested	**Voltages Tested**	**Polish Time**	Description of Polish
‘Electrolyte A’ [4]	60V, 40V	30s, 1min, 2min, 3min	Achieved depth No polish Slight pitting
Vinegar [5]	60V, 40V	30s, 1min, 2min, 3min	Achieved very little depth No polish
Equal parts ‘Electrolyte A’/ Vinegar	60V, 40V	30s, 1min, 2min, 3min	Achieved depth No polish
Equal parts ‘Electrolyte A’/ Perchloric Acid	100V, 60V, 40V	30s, 1min, 2min, 3min	Achieved slight depth Achieved polish
2 Parts ‘Electrolyte A’ to 1 Part Perchloric Acid	60V, 40V	30s	Achieved slight depth No polish
‘Electrolyte A’[6] then Perchloric Acid [7]	1.) 60V, 40V 2.) 60V	1.)30s, 1min, 2min, 3min 2.) 30s	Slight polish achieved over depth achieved by Electrolyte ‘A’ Did not eliminate pitting
Perchloric Acid	100V, 60V, 40V	30s, 3min	No depth Some shine
‘L1’ Solution [8]	60V	Varied 5-30 min	Temperature dependent; solution had to be chilled and remained chilled throughout to maintain effectiveness

---

[4] “Electrolyte A” was a proprietary sodium chloride solution obtained from Proto.

[5] Household distilled white vinegar (5 percent acidity).

[6] 10 percent perchloric acid mixed with 90 percent methanol.

[7] Two step process tested.

[8] ‘L1’ Solution was a Proto Recommended Electrolytic Solution of 70 percent ethanol, 13.7 percent distilled water, 10 percent butyl cellusolve, and 6.2 percent perchloric acid.

Table 10. Solutions, voltages and times tested for electrolytic polishing with a description of the polish achieved.

7. Microstructural Analysis

Electron microscopy was used to examine the microstructure of the aluminum after UIT. Two cross-sectional samples were cut transverse to the weld from sample set two: one sample from the control zone of surface A and one sample from the 1 mm pin zone of Surface A (80 percent power). These samples were cut transversely and metallographically polished such that the polished surface was a cross section across the weld allowing examination of the microstructure as a function of depth from the UIT surface. Metallographic polishing was performed using silicon carbide grit papers to a 4,000 grit and diamond polishing down to a one micron finish, followed by 0.05 μm colloidal silica. After metallography, the samples were electropolished using the Buehler Electromet 4 Electrolytic Polishing system designed for SEM samples. The electropolishing was accomplished using a 10 percent percholric-90 percent ethanol solution maintained at about -40°C, using liquid nitrogen, with an applied voltage of 20 volts. A 25 mm circular mask was used during electropolishing. These conditions resulted in a current between 0.1-0.2 amperes. Each sample was polished with one or two (as needed), 30 second exposures.

After electropolishing, the microstructure was examined using SEM with a Zeiss Neon 40 focused ion beam, scanning electron microscope (FIB-SEM). Imaging and electron backscatter diffraction (EBSD) were performed at 20 keV with a 60 μm objective aperture in high current mode. Both backscatter and secondary electron images were recorded. The EBSD data was collected using the EDAX OIM 6 system with a Hikari camera.

B. FIELD BASED EXPERIMENTS

1. Field Based Residual Stress Measurements

Authorization to conduct field based residual stress measurements involved extensive team training and preparation, visiting a decommissioned U.S. Navy cruiser, and shipboard measurements on an active U.S. Navy cruiser. Preparation initiated with team training and practice as soon as the iXRD arrived. Logistics discussions and walkthroughs were conducted on a decommissioned U.S. Navy cruiser during a trip to the Navy Yard in Philadelphia, Pennsylvania. An open beam standard and emergency operating procedure (SEOP) was developed in accordance with the U.S. Navy radiation safety requirements (set forth [66]) and NPS policies. All team members attained radiation worker qualifications and one member attained his radiation safety officer qualification. With final approval of the SEOP, an open beam field experiment was conducted at NPS to practice the process. Paint removal and surface preparation methods were also developed and tested prior to a shipboard visit. Initial shipboard field measurements occurred on site in San Diego, California with a team consisting of one student, one professor, and the NPS radiation safety officer.

The iXRD had to be assembled and disassembled daily due to environmental exposure and storage limitations. The setup location each day depended on the testing area (position one or position two). The iXRD field based setup (Figure 27) and start-up were conducted in accordance with the open beam SEOP and the Proto iXRD manual. To prepare the space, the sample area was polished to a mirror finish as discussed below. For safety considerations [66, 67]:

- The thickness of the deck was confirmed using an ultrasonic transducer and compared to the plot in Figure 28. To verify safety of personnel passing beneath the work area. A minimum thickness of 2 mm (0.079 in) was required. The standard deck thickness in these field measurements was 6.35 mm (0.25 in).
- The area was posted for radiation at the required 1 meter radius in all directions to achieve an x-ray exposure rate of <2 mrem/hr as shown in Figure 29.
- A radiation survey was conducted.
- All team members were required to wear personal dosimetry.

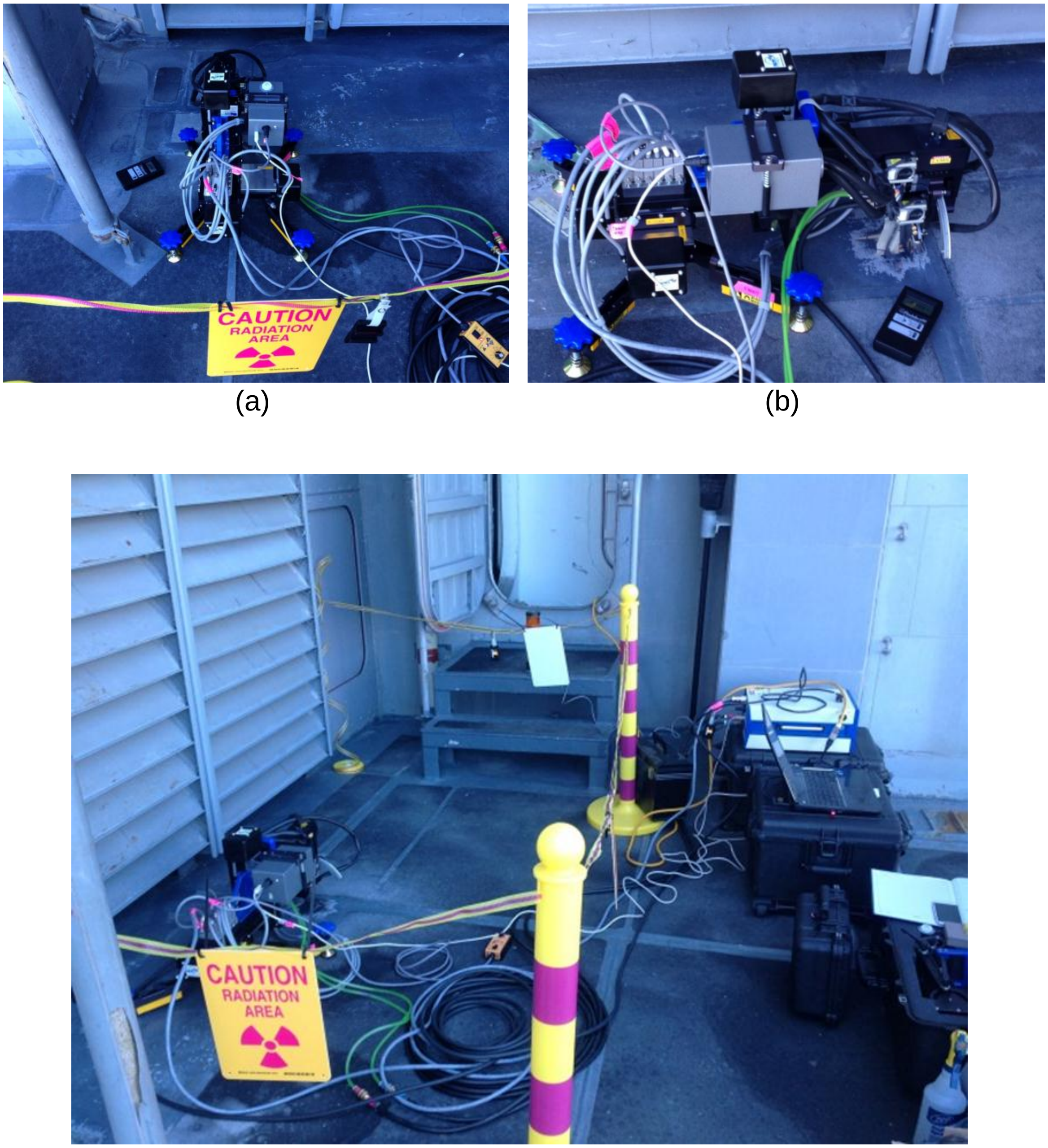

(a) (b)

(c)

Figure 27. Shipboard field setup of Proto iXRD and radiation safety equipment. Image (a) is the field configuration for position one. Image (b) is the field configuration for position two. Image (c) shows a broader view of the work area.

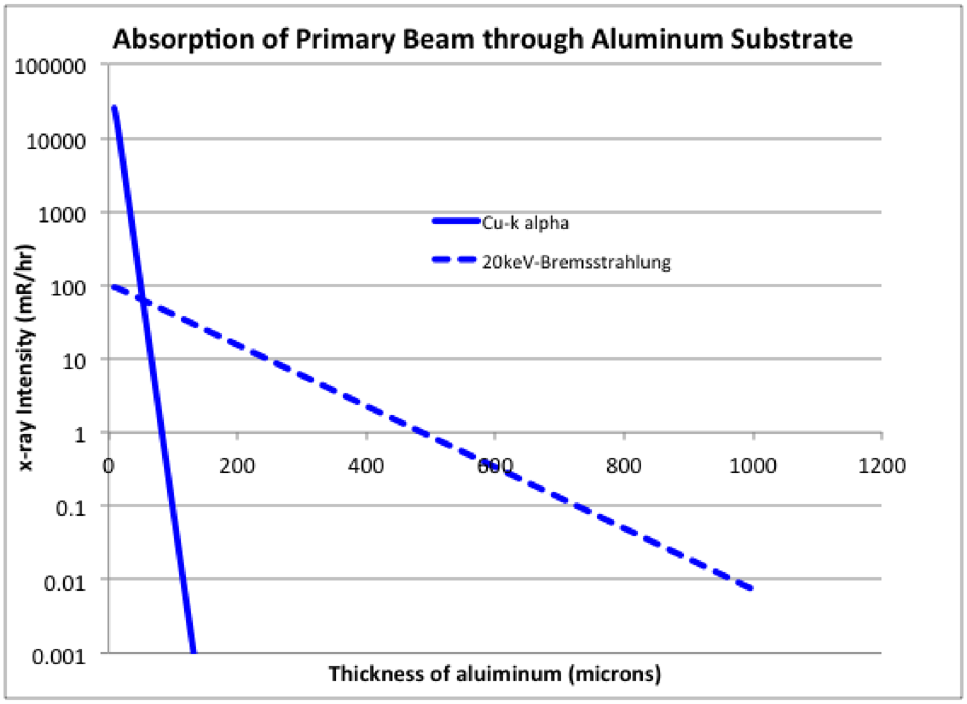

Figure 28. Absorption of the primary beam through aluminum substrate for the Proto iXRD (from [67]).

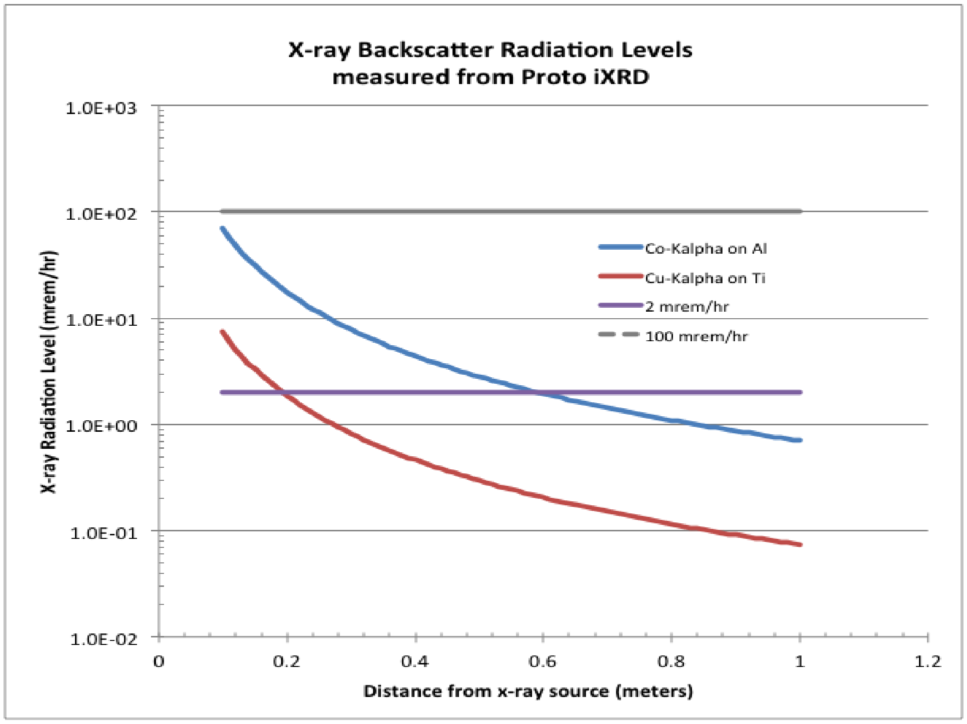

Figure 29. Backscattered x-ray intensity levels determined by experimental measurements of the Proto iXRD (from [67]).

Field based residual stress measurements were conducted following the completion of the SEOP. The system alignment was verified using the aluminum powder and high stress standards in the same manner as discussed in the laboratory Residual Stress Measurements section. However, prior to entering the posted area, a scan using the IM-231A ionization chamber RADIAC was required to determine if the area was safe to enter. The Proto Residual Stress Analyzer hardware manual was used for any required system realignments. The software parameters were similar to the laboratory parameters (Table 11). For some of the measurements, the beta angles had to be adjusted for the safety of the equipment and personnel due to the warped deck (discussed below).

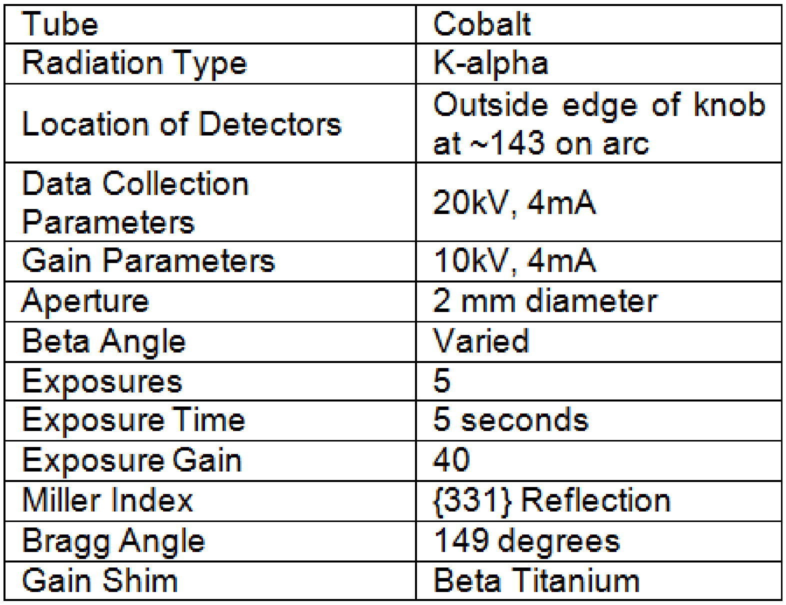

Tube	Cobalt
Radiation Type	K-alpha
Location of Detectors	Outside edge of knob at ~143 on arc
Data Collection Parameters	20kV, 4mA
Gain Parameters	10kV, 4mA
Aperture	2 mm diameter
Beta Angle	Varied
Exposures	5
Exposure Time	5 seconds
Exposure Gain	40
Miller Index	{331} Reflection
Bragg Angle	149 degrees
Gain Shim	Beta Titanium

Table 11. Proto iXRD parameters for field based residual stress measurements on shipboard AA5456-H116.

2. Shipboard, Sensitized, Gas Metal Arc Welded Aluminum Alloy 5456

X-ray residual stress measurements were performed at two locations onboard an active U.S. Navy cruiser. The analysis location was selected on the fourth deck high of the ship (O4 level). More specifically it was on the forward portion of the ship, starboard side, directly beside the rear corner and midpoint of the air intake. This area included an existing, patched crack near a GMAW weld. The area from the weld to the crack was used as sample position one an area near a separate weld was used as sample position two (Figure 30). An Olympus Ultrasonic Thickness Gage measured the deck thickness to be 6.35 mm (0.25 in). The deck was noticeably warped. Nonskid tape was recently replaced throughout the O4 level in accordance with shipboard safety requirements; however the sample area was cleared of nonskid tape for these measurements. The maintenance process performed on the sample area and welding parameters of the existing shipboard weld are unknown. There was no UIT in the sample area.

Figure 30. Shipboard sample location for residual stress measurements of field AA5456-H116. Sample position one is on the left (located at the rear corner of the air handler) and sample position two is on the right (located roughly at the midpoint of the air handler).

For these measurements, surface preparation was required due to the primer, paint, and nonskid residue remaining on the deck. Electropolishing was not cleared for use on board the ship, so a metallographic polishing method was used to prepare the surface. Low grit sandpaper (60, 120, and 220 grit) was used on a household 5 inch random orbit sander to remove the surface paint and primer. This surface was then hand sanded using 400 grit and 600 grit sandpaper consecutively. Microfiber bonnets and aluminum oxide (Al_2O_3) slurry (5 µm and 3 µm) were used with a household 6 inch orbital buffer to polish the surface.

One attempt was made to use the new *in situ* metallography procedure developed by Dr. W. J. Golumbfskie at NSWCCD [68]. This process uses a portable, high-speed rotary tool with a series of silicon carbide (SiC) abrasive discs and diamond impregnated polishing cloths. The following steps were used for this procedure:

- 120 grit SiC for ~2 minutes at speed setting #5 (repeat until surface is smooth)
- 240 grit SiC for ~75 seconds at speed setting #5
- 320 grit SiC for ~75 seconds at speed setting #4
- 600 grit SiC for ~75 seconds at speed setting #4
- 1000 grit SiC for ~75 seconds at speed setting #4
- 6 µm diamond on Struers MOL cloth for 2.5 minutes at speed setting #5
- 1 µm diamond on Buehler Microcloth (or Struers NAP cloth) for 2.5 minutes at speed setting #4
- 0.3 µm alumna slurry on Buehler Microcloth (or Struers NAP cloth) for 2.5 minutes at speed setting #4

After completing this procedure, the quality of the surface polish was inspected by a portable optical microscope. The quality of the surface polish was reasonably good for optical microscopy and was better than the primary process described above.

Residual stress measurements were taken at position one and position two as discussed in the previous section using teach maps. At position one a teach map consisting of four points was collected starting at the crown of the weld and working towards the existing crack. The following three points were at positions 15 mm, 30 mm, and 50 mm from the initial point. Nine beta angles were used for this measurement due to the geometry of the deck. The angles were spaced evenly from 20.01 to -20.01 degrees. All other software parameters were identical to Table 11. A three point teach map starting at the crown of the weld was developed for position two. Point two was 18.5 mm from the crown of the weld and point three was 60.34 mm from the weld crown. These points were expected to be in the HAZ and base metal, respectively. Eleven beta angles were used for this measurement and were evenly spaced from 25 to -25 degrees.

III. RESULTS

D-spacing versus $\sin^2\psi$ plots demonstrated the data upon which all of the measurements are based (Figure 31 and Figure 32). Data collected from the two standard aluminum specimens was used on a regular basis to verify the alignment of the system. A nearly horizontal line with little to no sign of an ellipse is expected and observed for the stress free powder aluminum standard. A slope to this line, or significant splitting between the red and green points, would indicate system misalignment. More specifically, splitting or branching in the d-spacing versus $\sin^2\psi$ plot is caused by an out-of-plane shear strain. The data in Figure 30 is typical for a well-aligned system. The high stress standard contains a relatively large level of compressive stress (-274 ± 23 MPa); therefore the d-spacing versus $\sin^2\psi$ plots should exhibit negligible splitting and a negative slope. Excessive branching in this plot is also indicative of a system misalignment. The data in Figure 31 is typical for a well-aligned system.

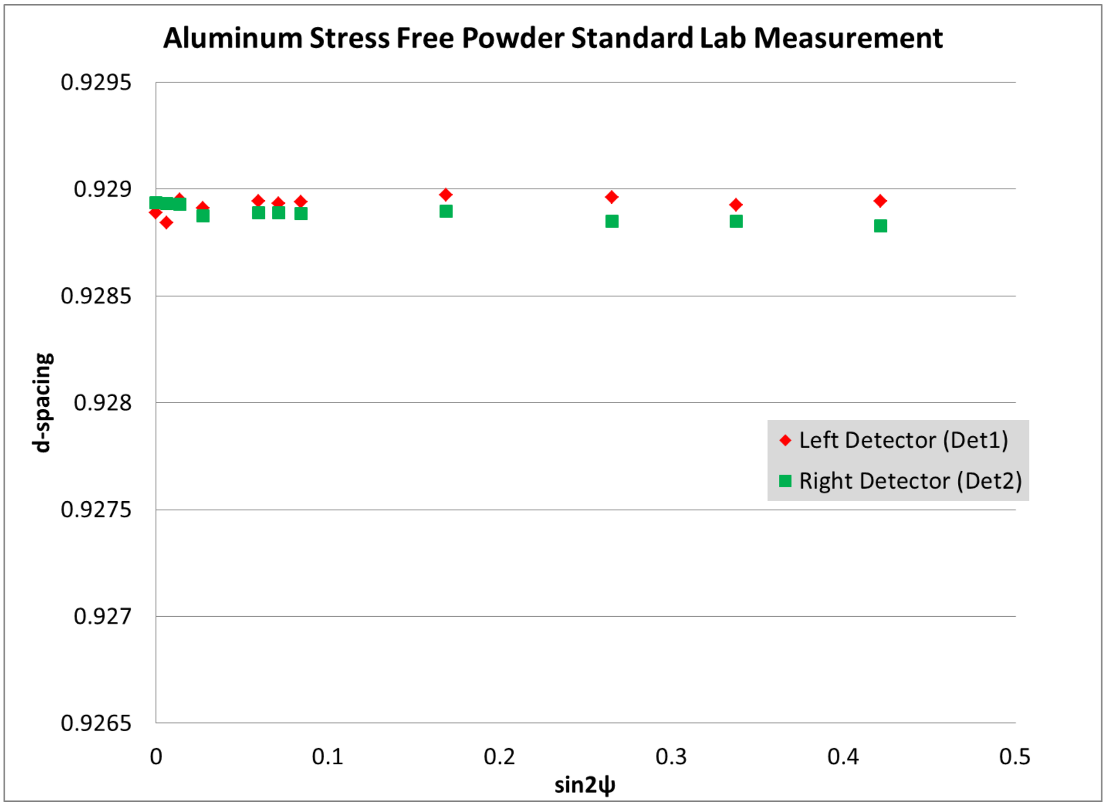

Figure 31. Sample d-spacing versus $\sin^2\psi$ plot for the aluminum stress free powder standard. Stress and out-of-plane shear stress were determined to be [-2.9± 1.7 MPa] and [-2.9 ± 0.8 MPa] respectively.

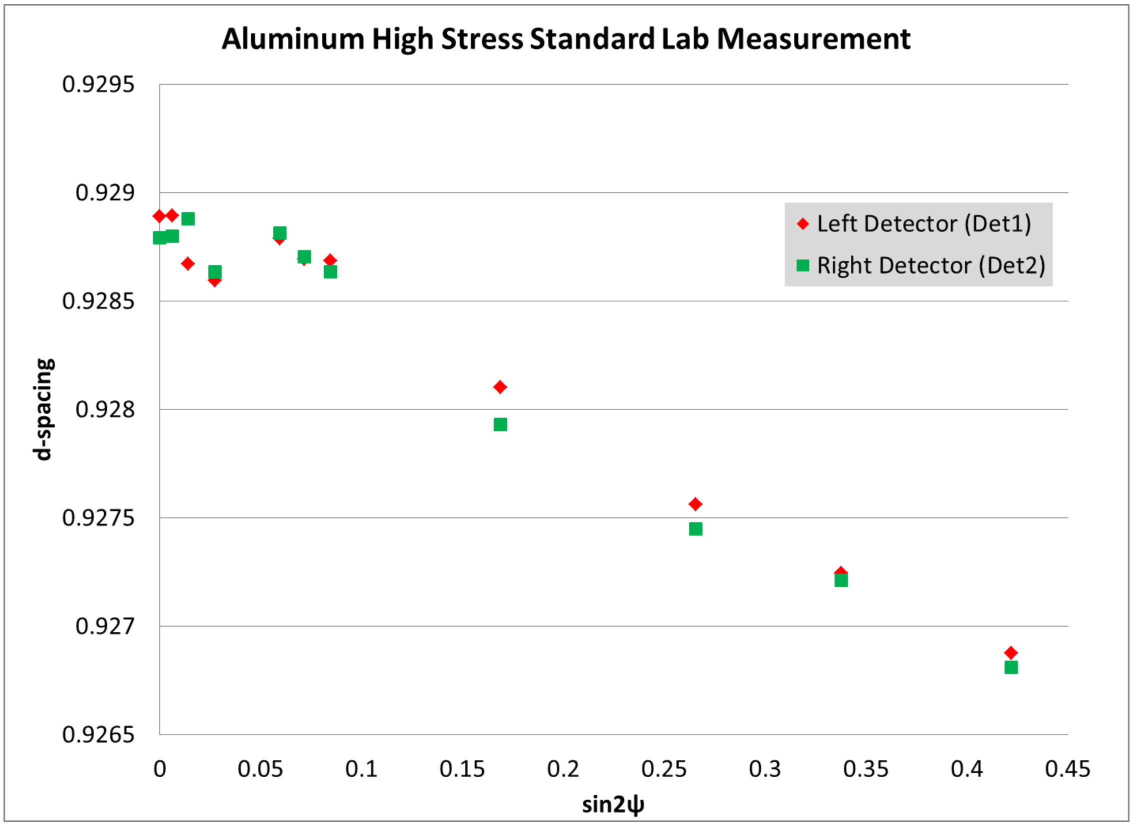

Figure 32. Sample d-spacing versus $\sin^2\psi$ plots for the aluminum high stress standard. Stress and out-of-plane shear stress were determined to be [-282.9 ± 8.3 MPa] and [-1.9 ± 4.0 MPa], respectively.

A. NON-SENSITIZED, SYSTEMATICALLY GAS TUNGSTEN ARC WELDED

Stress profiles across each of the “bead on plate” GTAW welds on the non-sensitized AA5456 plate showed tensile residual stresses exceeding 100 MPa as a result of welding. Higher power input resulted in a larger HAZ. The broadened region of tensile stresses shown in the 200 A/16.8 V/3360 W welds as compared to the 100 A/15.4 V/1540 W welds in Figure 33 indicated a wider HAZ. The faster weld travel speed resulted in higher tensile stresses at the weld center and a narrower distribution of tensile residual stresses across the weld. This is seen when comparing the 152.4 mm/min weld data with the 50.8 mm/min weld data (Figure 33). The error bars shown are from the fitting error of the d-spacing versus $\sin^2\psi$ plot for each point. The error is larger at the center of the weld due to the large grain size developed during fusion.

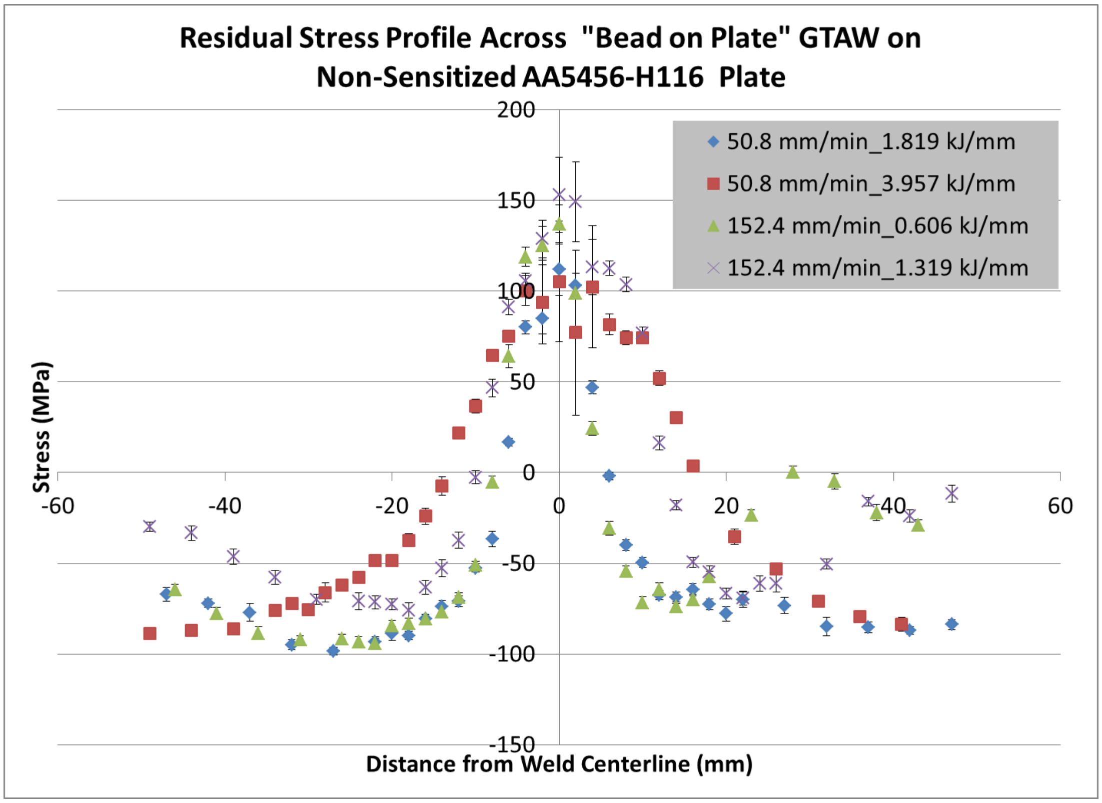

Figure 33. Residual stress measurements taken with the iXRD across the welds of the four GTAW welds on non-sensitized AA5456 plates. Measurements were taken parallel to the weld.

B. SENSITIZED, SYSTEMATICALLY ULTRASONIC IMPACT TREATED, GAS METAL ARC WELDED

The residual stress measurements taken across the control zones were representative of the residual stresses induced by the fusion of sensitized plates using GMAW (Figure 34). The results are expected to closely mimic those produced during repairs conducted on sensitized shipboard material without UIT. On the crown side of the weld, GMAW induced stresses near +80 MPa; whereas the root of the weld exhibited stresses significantly less, around +10 MPa. The large error bars at distance of less than 5 mm from the center of the weld are most likely due to the large grain size in the fusion zone. This large grain size can cause considerable scatter in the x-ray diffraction measurements.

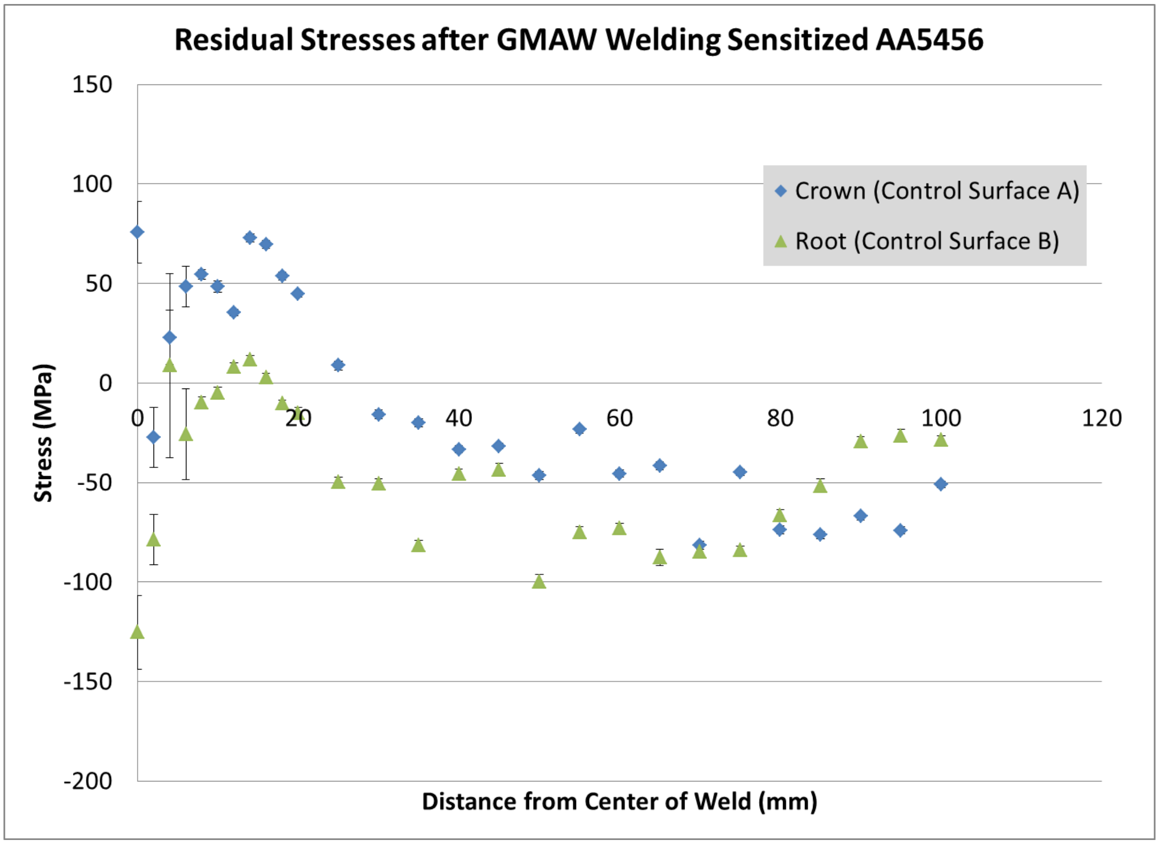

Figure 34. Longitudinal residual stresses measured as a function of distance perpendicular to GMAW on a surface without UIT.

The residual stress distributions across the welds after UIT clearly showed the effect of the peening process (Figure 35 through Figure 38). The data for each plate showed that UIT induces compressive stresses from the weld to the base material. The magnitude of the compressive stresses was in the range from roughly -100 MPa to -200 MPa in each case. UIT induced nearly the same magnitude of compressive stresses from the weld through the HAZ and into the base metal. The tensile stresses associated with the HAZ were completely removed by UIT. There were no longer the tensile regions that were clearly seen in each of the control surfaces. Surface B (60 percent power) showed the clearest difference in the effect of pin sizes. Based on the results of Surface B (60 percent power), 1 mm pins induced the greatest magnitude of compressive stresses, followed by 3 mm pins and 4 mm pins. The pin size dependence of the residual stresses was not as clear for the other power levels; however, the 1 mm pin consistently induced slightly more compressive stresses than the 3 mm or 4 mm pins at 20, 40, and 60 percent power. This trend is least obvious at 80 percent power. The difference between residual stresses induced by 3 mm and 4 mm pins is less distinguishable in all cases. The level of residual stress was not strongly affected by the power level during UIT.

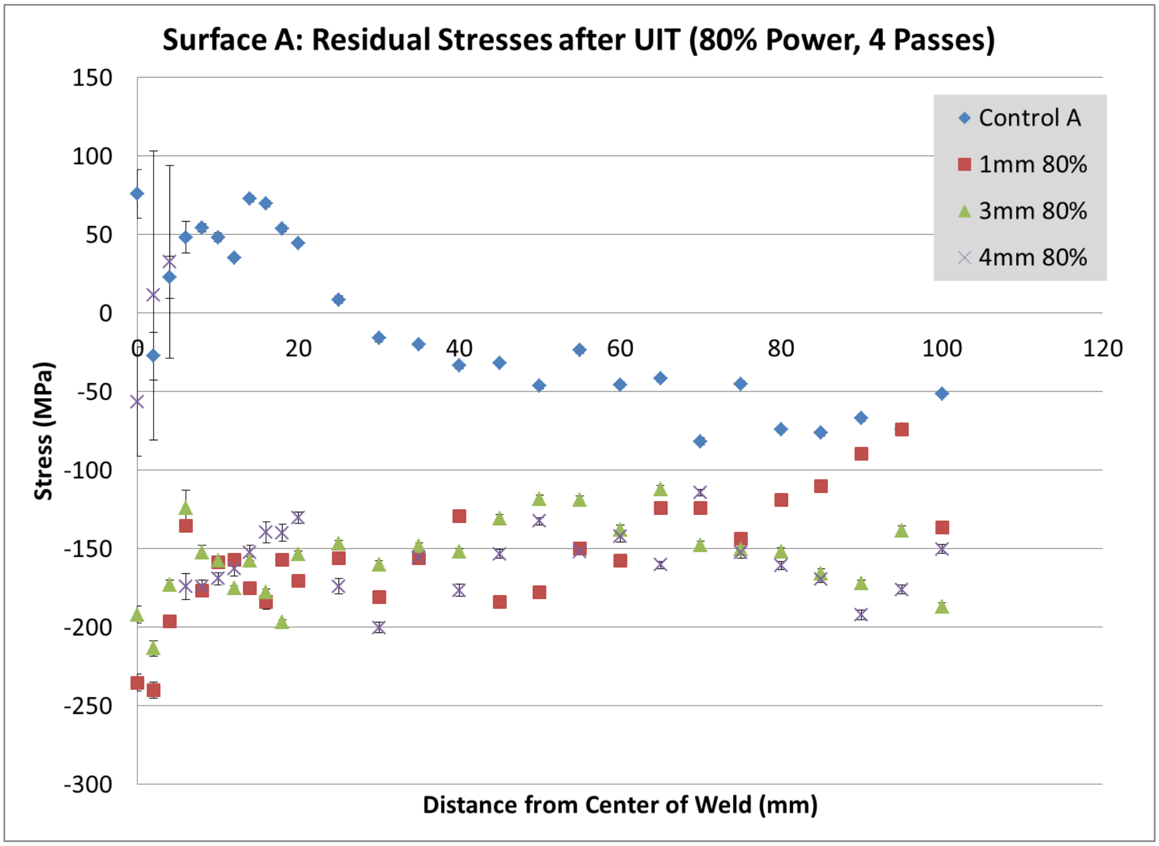

Figure 35. Residual stresses for the four zones (1 mm, 3 mm, and 4 mm UIT pins) of Surface A (80 percent power input).

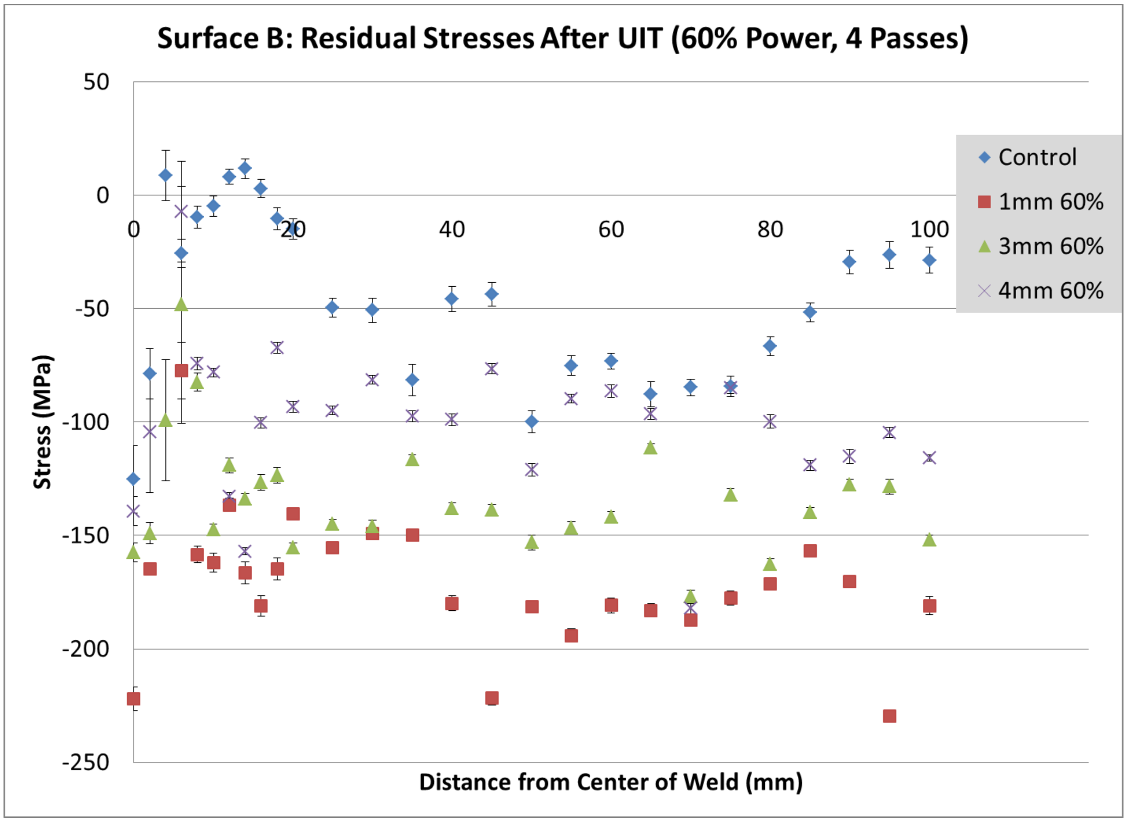

Figure 36. Residual stresses for the four zones (1 mm, 3 mm, and 4 mm UIT pins) of Surface B (60 percent power input).

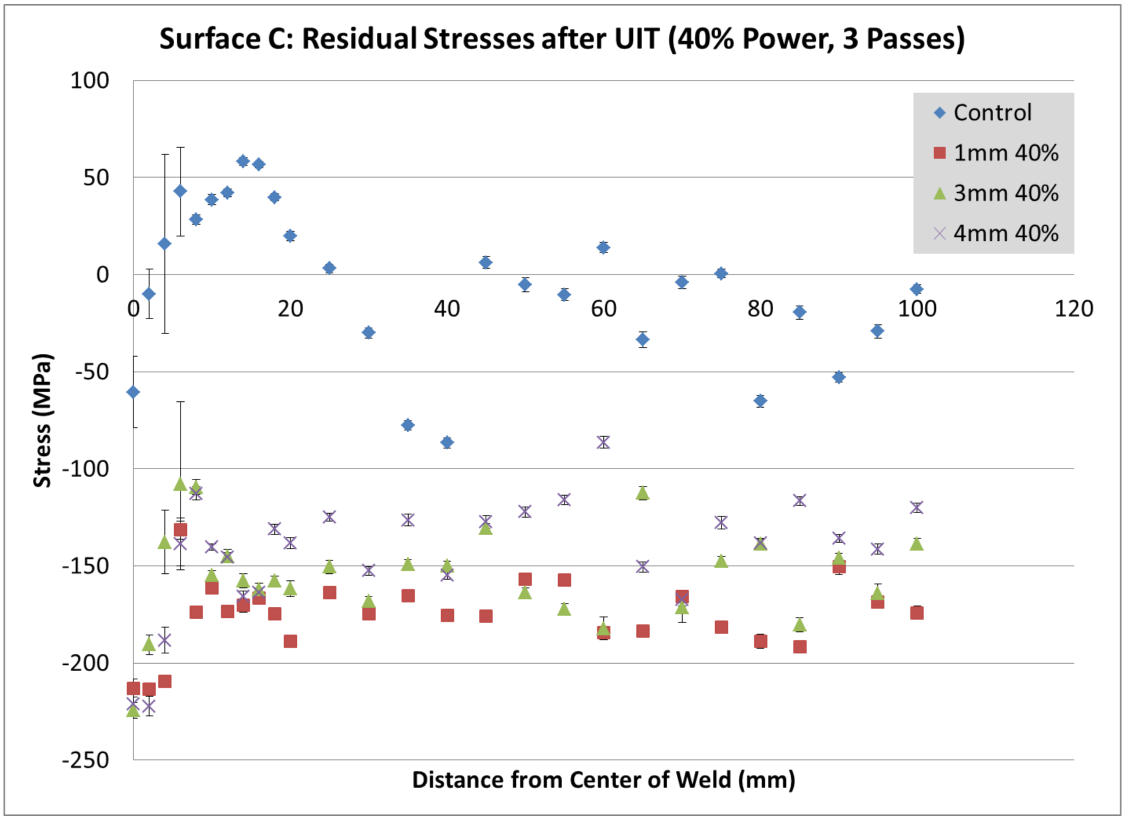

Figure 37. Residual stresses for the four zones (1 mm, 3 mm, and 4 mm UIT pins) of Surface C (40 percent power input).

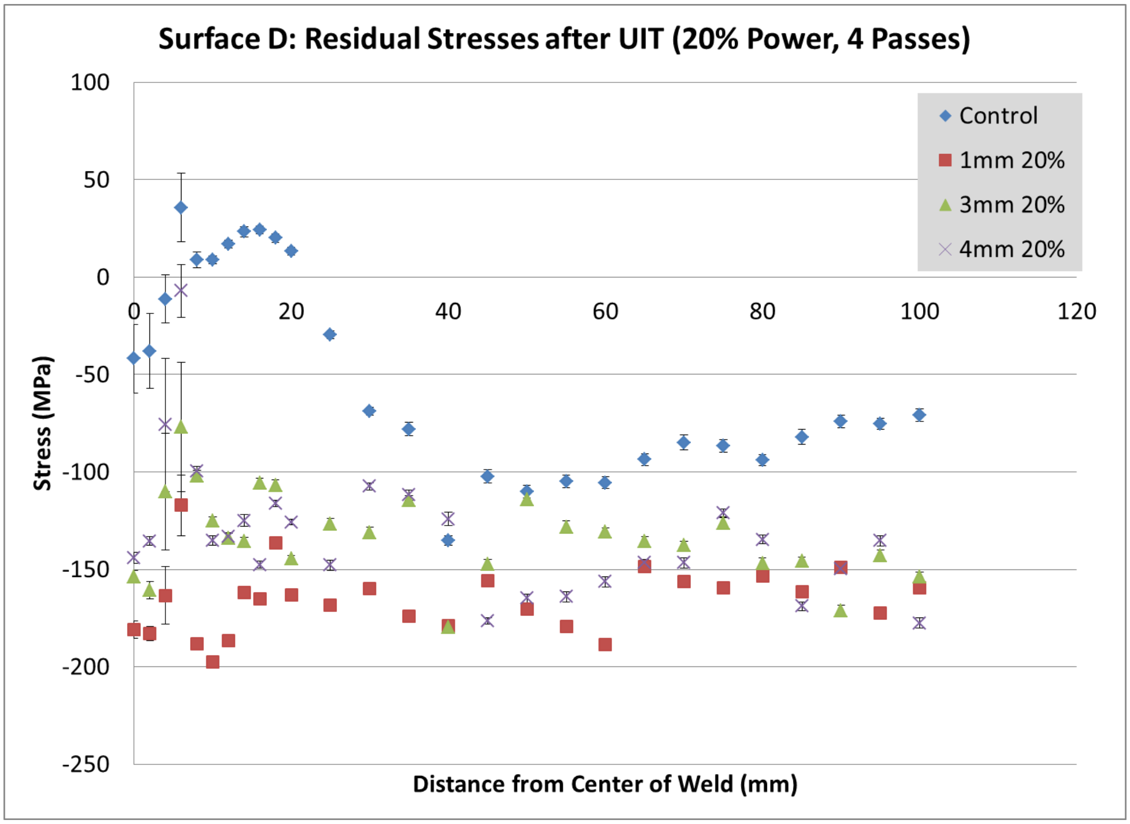

Figure 38. Residual stresses for the four zones (1 mm, 3 mm, and 4 mm UIT pins) of Surface D (20 percent power input).

The comparison of pin size and power was made clearer by examining only the residual stresses present in the base metal. The average residual stress in the base metal was determined by taking the mean value for the longitudinal residual stress at distances between 25-100 mm away from the weld center. The pin size was more clearly shown to affect the magnitude of compressive stresses induced at 20, 40, and 60 percent power (Figure 39). The 1 mm pin induced the most compressive stresses at 20, 40, and 60 percent power. The 3 mm pin induced the most consistent magnitude of stresses. The 4 mm pin induced the least compressive stresses at 40 and 60 percent power. The difference between the stresses induced by the 1 mm pin and the 4 mm pin ranged from about 20 MPa to 75 MPa (compressive). Overall, the results suggested that the residual stresses induced have a dependence on the pin size. The trend was seen particularly at 20, 40, and 60 percent power. There may be some dependence of the residual stress level upon the percent power, but the dependence was not strong.

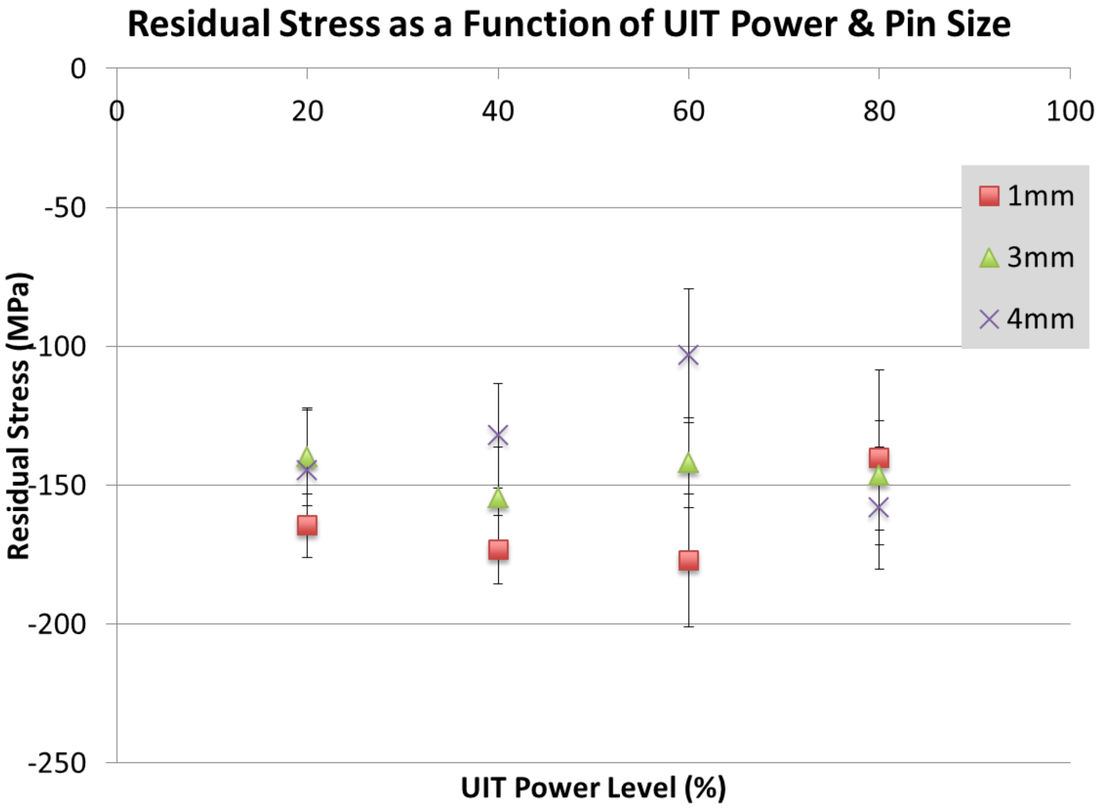

Figure 39. Magnitude of residual stresses in ultrasonically treated base metal suggests dependence on pin size and possibly percent power.

The depth resolved results (Figure 40) suggested that the magnitude of residual stresses induced is maintained to a depth of at least 0.6 mm below the surface, regardless of percent power or pin size. Regions of interest to conduct depth resolved measurements were established using the residual stress profiles above. The locations selected on Surface A (80 percent power) and Surface C (40 percent power) presented a wide array of data for comparison, to include:

- Measurements for 1 mm, 3 mm, 4 mm pin sizes
- Measurements for multiple power inputs
- Measurements of HAZ and base metal

UIT induced compressive stresses of -150 MPa to -250 MPa to depths of at least 0.6 mm in the HAZ and base metal. The results showed that the magnitude of stresses induced by UIT near the treated surface is comparable regardless of the power input or pin size in the HAZ and base metal.

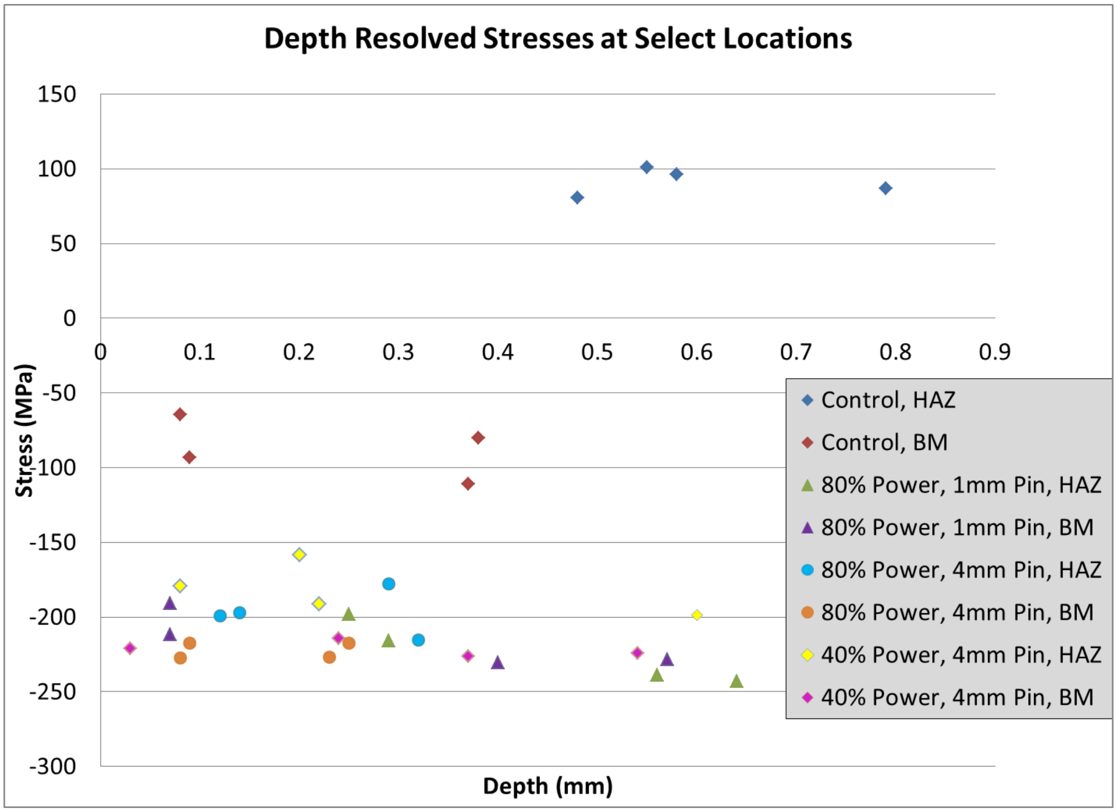

Figure 40. UIT induces compressive stresses to depths up to 0.6 mm. The power input and pin size do not create a great deal of variance.

The residual stress measurement repeatability was determined by taking seven measurements were across the 3 mm pin zone on Surface A (80 percent power input). The d-spacing versus $\sin^2\psi$ plot for the final measurement (y=100 mm) in each teach map is provided in Figure 41. The overlapping of this data demonstrates the repeatability of the residual stress measurements using the iXRD. The associated stress and out-of-plane shear stress values as determined by the XRDWIN software are given in Table 12. The standard deviation was calculated to be only about 2.6 MPa. The stresses at each point in the residual stress profile are shown in Figure 42 and reduced in Figure 43 to illustrate the standard deviation of stress at each point and the average of the fitting errors provided by the XRDWIN software. The maximum standard deviation of stress is 13.3 MPa at 6 mm from the weld center. The maximum average fitting error is 12.8 MPa at 4 mm from the weld center. These locations corresponded with the fusion zone and weld toe; the elevated values are most likely due to large grain size and shadowing.

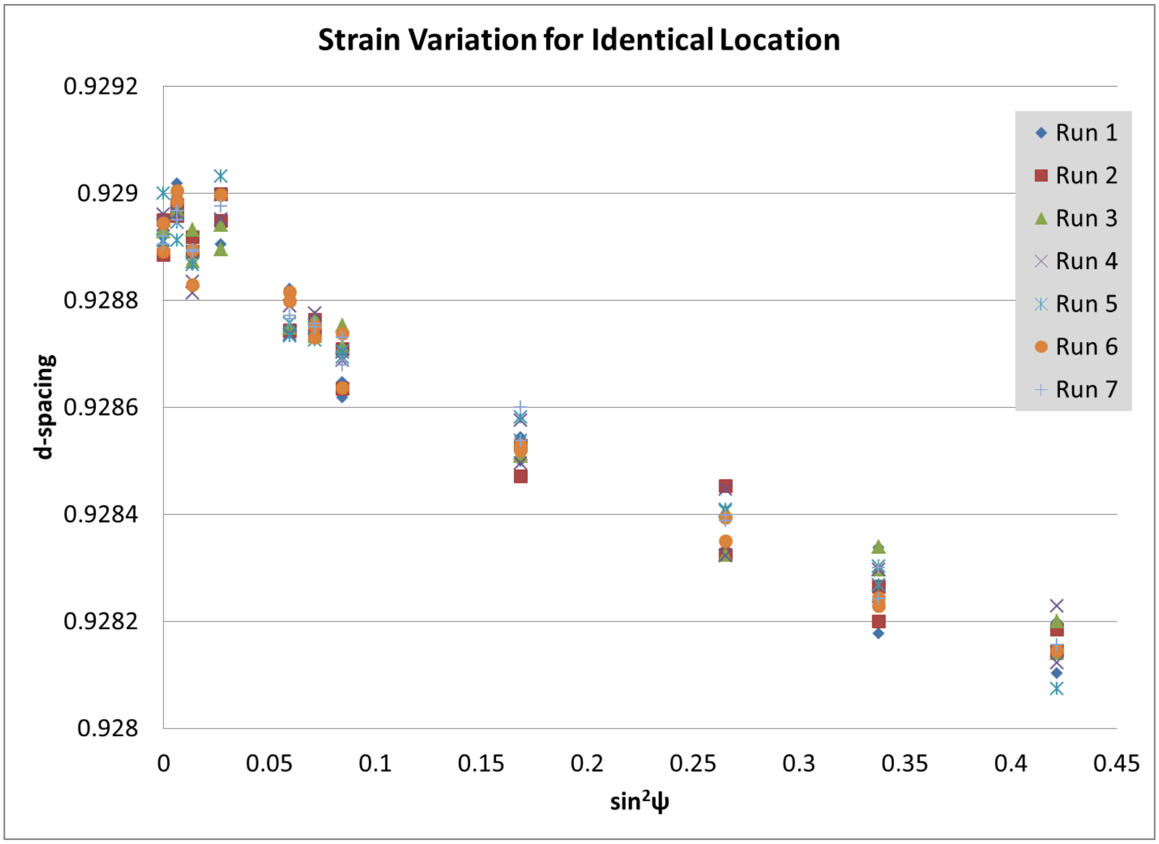

Figure 41. D-spacing results from seven measurements taken at the same location using identical parameters. These d-spacing values represent the data collected at the last point in the teach map.

Measurement	Stress (MPa)	Out-of-Plane Shear Stress (MPa)
Run 1	-111.7 ± 4.5	2.1 ± 2.1
Run 2	-111.5 ± 4.5	2.0 ± 2.1
Run 3	-107.2 ± 3.7	0.9 ± 1.8
Run 4	-107.8 ± 4.3	2.1 ± 2.0
Run 5	-109.0 ± 3.8	-0.2 ± 1.8
Run 6	-110.0 ± 4.4	-0.1 ± 2.1
Run 7	-104.5 ± 3.7	0.3 ± 1.8
Mean Value	-108.8 ± 4.1	1.0 ± 2.0
Standard Deviation	2.7 ± 0.4	1.0± 0.2

Table 12. Stress and out-of-plane shear stress data collected for the final point of seven teach maps conducted in the same location Surface A (80 percent power), 3 mm pin zone using identical parameters.

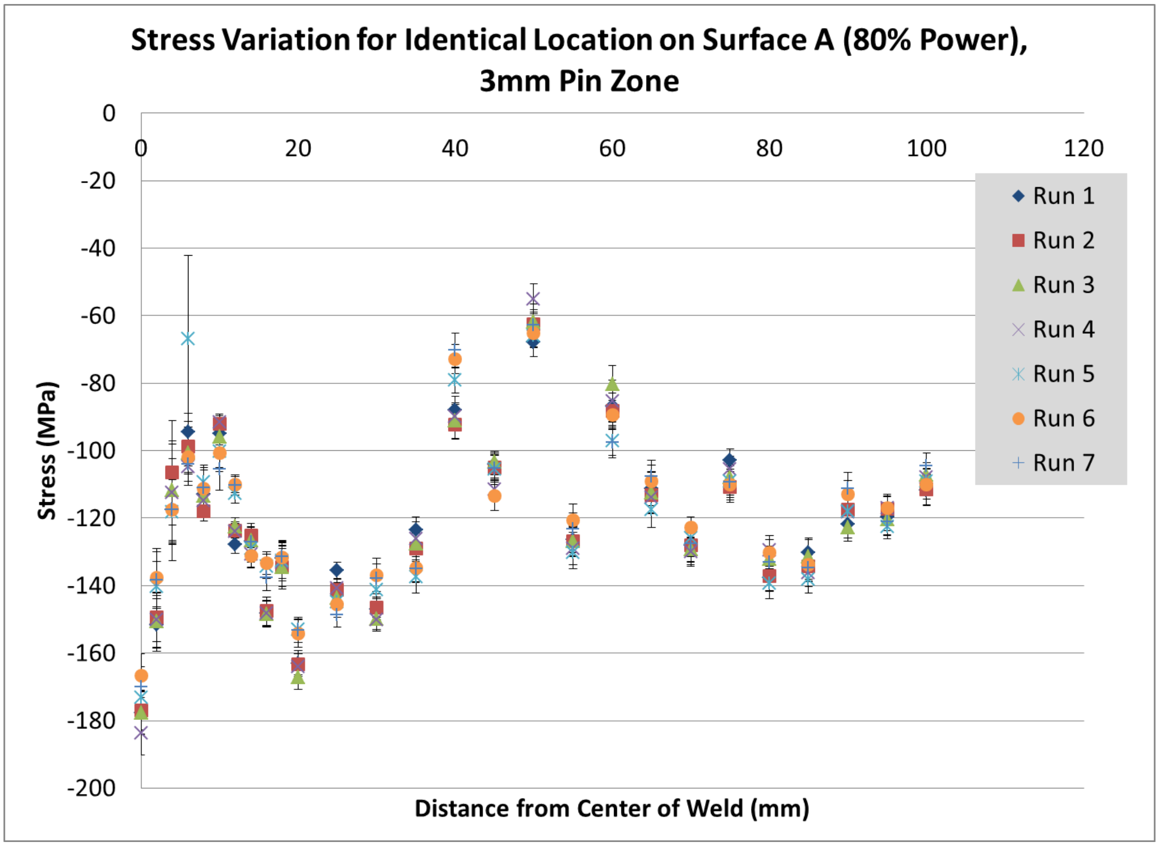

Figure 42. Stress measurements as calculated using the XRDWIN software based upon the data collected in the seven measurements at the same location using identical parameters.

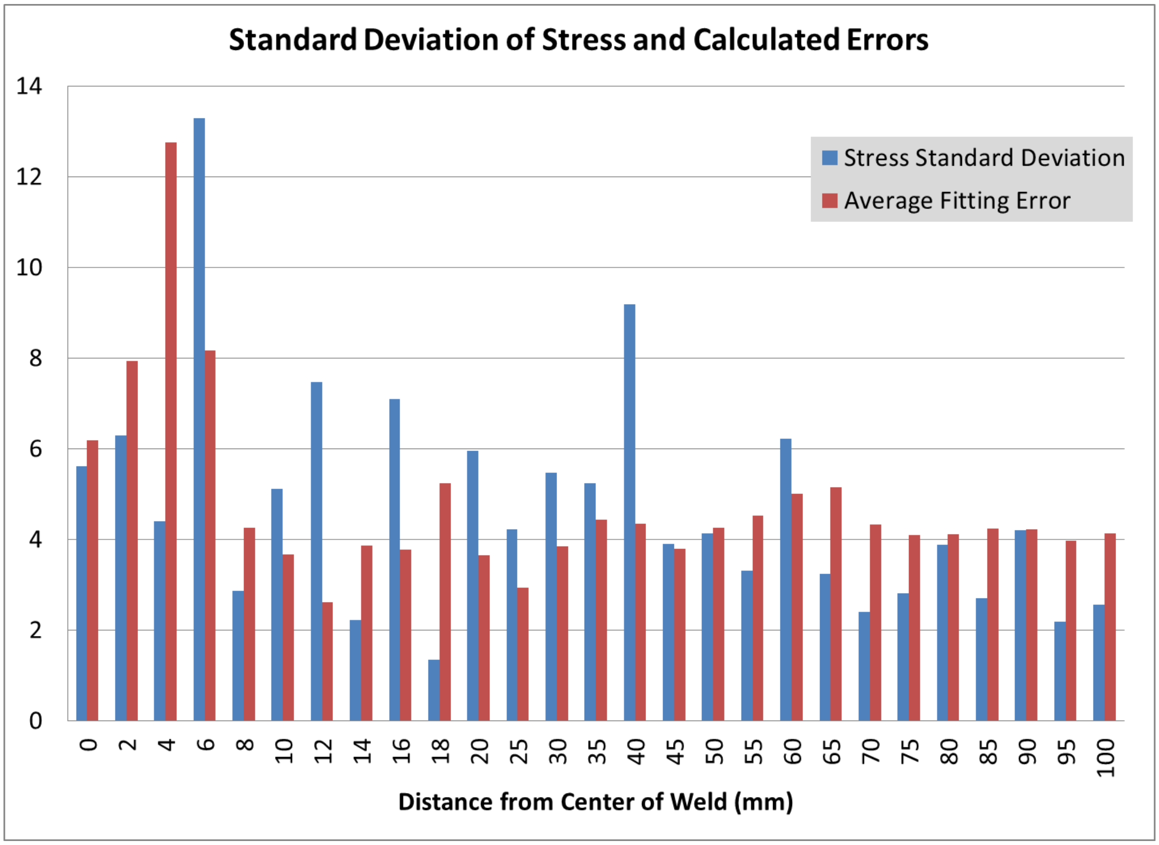

Figure 43. Variances in the stresses and the fitting errors at each point as determined by comparing the values obtained across all seven teach maps from the XRDWIN software.

Electron microscopy images and orientation maps showed clear evidence of the sub-surface deformation induced by the ultrasonic impact treatment process. In Figure 44(a), a crater left by one of the UIT pins on the crown surface of the weld is visible. A backscatter electron (BSE) image of the region just below the crater shows an extensive substructure as would be expected for severe plastic deformation (Figure 44(b) and Figure 45). A crack also appears to be present at the surface of the crater. BSE images under UIT pin craters in the HAZ (Figure 44(c)/Figure 44(d)) and in the base metal (Figure 44(e)/Figure 44(f)) do not show such clear plastic deformation.

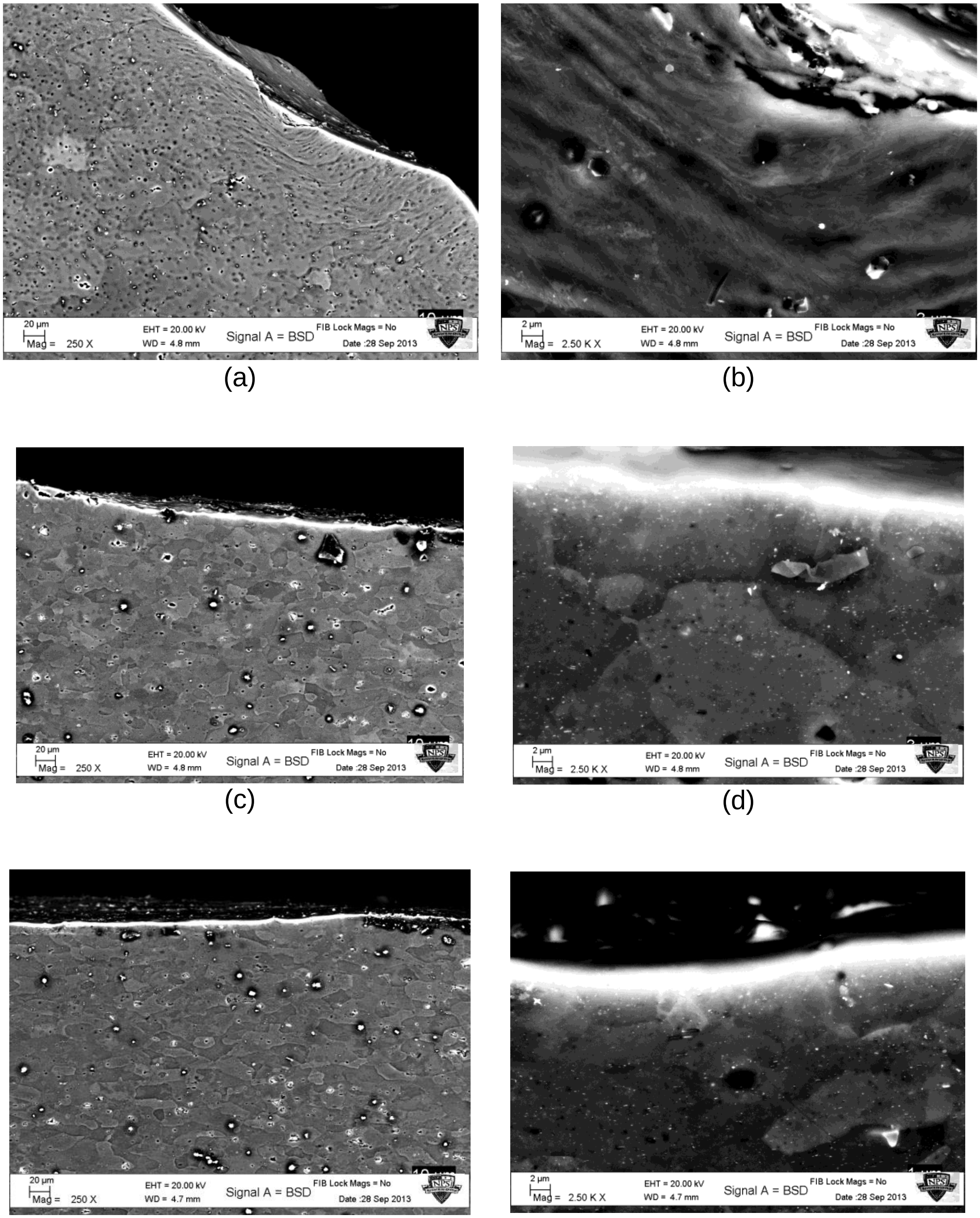

(a) (b)

(c) (d)

(e) (f)

Figure 44. Images captured from the crown (a, b), HAZ (c, d), and base metal (e, f) of Surface C (40 percent power) in the 1 mm pin zone. Images (b), (d), and (f) are higher magnification versions of images (a), (c), and (e).

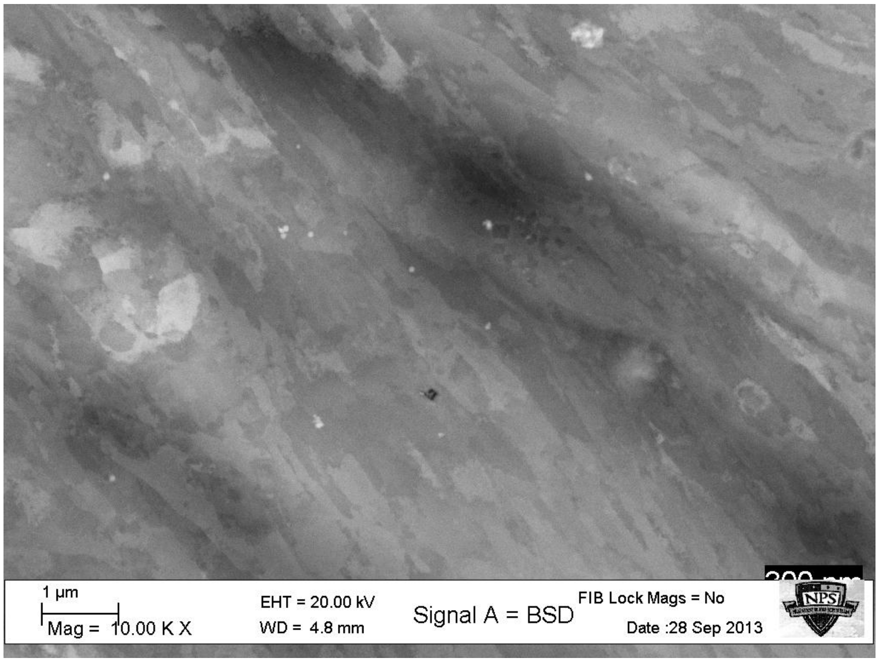

Figure 45. Higher magnification BSE image showing the deformation induced subgrain structure at a pin crater in Figure 44(b).

Figure 46 shows the grain size and shape under the UIT pin craters shown in the weld and base metal (compliments Figure 44(a) and Figure 44(e)). The average grain size in the fusion zone is approximately 40 µm, while the average grain size in the base metal is approximately 20 µm. Some evidence of the plastic deformation at the surface can be seen in these orientation maps from the mottled appearance in the color scheme and the inability of the software to consistently index the patterns. Mapping the orientation of the surface region (Figure 47), reveals that the severe plastic deformation has refined the grain structure such that the grains are only about 3 µm thick while closer to 30 µm in length. In addition, there is a several micron thick band of highly deformed material that cannot be systematically indexed with the collected EBSD data. It is quite possible that this data comes from aluminum that has become nanocrystalline after UIT.

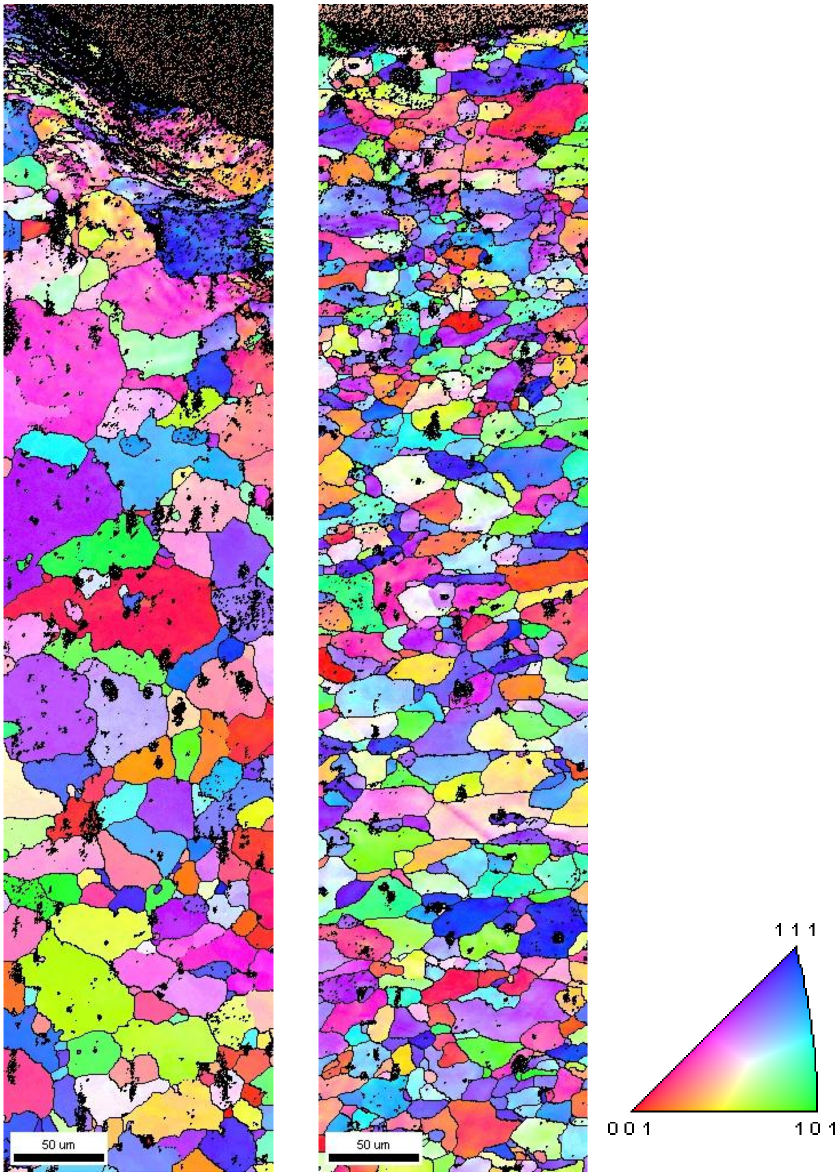

(a) (b)

Figure 46. Inverse pole figure map determined using the electron backscatter diffraction. Displays the grain orientations at the surface and subsurface in a pin crater in the weld (a) and the base metal (b).

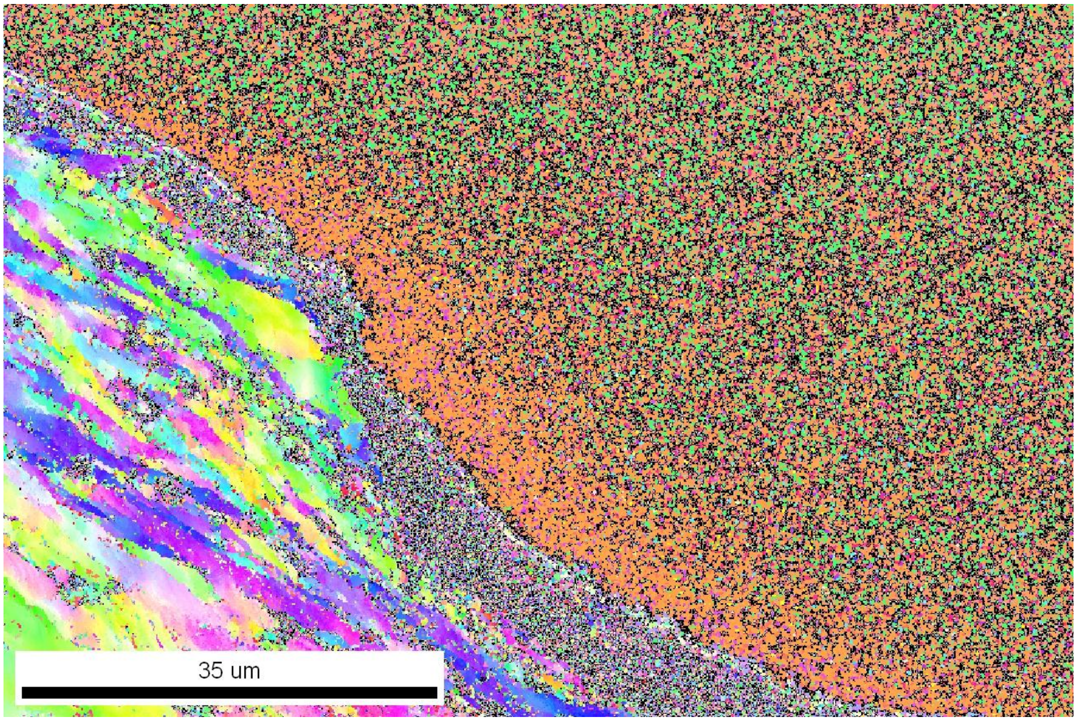

Figure 47. Inverse pole figure of deformed region at the surface of the UIT pin crater in the crown region of the weld.

The extent of plastic deformation created by UIT can be further quantified by mapping the degree of intragranular misorientation. There are several methods for plotting intragranular misorientation, but the grain orientation spread (GOS) was used here. The GOS first calculates the average orientation for each identified grain and then plots the scalar misorientation between every point in the grain and the average orientation. GOS values of 0.1-0.3 degrees are indicative of crystalline material with little plastic deformation while values of one degree and above demonstrate extensive plastic deformation. Maps of GOS clearly show the level and extent of plastic deformation after UIT (Figure 48). The crater in the crown region of the weld shows a zone of plastic deformation that extends approximately 150 µm below the surface of the crater (Figure 48(a)). The values of GOS are quite high and the grain to grain variation is also high. A clear zone of plastic deformation is also visible under a UIT pin crater in the base metal (Figure 48(b)). In this case, the GOS values are lower, as is the gradient in GOS. The extent of plastic deformation seems qualitatively to extend for at least 200 µm below the surface.

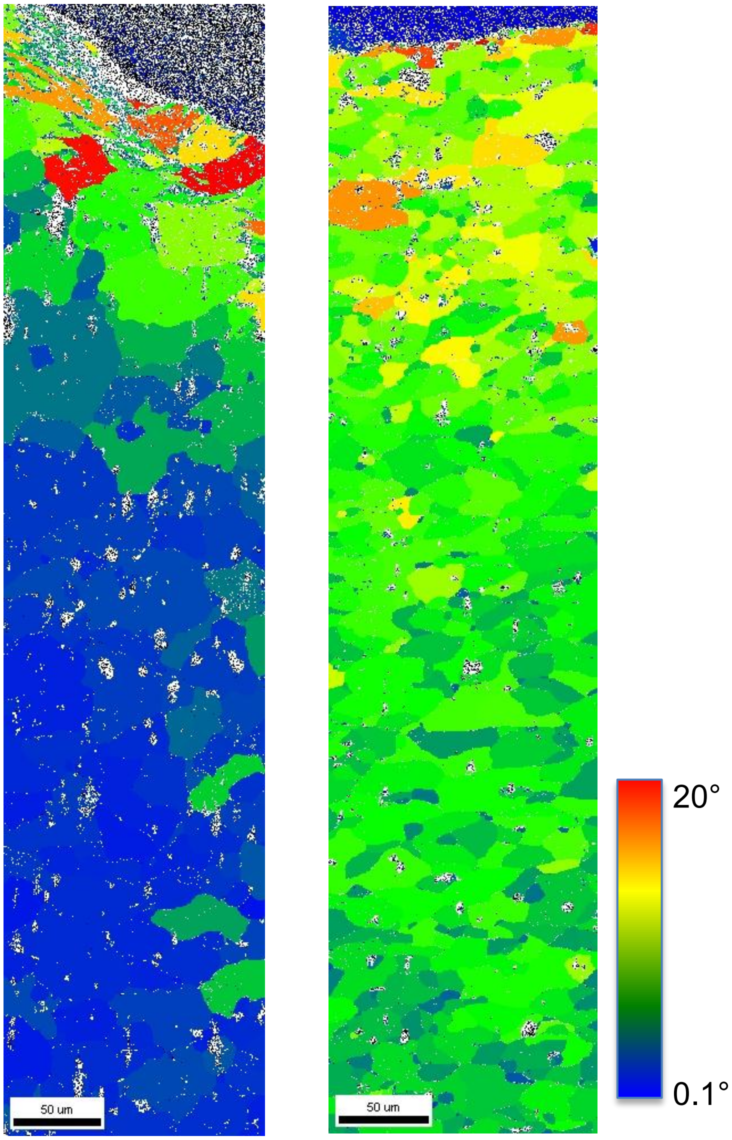

(a) (b)

Figure 48. Grain orientation spread found using electron backscatter diffraction for the weld (a) and base metal (b) at the surface and subsurface in a pin crater. The color scheme is in degrees. Red (20 degrees) denotes an area with a large amount of intragranular misorientation. Blue (0.1 degrees) denotes a region with very little intragranular misorientation.

Extensive intergranular cracking parallel to the UIT surface was observed in the heat affected zone (Figure 49 and Figure 50). Starting at a distance of 14 mm from the weld toe on the root side (Surface D, 20 percent power, 1 mm pin diameter), this intergranular cracking was visible throughout the HAZ to the end of the sample, a distance of 20 mm from the weld toe. Even more extensive intergranular cracking was observed on the crown side of the weld (40 percent power, 1 mm pin diameter). This cracking started right at the weld toe and continued throughout the HAZ to the end of the sample. The cracks were all Intergranular, primarily parallel to the surface and occurred in multiple layers to a depth between 100-200 μm below the surface. In contrast, no cracking was observed on the crown or root sides of the control weld (Figure 51).

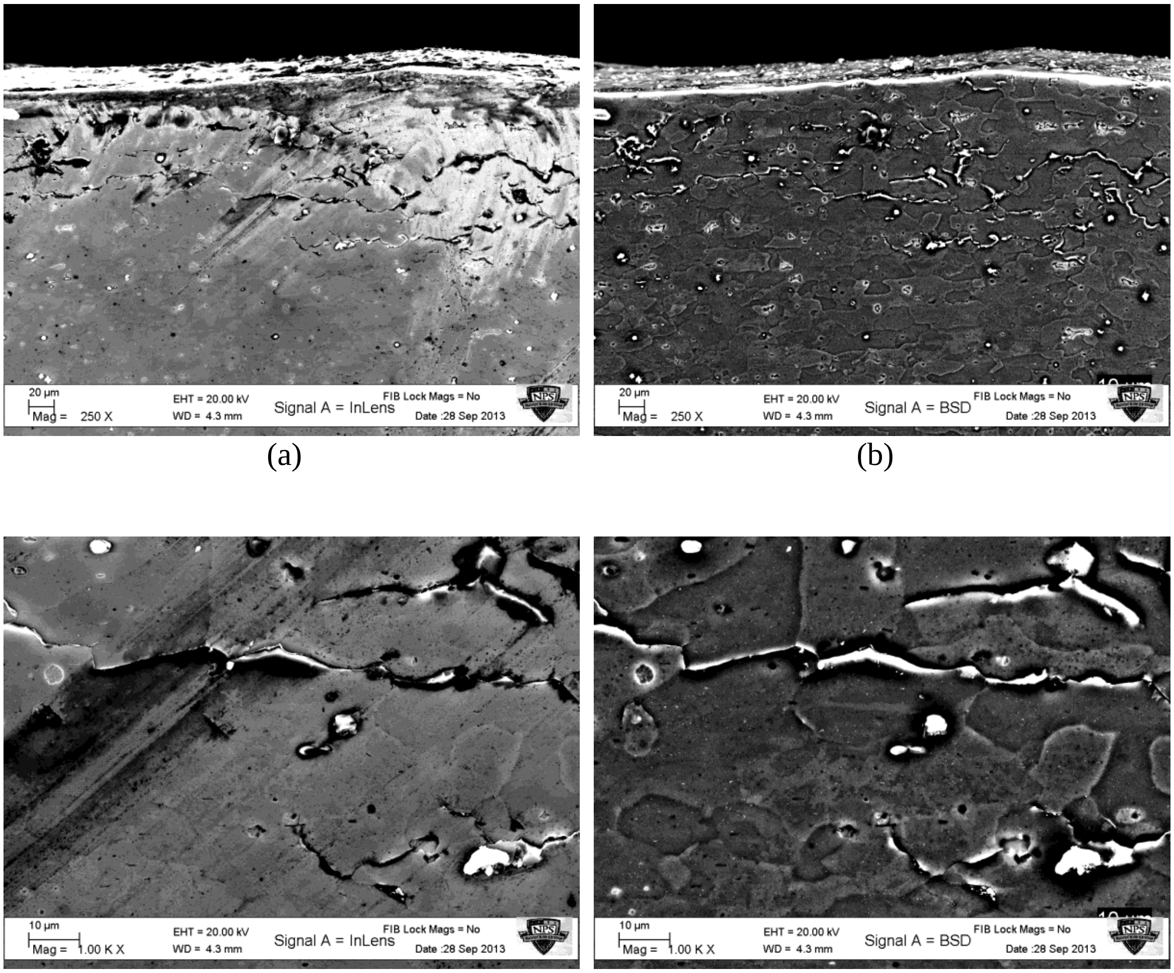

(a) (b)

(c) (d)

Figure 49. Images captured 14.6 mm from the toe of the weld, illustrating intergranular cracking. Image (c) and (d) are higher magnifications of image (a) and (b).

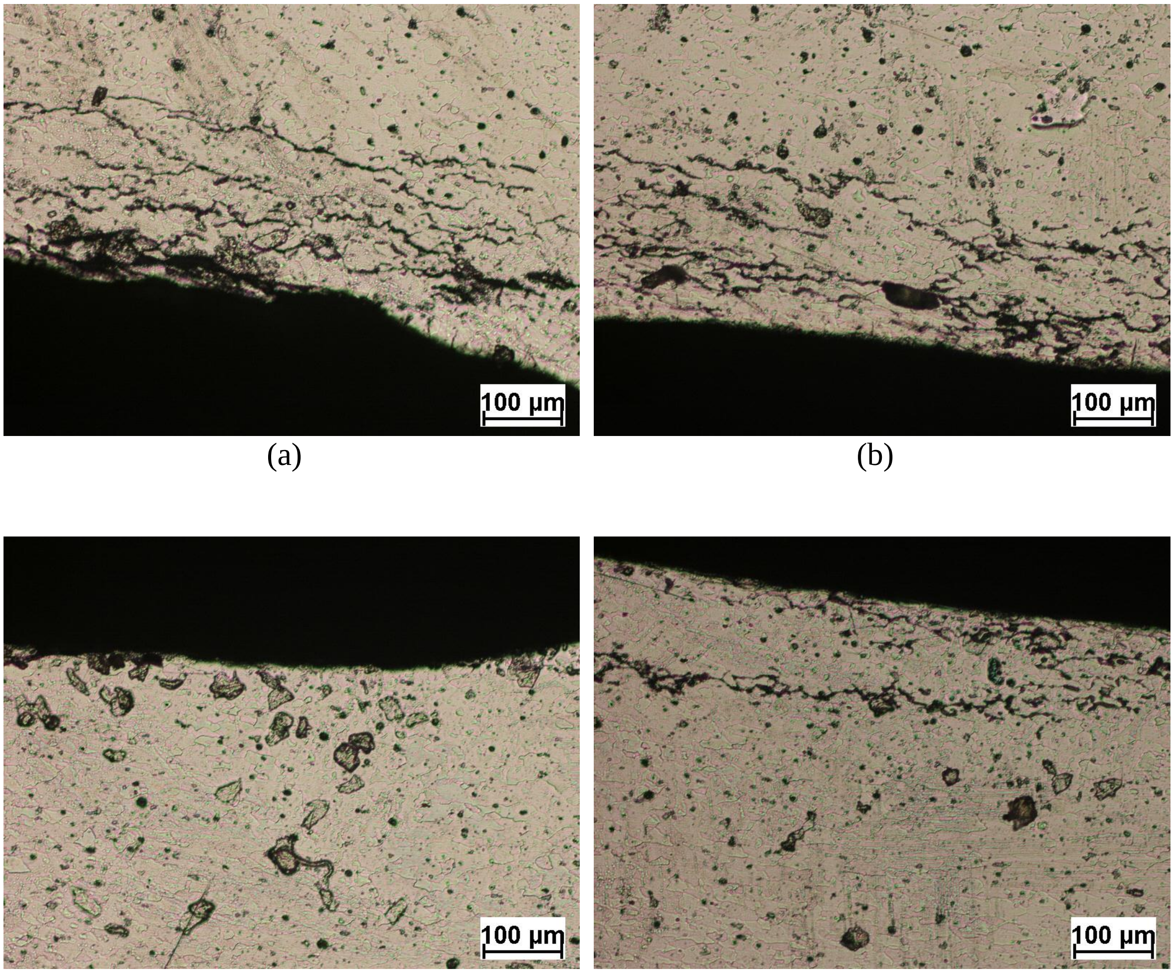

(a) (b)

(c) (d)

Figure 50. Optical microscopy images of sub-surface intergranular cracking in regions that have experience UIT with a 1 mm pin diameter. (a) 40 percent power at the toe of the weld, (b) 40 percent power in the HAZ, (c) 20 percent power at the toe of the weld, and (d) 20 percent power in the HAZ.

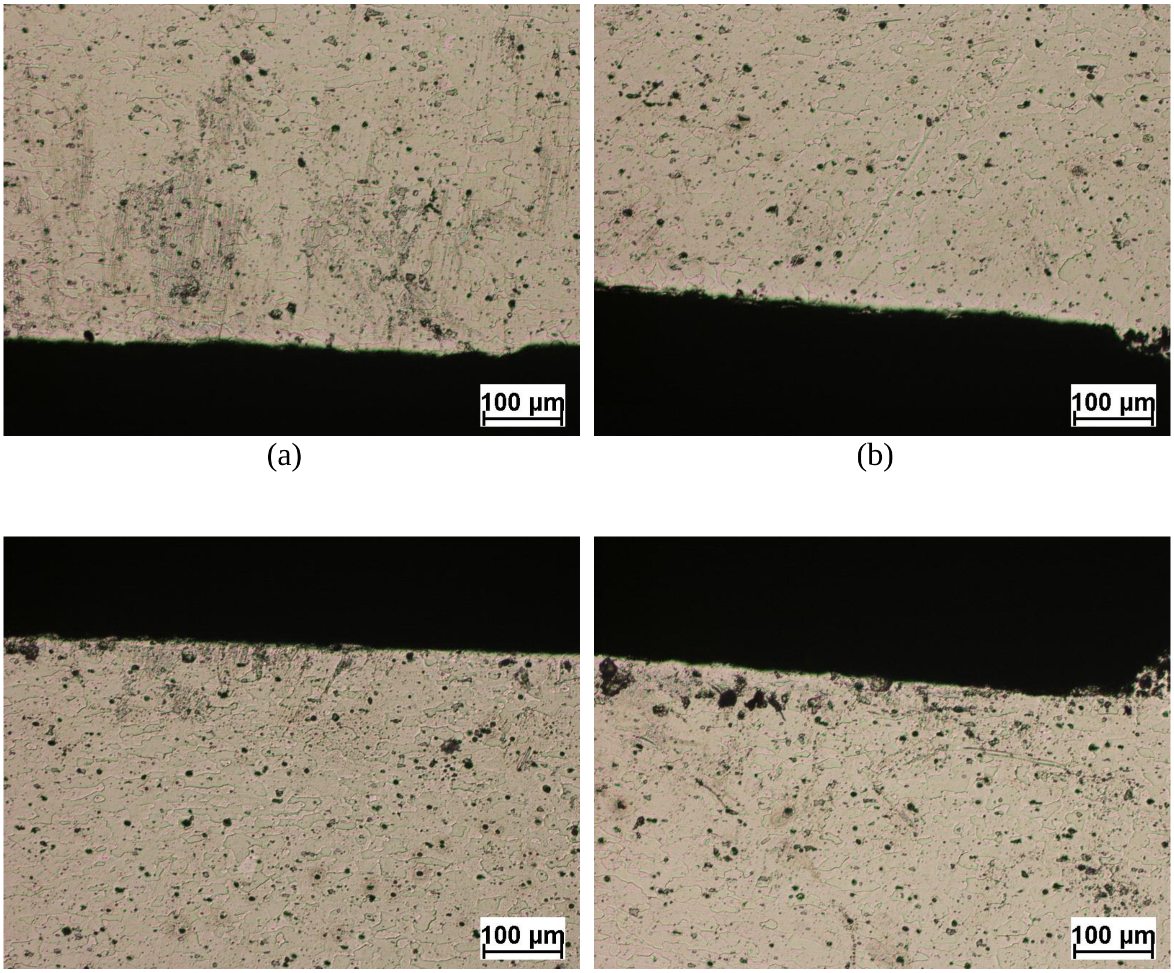

(a) (b)

(c) (d)

Figure 51. Optical microscopy images of sub-surface regions that have no UIT: (a) crown side of weld at the toe, (b) crown side in the HAZ, (c) root side of the weld at the toe, and (d) root side in the HAZ.

C. FIELD MEASUREMENT RESULTS

After assembly on the deck of the U.S. Navy cruiser, the iXRD instrument returned acceptable residual stress measurements for the stress free and high stress aluminum standards (Figure 52 and Figure 53). The d-spacing versus $\sin^2\psi$ plot shows a horizontal trend for the stress-free aluminum powder sample as expected. The d-spacing versus $\sin^2\psi$ plot did exhibit some slight, but systematic, branching. This branching was indicative of a small, out-of-plane shear stress component. The calculated normal stress value was 6.8±2.0 MPa; well below the 14 MPa limit for high quality measurements [69]. The value determined for out-of-plane shear stress was -12.6±1.0 MPa, which is higher than desired but also within the acceptable limits of ASTM-E-915 value of 14 MPa for acceptable alignment [69]. The diffraction measurements on the high-stress standard returned even better results. The d-spacing versus $\sin^2\psi$ plot shows a relatively linear plot with a negative slope and little branching. The measured normal stress was -275.0±9.1 MPa as compared to a standard value of -274±23 MPa. The measured out-of-plane shear stress was -8.8±4.3 MPa.

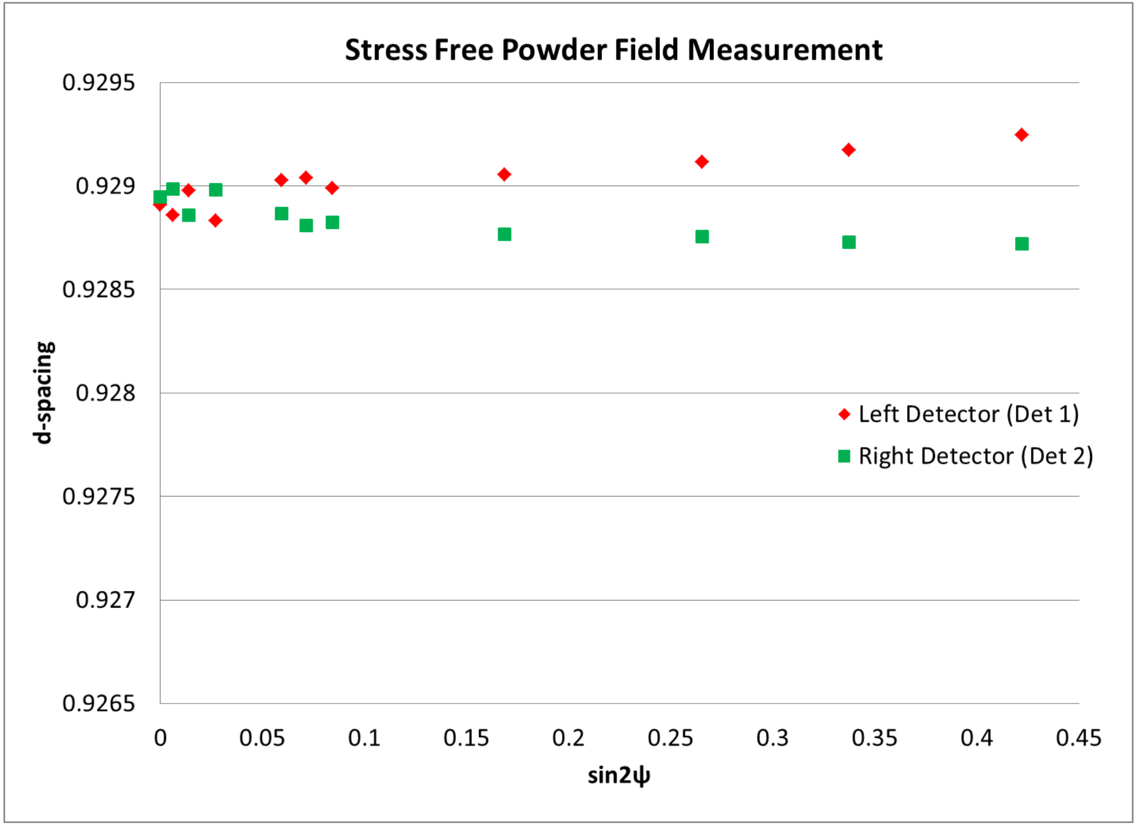

Figure 52. D-spacing results from the successful field measurement of the stress free powder standard. Stress and out-of-plane shear stress were determined to be [6.8 ± 2.0 MPa] and [-12.6 ± 1.0 MPa], respectively.

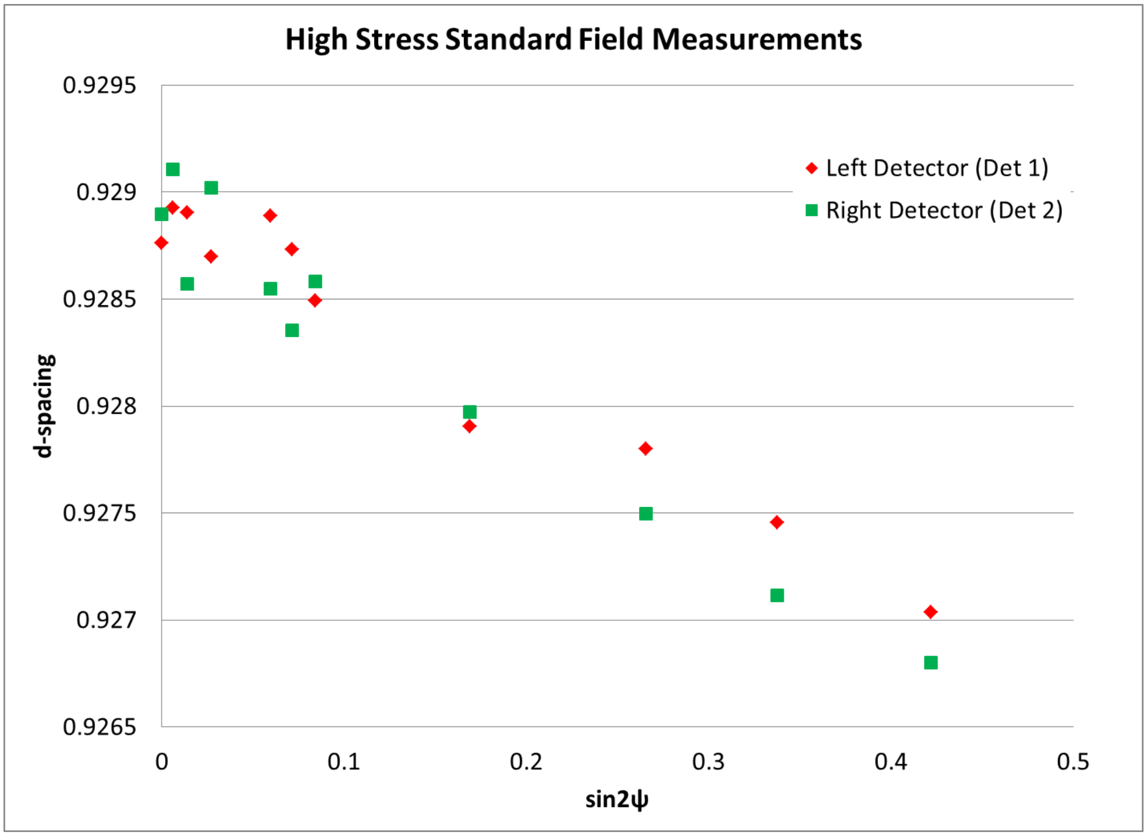

Figure 53. D-spacing results from the successful field measurement of the high stress standard. Stress and out-of-plane shear stress were determined to be [-275.0 ± 9.1 MPa] and [-8.8 ± 4.3 MPa], respectively.

The measured residual stresses obtained from the deck of a U.S. Navy cruiser were entirely compressive. Position 1(a), located outside the curved edge of the weld, was prepared using *in situ* metallography (Figure 54). The residual stress measurement returned a highly compressive value of -131.2 MPa (Figure 55). The surface in position 1(b) was prepared using a more basic metallographic polishing method in order to take line map from the weld towards the crack (also shown in Figure 54). The measurements collected at position 1(b) (Figure 56/Table 13) were the least compressive (-99 MPa) at the weld center. The results trended towards higher magnitude compressive stresses as measurements were taken away from the weld and closer towards the crack. These results suggest position one is compressive across the area investigated.

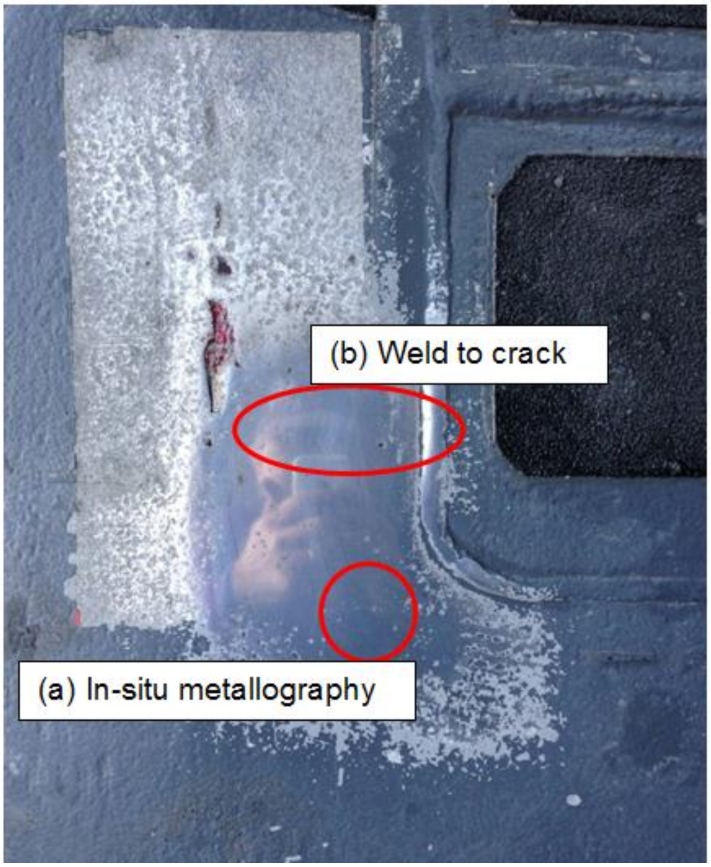

Figure 54. Position one located on the O4 deck of a U.S. Navy cruiser, polished for measurements. Location (a) was where the *in situ* metallography was conducted and location (b) was where the line profile was conducted from the weld towards the crack.

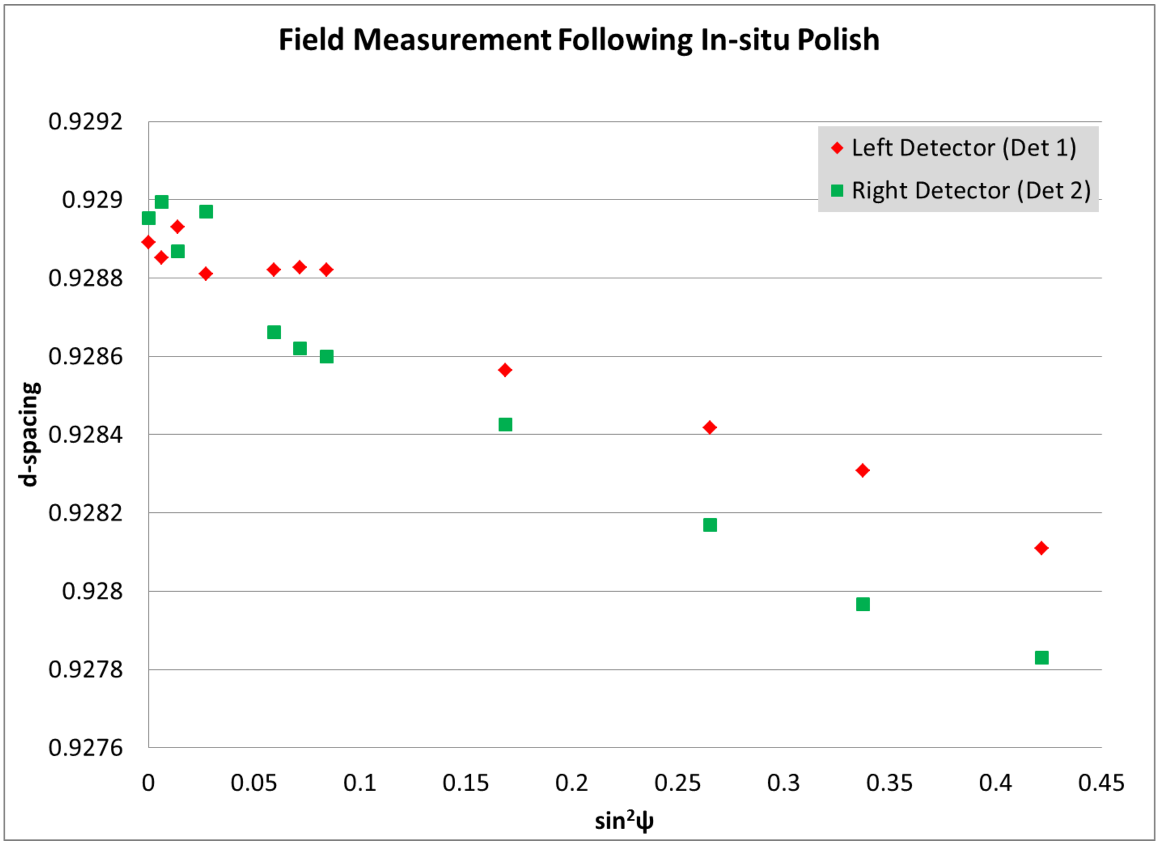

Figure 55. D-spacing of the successful field measurement on the deck of a U.S. Navy cruiser following Dr. Bill Golumbfskie's *in situ* polishing and subsequent microstructural observation using his field apparatus. Stress and out-of-plane shear stress values were determined to be [-131.2 ± 2.6 MPa] and [-8.9 ± 1.2 MPa], respectively.

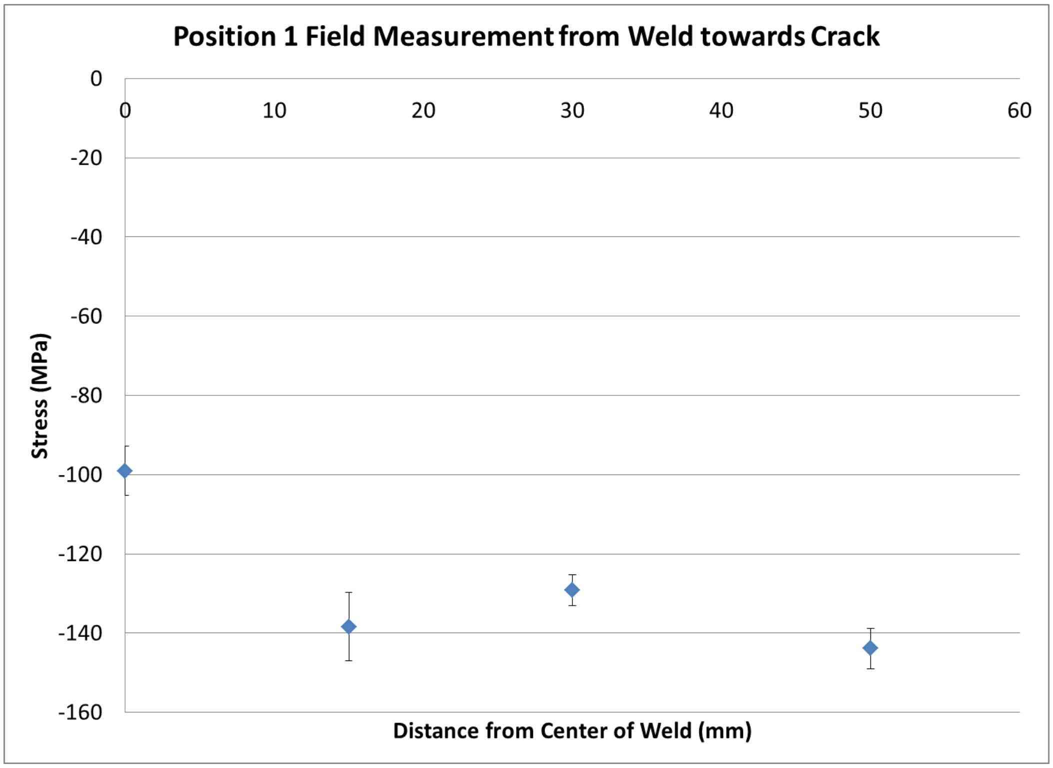

Figure 56. Stress profile initiated at the center of the weld and moved towards the crack at position one.

Distance from Center of Weld (mm)	Stress Parallel to Weld (MPa)	Out-of-Plane Shear Stress (MPa)
0	-99.1 ± 6.2	-4 ± 2.7
15	-138.4 ± 8.6	-9.4 ± 3.8
30	-129.2 ± 4.0	-13 ± 1.7
50	-143.9 ± 5.1	-10.7 ± 2.2

Table 13. Stress values at each point in the stress profile from the center of the weld towards the crack at position one.

The final measurements, taken at position two (Figure 57), resulted in compressive residual stresses of a similar magnitude (Figure 58/Table 14) as the stresses obtained at position 1(a) and 1(b). However, the magnitude was largest at the center of the weld, and decreased as measurements were taken further from the weld center, which is the opposite trend as that shown for position 1(b) (Figure 56/Table 13). It should be noted that sudden increase in material thickness was measured using ultrasonic methods just below this weld, while the deck plate itself was 6.35 mm (0.25 in) in thickness.

Figure 57. Position two located on the O4 deck of a U.S. Navy cruiser. The line profile was set up from the center of the weld towards the anticipated base material shown by the red oval.

Figure 58. Stresses collected in position two

Distance from Center of Weld (mm)	Stress Parallel to Weld (MPa)	Out-of-Plane Shear Stress (MPa)
0	-163.0 ± 5.6	-17 ± 2.6
18.5	-139.1 ± 7.1	-10 ± 3.4
60.34	-120.1 ± 4.5	6.6 ± 2.1

Table 14. Stress values determined for the teach map taken at position two.

THIS PAGE INTENTIONALLY LEFT BLANK

IV. DISCUSSION

Using the three dimensional Rosenthal's solution (Equation 9), it was possible to predict the width of the expected fusion zone and HAZ for AA5456 at the various parameters of GTAW based on the temperature gradient in the material [30].The three-dimensional solution was used because the thickness of the plate was much larger than the depth of the fusion zone (32.43 mm plate thickness). The MATLAB code provided in the Appendix was used to determine the fusion zone and HAZ for AA5456 [70]. The conditions in Table 15 were used to solve Rosenthal's solution and compared to the measured fusion zone and the HAZ seen in the residual stress profiles (Table 16). The HAZ was determined from the residual stress measurements as the point at which the values were no longer tensile.

$$\frac{2\pi(T-T_o)kR}{Q} = e^{\frac{-V(R-x)}{2\alpha}} \qquad \text{Equation 9.}$$

Where

- T = temperature
- T_o = workpiece temperature before welding
- k = workpiece thermal conductivity
- Q = heat transferred from heat source to workpiece
- V = travel speed
- α = workpeice thermal diffusivity
- R = radial distance from origin
- I = current
- V = voltage

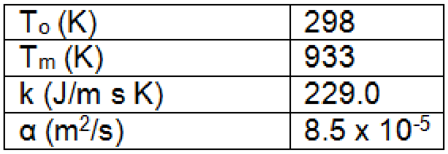

T_o (K)	298
T_m (K)	933
k (J/m s K)	229.0
α (m^2/s)	8.5×10^{-5}

Table 15. AA5456 material characteristics and atmospheric conditions considered for solving Rosenthal's 3-D solution.

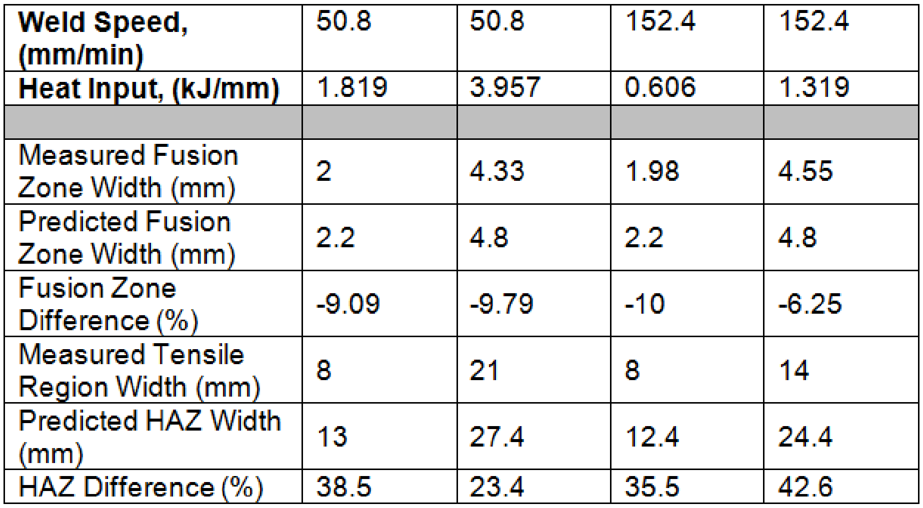

Weld Speed, (mm/min)	50.8	50.8	152.4	152.4
Heat Input, (kJ/mm)	1.819	3.957	0.606	1.319
Measured Fusion Zone Width (mm)	2	4.33	1.98	4.55
Predicted Fusion Zone Width (mm)	2.2	4.8	2.2	4.8
Fusion Zone Difference (%)	-9.09	-9.79	-10	-6.25
Measured Tensile Region Width (mm)	8	21	8	14
Predicted HAZ Width (mm)	13	27.4	12.4	24.4
HAZ Difference (%)	38.5	23.4	35.5	42.6

Table 16. Comparison of physical measurements and residual stress measurements with those predicted by the 3-D Rosenthal's solution.

The data collected in the GTAW, non-sensitized AA5456 plates demonstrates a strong dependence of breadth of HAZ on heat input and a dependence of the maximum tensile stress on weld travel speed. The agreement between these measurements and the theoretical predictions from the Rosenthal equations is close enough to demonstrate that x-ray diffraction is a valid method for mapping residual stresses across welds. As heat input increased, a broader the heat affected zone and region of tensile residual stresses were observed. This increased in width was due to a lower thermal gradient. This width of the tensile zone ranged from 8 mm for the two lower heat input conditions to 21 mm for the largest heat input condition. Higher weld travel speed resulted in higher peak residual stresses at the center of the weld, ranging from +100-150 MPa. The scatter in the stress values within the fusion zone is significant because the grain size becomes large. Kohandehghan et al. performed a combined finite element model and experimental study of GTAW on the related alloy AA5251 using 2 mm thick plate with heat inputs ranging between 116-202 J/mm [71]. They predicted a maximum tensile, longitudinal residual stress of 140 MPa, which is quite similar to the values measured here, despite the larger weld travel speed and consequent lower heat input. They predicted a tensile, longitudinal residual stress width of approximately 20 mm, but measured a width closer to 15 mm using the hole drilling technique. The Rosenthal solution consistently returned larger values compared with measured values in this research as well.

By comparison, the longitudinal residual stresses from GMAW on sensitized AA5456 plate had a greater breadth and a lower magnitude. The breadth on the crown side of the weld was almost 40 mm and ranged in maximum longitudinal stress value from 25-75 MPa. The heat input was 851 J/mm. It should be noted that some compressive stress was present in the base plate itself, which likely lowered the observed tensile stresses in the HAZ. A similar, but cleaner, result for longitudinal residual stresses after GMAW in AA5083 is seen in Figure 7 by James et al. [31]. In this case, the maximum longitudinal residual stress was displaced by approximately 20 mm from the weld center. The heat input was 560 J/mm. The maximum observed longitudinal residual stress was (+80-90 MPa).

The ultrasonic treatments reported in this thesis were all effective in mitigating the tensile stresses induced by GMAW in sensitized AA5456. As mentioned in the results section, the compressive stresses induced by UIT removed all of the tensile residual stresses in the HAZ. The maximum tensile stresses present in the control zones reached a measured value over +70 MPa in the HAZ on the crown of the weld and +24 MPa on the root of the weld. The average of the compressive stresses induced on all surfaces after UIT was ≤ -140 MPa. The average compressive stresses induced on the crown side of the plate was -154.3 ± 12.1 MPa and on the root side of the plate was -139.4 ± 23.5 MPa. The proximity of these two averages suggests that UIT induces a nearly uniform compressive stress on AA5456 regardless of initial stress of the plate. This conclusion with regards to crown and root compressive stresses has not been reported in other research, but Liao et al. showed that for a single set of UIT parameters tested on AA7075 at various levels of corrosion, the compressive stresses induced on each surface were of a similar magnitude to a depth of 1 mm (Figure 12) [58].

The depth resolved measurements revealed that the compressive stresses were present to a depth of 0.6 mm in several zones. Further depth resolved measurements are needed to determine where the stresses end and tensile stresses begin. Other reports suggest compressive stresses exist from 1.5 mm to 4 mm in various materials [55]–[58], [72]. Since both sides of the roughly 6.35 mm plates were treated with UIT, it is expected that at a depth near 2 mm, the residual stresses would begin to turn tensile. Surface material was removed using the “L1” solution with the electrolytic polisher. This solution did not remove material at a steady rate in each zone. The solution was chilled for each use, but still required varying amounts of time to achieve material removal in each zone. The HAZ and base metal for the welded plate without UIT only required about five minutes of electropolish, while other zones required up to 30 minutes and removed only 0.01 mm of surface material. Measurements were collected at depths up to 0.6 mm in several zones, but a more regularized material removal solution would be beneficial for clear depth resolved data.

The dependence of compressive residual stress on pin diameter might be modeled based upon spherical indentation. Of the two parameters: pin diameter and displacement amplitude (percent power), this research suggests that the residual stresses induced have more dependence on the pin size than on the percent power. This dependence may be explained by treating the UIT pins as spherical indenters (Figure 59).

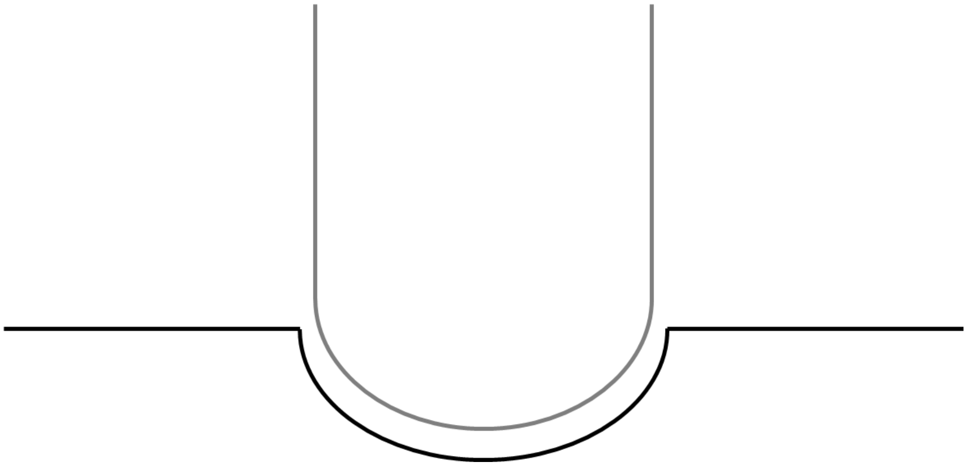

Figure 59. Image of spherical indenter used for comparison of the pin size results.

The mean pressure below a spherical contact with a flat surface is given by Equation 10 [73].

$$P_m = \frac{4}{3\pi} E_r \frac{a}{R} \qquad \text{Equation 10}$$

Where

- P_m = pressure underneath the pin contact
- E_r = reduced modulus
- R = radius of UIT pin
- a = contact radius between the pin and the sample surface

The reduced modulus, E_r, is related to the elastic properties of the sample, E_s and v_s (aluminum), and the indenter/UIT pin, E_i and v_i (hardened steel) (Equation 11). For this research, these values can be taken to be 70 gigapascal (GPa), 0.35, 200 GPa, and 0.3 respectively.

$$E_r = \left[\frac{1-\nu_i}{E_i} + \frac{1-\nu_s}{E_s}\right]^{-1} \qquad \text{Equation 11.}$$

The contact radius, a, is related to the pin radius, R, and the imposed depth of the indentation, h. The values of h are given in column four of Table 8 and are directly related to the power used during UIT.

The relationship between a, R, and h is shown in Equation 12. The data in

$$a = \sqrt{2R * h - h^2} \qquad \text{Equation 12.}$$

Figure 39 can be re-plotted as residual stress as a function of mean pressure (Figure 60). A roughly linear decrease in longitudinal residual stress with increasing contact pressure can be seen in this figure; however, two potential outliers obscure the overall trend. The point with the highest contact pressure, 11 GPa, had a much lower residual stress value than expected. This data point corresponds to the 80 percent power, 1 mm pin diameter measurement. In Figure 36, the last several points for this UIT condition systematically decrease in compressive residual stress, suggesting that the end of the UIT region had been reached and that the residual stress values were transition back to the control plate values. In addition, careful inspection of these shipboard plates shows a significant amount of grinding and other sorts of damage marks that may have influenced the measurements. These measurements will be repeated on non-sensitized, laboratory plates in the future. The data from these plates may allow for a much cleaner analysis of the residual stress and its relationship to contact pressure.

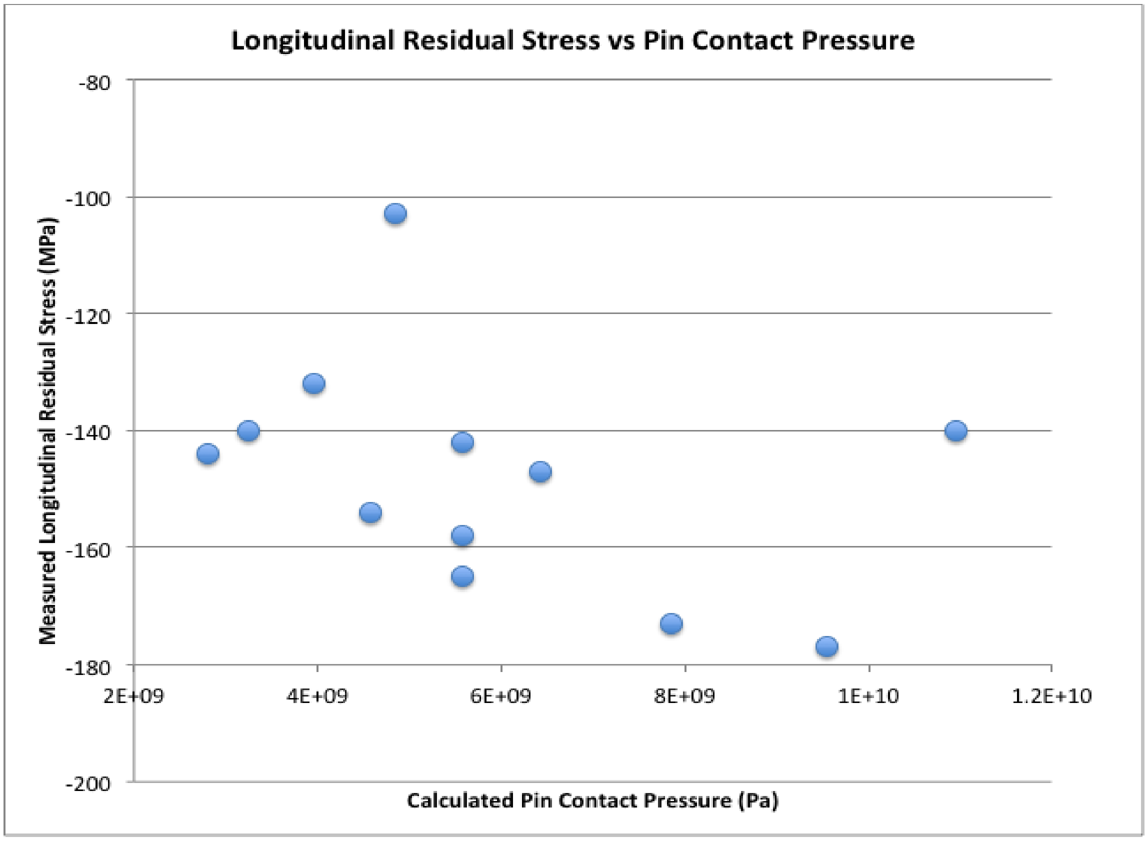

Figure 60. Average longitudinal stress in the base metal versus the calculated spherical contact pressure.

The severe plastic deformation that imparts the large compressive stresses on the surface of the plate clearly manifests itself in the microstructure. The GOS maps from the 40 percent power, 1 mm pin surface clearly showed plastic deformation up to 200 μm below the surface. This depth is supported by other studies that suggest evidence of UIT on microstructural characteristics of AA5456 to depths of at least 1.7 mm [40]. The EBSD data from just beneath the pin crater strongly suggests the presence of a nanocrystalline region, about 10 μm thick; this region could not be indexed by EBSD (Figure 46). This observation agrees with the recent work of Tran et al. who observed a nanocrystalline deformation region 10–18 μm below the surface of ultrasonically treated AA5456. Similar observations have also been made by An et al. after UIT on AA2024 [45].

Of greater concern is the extensive intergranular cracking observed in the microstructure of the material treated at 20 and 40 percent power with a 1 mm pin size. The cracks started at either the weld toe or about 14 mm away from the weld toe and ran parallel through the rest of the HAZ. The estimated contact pressure for these conditions is between 5–7 GPa. Other conditions in this study, (i.e., 20 percent power, 3 mm pin size and 20 percent power, 4 mm pin size), should have much lower contact pressures, about 3 GPa. In future work, cross sections of these ultrasonically treated welds will be examined for Intergranular cracking. Tran et al. also observed microstructural cracking or tearing in this alloy system [41]. In this work, the material was also sensitized and used a pin size of 3 mm diameter and displacement amplitude of 22 μm. By the analysis used here, the mean contact pressure would be approximately 4.6 GPa. Castillo-Morales et al. also observed a decrement in fatigue life after UIT of AA2024 samples, which they attributed to surface roughening and the nucleation of multiple cracks on the surface [44]. It would seem that UIT certainly can mitigate tensile residual stresses, but that care must be taken to not generate sub-surface cracking in the process.

Successfully taking residual stress measurements onboard a U.S. Navy cruiser was the most noteworthy objective achieved in this research. All of the measurements taken suggest that compressive stresses are common at the aluminum deck surface; which is the opposite of expectations, since tensile stresses are required for both SCC and corrosion fatigue. It should be noted that the compressive stresses measured were quite large and the data was clean. These compressive stresses are likely not from x-ray diffractometer issues. Several hypotheses might explain this outcome. It is possible that the relatively coarse metallographic method of surface preparation generated compressive stresses that were not removed during polishing. However, *in situ* metallography was utilized on a small area of the deck, and the x-ray diffraction measurement still returned a compressive stress of similar magnitude to those obtained in a near location when the coarse metallographic method was used. Electropolishing would mitigate this concern in future measurements, but it will require further collaboration to address all chemical safety concerns. It is possible that mechanical surface maintenance processes conducted by ships' crew and contractors may impart compressive residual stresses into the deck surface. Deck crawlers, needle guns, and other methods that are used In an effort to prepare the deck for painting, may induce compressive stresses on the surface of the material. There tools leave behind evidence of use in the form grooves and divots on the surface. The impact of these tools on residual stresses in aluminum is largely unknown. Future laboratory testing would determine if this hypothesis is true.

V. CONCLUSION

X-ray diffraction was used to measure residual stresses of welded and ultrasonically treated, sensitized and non-sensitized AA5456. UIT parameters were systematically varied to determine the effects of these parameters on residual stresses and microstructure. The most notable accomplishment of this research was the step taken towards gathering more information on the residual stresses in ship structures by taking measurements onboard an active U.S. Navy cruiser.

The following conclusions can be drawn from this work:

- The iXRD was successfully able to measure residual stress distributions around gas tungsten arc and gas metal arc welds in AA5456. As expected, the breadth of tensile residual region increased with increasing heat input, while the maximum in tensile stress increased with increasing weld travel speed.
- UIT parameters were systematically varied to study the effects of two control parameters, pin diameter and displacement amplitude, on the surface and subsurface residual stresses generated on in-service sensitized, GMAW AA5456 plates. All of the UIT parameter combinations induced significant compressive stresses that eliminated the tensile stresses in the HAZ caused by welding. Smaller pin sizes induced larger compressive stresses.
- Welding results in grain growth in the fusion zone, which was subsequently deformed by the UIT processing. Substantial microscale plasticity was evident from the UIT process in the weld, HAZ, and base metal. Microvoids and microcracking were observed in the subsurface area for UIT performed at 20 and 40 percent power input, with a 1 mm pin size.
- X-ray residual stresses were successfully performed on a U.S. Navy cruiser to determine the in service stresses located on the deck of the aluminum superstructure near welds and an existing crack. The measurements revealed compressive stresses on the surface of the deck in all locations tested. These stresses may be a result of surface preparation, surface processing (e.g., deck crawlers, needle gunning), or the geometric complexities of the deck structure.

The data collected and presented offers just a small contribution to the knowledge base for AA5456, sensitization, and UIT. Additional research into several aspects of this thesis is recommended. Further research should be conducted regarding the microstructural changes as a function of each UIT parameter combination in order to find the optimal parameters for mitigating SCC in 5xxx series aluminum alloys. Further depth resolved measurements would more fully characterize the residual stresses generated by UIT. Depth resolved measurements on board an active ship would also prove beneficial, since the measured residual stresses were shown to be quite complex. Additional shipboard measurements to better understand the stresses throughout the structure of in-service vessels are needed. This data would prove extremely valuable in future ship designs and could validate finite element models of ship structures.

APPENDIX ROSENTHAL'S 3-D SOLUTION MATLAB CODE

MATLAB Code as developed by Scott Millhouse

```
%3-D Rosenthal Solution
%AA 5456
%2in/min
%100 Amps

clear
clc
clf

%------------------------------------------------
%  Variables
%------------------------------------------------

Material='AA';
Desig='5456';
Velocity=2;
I=100;                  %amps
E=15.4;                 %volts, voltage based on 100 amps
XLcolumn='B';           %Column to write to in excel summary

%AA specific values from Kou Table 2.1
a=8.5*10^-5;     %m^2/s, thermal diffusivity
k=229.0;         %W/m-K, workpiece thermal conductivity
Cp=2.7*10^6;     %J/m^3-K, specific heat capacity
Tm=911;          %K, melting Temp
%------------------------------------------------

%Universal Values
T0=298;         %Temperature of workpiece before welding, assumed value
n=0.7;          %arc efficiency, assume for GTAW fig 2.7

%Intermediate Calculations
Q=n*E*I;        %heat transferred from heat source to piece
V=Velocity*0.0254/60;   %m/sec; 2 in/min, velocity

%Width of fusion zone, solve for T where T=Tm in y-direction
%Use Kou 2.10
LHS=2*pi*(Tm-T0)*k/Q;
RHS=-V/(2*a);
Tol=.1;
for i=1:500
    R(i)=i/10000;
    L(i)=log(LHS*R(i));
    Rfn(i)=RHS*R(i);
    if L(i)<=(Rfn(i)+Tol) && L(i)>=(Rfn(i)-Tol)
        Y=R(i);
        break
```

```
    end

end
yFZ=Y

%Thermal cycles (T vs time) for y=FZB, y=FZB+6mm, y=FZB+12mm

    t=linspace(-10,25,1000);
    x=t.*V;

    %y=FZB
    R=sqrt(x.^2+Y^2);
    d=R-x;
    TFZB=Q*exp(-V*d./(2*a))./(2*pi*k*R)+T0;

    %y=FZB+6
    R6=sqrt(x.^2+(Y+0.006)^2);
    d6=R6-x;
    T6=Q*exp(-V*d6./(2*a))./(2*pi*k*R6)+T0;

    %y=FZB+12
    R12=sqrt(x.^2+(Y+0.012)^2);
    d12=R12-x;
    T12=Q*exp(-V*d./(2*a))./(2*pi*k*R12)+T0;


TC=figure(1);
plot(t,TFZB,'b',t,T6,'r',t,T12,'c')
hleg1=legend('y=FBZ', 'y=FBZ+6mm', 'y=FBZ+12mm');
title(['Thermal Cycles ',num2str(Material),' ',num2str(Desig),...
    ' Velocity = ',num2str(Velocity),' in/sec Current = ',num2str(I),'
amps'])
xlabel('Time, sec')
ylabel('Temperature, K')
filenameTC=['TC',num2str(Material),num2str(Desig),'_',...
     num2str(Velocity),'_',num2str(I)];
print(TC,'-djpeg',filenameTC)

%Cooling rate (dTdtx) for y=FZB, y=FZB+6mm, y=FZB+12mm
dTdtx=2*pi*k*V*(max(TFZB)-T0)^2/Q;
dTdtx6=2*pi*k*V*(max(T6)-T0)^2/Q;
dTdtx12=2*pi*k*V*(max(T12)-T0)^2/Q;

%HAZ Width
THAZ=0.45*Tm;
for j=1:500
    yHAZ(j)=j/10000;
    %assume x and z are zero and increase away from centerline in y
    %direction using Rosenthal's 3-d Eqn
    Ty(j)=Q*exp(-V*yHAZ(j)./(2*a))./(2*pi*k*yHAZ(j))+T0;
    if Ty(j)<=THAZ
        HAZ=yHAZ(j)
        break
```

```
    end
end

%output to excel file
filename='summary.xlsx';
name=strcat(Material,Desig);
data={name; Velocity; I; yFZ; dTdtx; dTdtx6; dTdtx12; HAZ};
sheet=1;
xlRange=strcat(XLcolumn,'1');
xlswrite(filename,data,sheet,xlRange);
```

THIS PAGE INTENTIONALLY LEFT BLANK

LIST OF REFERENCES

[1] R. Schwarting et al., "Manufacturing techniques and process challenges with CG47 class ship aluminum superstructure modernization and repairs," BAE Systems, Norfolk, VA, 2011.

[2] United States Navy. (2013, Nov.). America's Navy. [Online]. Available: http://www.navy.mil/navydata/fact_display.asp?cid=4200&tid=800&ct=4US

[3] W. W. Sanders and K. A. McDowell, "Fatigue behavior of 5000 series aluminum alloy weldments in marine environment," in *Welding Research Council Bulletin,* no. 242, pp. 1–15, 1978.

[4] R. A. Sielski, "Ship structural health monitoring research at the Office of Naval Research," in *Journal of the Minerals, Metals & Materials Society,* vol. 64, no. 7, pp. 823–827, 2012.

[5] *ASM Handbook on Properties and Selection: Nonferrous Alloys and Special-Purpose Materials*, vol. 2. Materials Park, OH: American Society of Materials International, 2012, pp. 19–28.

[6] Y. Zhong. (2005). *Alloy phase diagram database*. [Online]. Available: http://www1.asminternational.org.libproxy.nps.edu/asmenterprise/APD/ViewAPD.aspx?id=101029

[7] M. G. Fontana, *Corrosion Engineering.* New York, NY: McGraw-Hill Book Company, 1987, pp. 820-824.

[8] *ASM Handbook on Corrosion: Fundamentals Testing and Protection*, vol. 13. Materials Park, OH, 2012, pp. 346-366: American Society of Materials International,

[9] Hydro. (2009, 26 Oct.). Alloy elements. [Online]. Available: http://www.hydro.com/en/Subsites/Tonder/Products-and-services/Aluminium-profiles/Choice-of-material/Alloys/Alloy-elements/

[10] *ASM Handbook on Properties and Selection: Nonferrous Alloys and Special-Purpose Materials*, vol. 2. Materials Park, OH: American Society of Materials International, 2012, pp. 3–14.

[11] *ASM Handbook on Properties and Selection: Nonferrous Alloys and Special-Purpose Materials*, vol. 2. Materials Park, OH: American Society of Materials International, 2012, pp. 29–61.

[12] N. Sukiman et al.,"Durability and corrosion of aluminum and its alloys: overview, property space, techniques and developments," in *Aluminum Alloys—New Trends in Fabrication and Applications*, 2013, pp. 47–97.

[13] D. Williams, "Stress corrosion cracking in an annealed 5083 aluminum alloy weldment," in *Welding Journal*, vol. 62, no. 8, pp. 25–27, 1983.

[14] R. L. Holtz et al., "Corrosion-fatigue behavior of aluminum alloy 5083-H131 sensitized at 448K," in *Matallurgical and Materials Transactions,* vol. 43A, pp. 2839–2849, Aug. 2012.

[15] J. Searles et al., "Stress corrosion cracking of sensitized AA5083 (Al-4.5Mg-1.0Mn)," in *Metallurgical and Materials Transactions,* vol. 32A, pp. 2859–2867, Nov. 2001.

[16] R. Goswami et al., "Microstructural evolution and stress corrosion cracking behavior of Al-5083," in *Metallurgical and Materials Transactions,* vol. 42A, pp. 348–355, Feb. 2011.

[17] L. Kramer et al., "Locally reversing sensitization in 5xxx aluminum plate," in *Journal of Materials Engineering and Performance,* vol. 21, no. 6, pp. 1025–1029, 2012.

[18] C. B. Crane and R. P. Gangloff, "Stress corrosion cracking of low temperature sensitized AA5083," presented at NACE International DOD Corrosion Conference, La Quinta, CA, Jul. 31–Aug. 5, 2011.

[19] R. Holtz et al., "Corrosion fatigue of AL 5083-H131 sensitized at 70, 100, and 175C and relation to microstructure and degree of sensitization," presented at NACE International DoD Corrosion Conference, La Quinta, CA, Jul. 31–Aug. 5, 2011.

[20] R. Goswami et al., "Precipitation of the beta phase in Al-5083," in *Materials Science and Engineering Journal,* vol. A, no. 527, pp. 1089–1095, 2010.

[21] *Standard Specifications for High Magnesium Aluminum-Alloy Sheet and Plate for Marine Service and Similar Environments*, ASTM B928, 2013.

[22] *Standard Test Method for Determining the Susceptibility to Intergranular Corrosion of 5XXX Series Aluminum Alloys by Mass Loss After Exposure to Nitric Acid (NAMLT),* ASTM G67, 2004.

[23] E. C. Cormack, “The effect of sensitization on the stress corrosion cracking of aluminum alloy 5456,” M.S. Thesis, Dept. Mech. Eng., Naval Postgraduate School, Monterey, CA, 2012.

[24] M. Pourbaix, *Atlas of Electrochemical Equilibria*, Houston, TX: National Association of Corrosion Engineers, 1974.

[25] D. R. Arnott et al., "Oxide film rupture, reanodization, and stress corrosion cracking in aluminum," in *Journal of Electrochemical Science and Technology*, vol. 129, no. 12, pp. 2660–2665, Dec. 1982.

[26] H. L. Logan, "Film rupture mechanism of stress corrosion," in *Journal of Research of the National Bureau of Standards,* vol. 48, no. 2, pp. 99–105, Feb. 1952.

[27] R. Jones, "The influence of hydrogen on the stress corrosion cracking of low strength Al-Mg alloys," in *Journal of Minerals, Metals, and Materials,* pp. 42–46, Feb. 2003.

[28] J. Farmer, “Lecture L3-types of corrosion,” unpublished.

[29] M. Meyers and K. Chawla, *Mechanical Behavior of Materials*, Cambridge, UK: Cambridge University Press, 2009, pp. 820–824.

[30] S. Kou*, Welding Metallurgy*, 2nd ed. Hoboken, NJ: John Wiley and Sons, Inc., 2003.

[31] M. N.James et al., "Residual stress and strain in MIG butt welds in 5083-H321 aluminum: as-welded and fatigue cycled," in *International Journal of Fatigue,* vol. 31, pp. 28-40, 2009.

[32] L. Kramer et al., "Locally reversing sensitization in 5xxx aluminum plate," in *Journal of Materials Enginering and Performance,* vol. 21, no. 6, pp. 1025–1029, 2012.

[33] M. B. Kannan and V. S. Raja, "Enhancing stress corrosion cracking resistance in Al-Zn-Mg-Cu-Zr alloy through inhibiting recrystallization," in *Engineering Fracture Mechanics,* vol. 77, no. 2, pp. 249–256, 2010.

[34] F. Zucchi et al., "Pitting and stress corrosion cracking resistance of friction stir welded AA5083," in *Materials and Corrosion,* vol. 52, pp. 853–859, 2001.

[35] R. Mishra and Z. Ma, "Friction stir welding and processing," in *Materials Science and Engineering,* vol. 50, pp. 1–78, 2005.

[36] H. Zoeller and B. Cohen, "Shot peening for resistance to stress corrosion cracking," in *Metals Engineering Quarterly*, pp. 16–20, Feb.1966.

[37] J. E. Rankin et al., "The effects of process variations on residual stress induced by laser peening," in *Materials Science Forum,* vol. 404, no. 407, pp. 95–100, 2002.

[38] B. Rouleau et al., "Characterization at a local scale of a laser shock peened aluminum alloy surface," in *Applied Surface Science,* vol. 257, pp. 7195-7203, 2011.

[39] K. A. Brandenburg et al., "Use of engineered compressive residual stresses to mitigate stress corrosion cracking and corrosion fatigue in sensitized 5xxx series aluminum alloys," in *Proceedings of Department of Defense Virtual Corrosion Conference*, Sept. 2013.

[40] C. Scheck et al., "Impact of ultrasonic impact treatment on a 5456 aluminum alloy characterized through microspecimen testing and x-ray tomography," in *TMS 2011 Supplemental Proceedings Vol 2: Materials Fabrication, Properties, Characterization, and Modeling* San Diego, 2011, pp.205–212.

[41] K. N. Tran and L. Salamanca-Riba, "Microstructural evolution of severely plastically deformed sensitized aluminum 5456-H116 treated by ultrasonic impact treatment," in *Advanced Engineering Materials,* vol. 15, no. 11, pp. 1105–1110, 2013.

[42] T. Okawa et al., "Effect of preload and stress ratio on fatigue strength of welded joints improved by ultrasonic impact treatment," in *Weld World,* vol. 57, pp. 235–241, 2013.

[43] P. Mikheev et al., "Effectiveness of ultrasonic treatment for increasing the fatiue resistance of welds," in *Russian Ultrasonics,* vol. 15, no. 4, pp. 70–75, 1985.

[44] M. Castillo-Morales and A. Salas-Zamarripa, "The effects of UIT in the fatigue life of Al 2024-T3," in *Key Engineering Materials,* vol. 449, pp. 15–22, 2010.

[45] X. An et al., "Study of the surface nanocrystallization induced by the Esonix ultrasonic impact treatment on the near-surface of 2024-T351 aluminum alloy," in *Journal of Materials Engineering and Performance,* vol. 15, no. 3, pp. 355–364, Jun. 2006.

[46] B. Mordyuk et al., "Enhanced fatigue durability of Al-6Mg alloy by applying ultrasonic impact peening: effects of surface hardening and reinforcement with AlCuFe quasicrystalline particles," in *Materials Science and Engineering A,* vol. 563, pp. 138–146, 2013.

[47] E. S. Statnikov et al., "Comparison of ultrasonic impact treatment (UIT) and other fatigue life improvement methods," in *Welding in the World,* vol. 46, no. 3, pp. 20–32, 2002.

[48] P. Crooker, “Materials seminar on peening technology for mitigating PWSCC,” presented at NPS, Monterey, CA, May 29, 2013.

[49] C. Rodopoulos et al., "Effect of controlled shot peening and laser shock peening on fatigue performance of 2024-T351 aluminum alloy," in *Journal of Materials Engineering and Performance,* vol. 12, no. 4, pp. 414–419, 2003.

[50] Lambda Technologies Group. (2012). Low plasticity burnishing. [Online]. Available: http://www.lambdatechs.com/low-plasticity-burnishing-LPB.html

[51] Applied Ultrasonics. (2011). Esonix UIT. [Online]. Available: http://www.appliedultrasonics.com/solutions.html

[52] Europe Technologies Group. (2009).Sonats needle peening objectives. [Online]. Available: http://www.sonats-et.com/page_23-needle-peening.html

[53] K. Tran, “Microstructural characterization of ultrasonic impact treated Al-Mg alloy,” Ph.D. dissertation, Dept. Mat. Sci., Univ. of Maryland, College Park, MD, 2012.

[54] Europe Technologies Group. (2013, Oct.). STRESSONIC principle. [Online]. Available: http://www.sonats-et.com/page_12-stressonic.html

[55] D. Goudar et al., "Measurement of residual stresses in surface treated stainless steel groove welds," in *Materials Science Forum,* vol. 681, pp. 49–54, 2011.

[56] C. Rodopoulos et al., "The effect of surface engineering treatments on the fatigue behavior of 2024-T351 aluminum alloy," in *Journal of Materials Engineering and Performance,* vol. 16, no. 1, pp. 30–34, 2007.

[57] X. Cheng et al., "Residual stress modification by post-weld treatment and its beneficial effect on fatigue strength of welded structures," in *International Journal of Fatigue,* vol. 25, pp. 1259–1269, 2003.

[58] M. Liao et al., "Effects of ultrasonic impact treatment on fatigue behavior of naturally exfoliated aluminum alloys," in *International Journal of Fatigue,* vol. 30, pp. 717–726, 2008.

[59] G. S. Schajer, Ed., *Practical Residual Stress Measurement Methods*. West Sussex, UK: John Wiley & Sons Ltd, 2013.

[60] S. Farrell et al., "Stress analysis on Canadian naval platforms using a portable miniature x-ray diffractometer," in *Powder Diffraction,* vol. 25, no. 2, pp. 119–124, 2010.

[61] D. Huff and K. Lynaugh, "Utilization of root cause failure analysis in the investigation of marine deck fitting failures," in *Naval Engineers Journal,* pp. 93–99, Winter 2001.

[62] C. E. Murray and I. C. Noyan, "Applied and residual stress determination using x-ray diffraction," in *Practical Residual Stress Measurement Methods*, West Sussex, UK, John Wiley & Sons Ltd., 2013, pp. 139–161.

[63] *Standard and Emergency Operating Procedures for Proto iXRD Inside Laboratory Enclosure* (NAVPGSCOL INST 6470.14), Naval Postgraduate School, Moneterey, CA, 2013.

[64] M. Bennett, "Characterization of Residual Stress as a Function of Friction Stir Welding Parameters in ODS Steel MA956," M.S. thesis, Dept. Mech. Eng., Naval Postgraduate School, Monterey, CA, 2013.

[65] *PROTO Electrolytic Polisher-Operating Manual Version 3.01*, Proto Manufacturing Ltd., Taylor, MI.

[66] Naval Sea Systems Command, *Radialogical Affairs Support Program Manual* (SS0420-AA-RAD-010 Rev 1A). Washington Navy Yard, Naval Sea Systems Command, 2012.

[67] Naval Postgraduate School, *NAVPGSCOL Instruction 6470.14: Standard and Emergency Operating Procedure for Proto iXRD during Field Use,* Monterey: Naval Postgraduate School, 2013.

[68] W. Golumbfskie, private communication, "*In situ* metallography," Mar.2014.

[69] *Standard Test Method forVerifying the Alignment of X-ray Diffraction Instrumentation for Residual Stress Measurement*, ASTM E915-10, 2012.

[70] S. Millhouse, "MATLAB code for 3-D Rosenthal's solution*,"* unpublished.

[71] A. R. Kohandehghan et al., "A study on residual stresses in gas tungsten arc welding of AA5251," in *Materials and Manufacturing Processes,* vol. 25, pp. 1242–1250, 2010.

[72] W. D. Callister and D. G. Rethwisch, *Materials Science and Engineering an Introduction*, Hoboken, NJ: John Wiley & Sons, 2010.

[73] A. C. Fischer-Cripps, *Nanoindentation*, 2nd ed., New York, NY: Springer, 2004.

[74] *Manual for Stress Analysis-Software Manual*. Ontario:Proto Manufacturing Ltd., Oldcastle, 2010.

THIS PAGE INTENTIONALLY LEFT BLANK

INITIAL DISTRIBUTION LIST

1. Defense Technical Information Center
   Ft. Belvoir, Virginia

2. Dudley Knox Library
   Naval Postgraduate School
   Monterey, California